CONSTRAINTS ON MODELS FOR THE HIGGS BOSON WITH EXOTIC SPIN AND PARITY

By

Emily Hannah Johnson

A DISSERTATION

Submitted to
Michigan State University
in partial fulfillment of the requirements
for the degree of

Physics - Doctor of Philosophy

2016

ABSTRACT

CONSTRAINTS ON MODELS FOR THE HIGGS BOSON WITH EXOTIC SPIN AND PARITY

By

Emily Hannah Johnson

The production of a Higgs boson in association with a vector boson at the Tevatron offers a unique opportunity to study models for the Higgs boson with exotic spin J and parity P assignments. At the Tevatron the VH system is produced near threshold. Different J^P assignments of the Higgs boson can be distinguished by examining the behavior of the cross section near threshold. The relatively low backgrounds at the Tevatron compared to the LHC put us in a unique position to study the direct decay of the Higgs boson to fermions. If the Higgs sector is more complex than predicted, studying the spin and parity of the Higgs boson in all decay modes is important. In this Thesis we will examine the $WH \to \ell\nu b\bar{b}$ production and decay mode using $9.7\,\mathrm{fb}^{-1}$ of data collected by the D0 experiment in an attempt to derive constraints on models containing exotic values for the spin and parity of the Higgs boson. In particular, we will examine models for a Higgs boson with $J^P = 0^-$ and $J^P = 2^+$. We use a likelihood ratio to quantify the degree to which our data are incompatible with exotic J^P predictions for a range of possible production rates. Assuming the production cross section times branching ratio of the signals in the models considered is equal to the standard model prediction, the $WH \to \ell\nu b\bar{b}$ mode alone is unable to reject either exotic model considered. We will also discuss the combination of the $ZH \to \ell\ell b\bar{b}$, $WH \to \ell\nu b\bar{b}$, and $VH \to \nu\nu b\bar{b}$ production modes at the D0 experiment and with the CDF experiment. When combining all three production modes at the D0 experiment we reject the $J^P = 0^-$ and $J^P = 2^+$ hypotheses at the 97.6% CL and at the 99.0% CL, respectively, when

assuming the signal production cross section times branching ratio is equal to the standard model predicted value. When combining with the CDF experiment we reject the $J^P = 0^-$ and $J^P = 2^+$ hypotheses with significances of 5.0 standard deviations and 4.9 standard deviations, respectively.

For my parents.

ACKNOWLEDGMENTS

I've found particle physics fascinating since high school and it has been my absolute pleasure to become acquainted with the field in the years since then. My interest in physics as well as the drive and determination necessary to complete my degree did not simply materialize from the vacuum but were the result of many positive influences from the people in my life. I would like to use this space to thank those people.

First and foremost I would like to thank my parents Shelley and Donald Johnson. I can attribute much of my love of math and science to their guidance. They fed my childhood curiosity by always attempting to answer my questions fully and by engaging me in activities and discussions that peaked my interests. The most memorable activities in my early childhood were the crafting of homemade experiments with my mother. We watched lima beans and rock candy grow in jars and tried to figure out which substances would slow the accumulation of rust on nails. In addition to fueling my curiosity they also gave me a lot of encouragement and support. I always knew that I could try for any career, even ones that were seen as non-traditional. I was shy, so sometimes the encouragement came in the form of a healthy shove. One such shove involved attending a math and science mini-conference for girls where I realized that 'scientist' could be a valid career option. For these things and so much more I am eternally grateful.

I entered high school with an interest in science and filled my electives with additional science classes. I had several good teachers who all deserve my thanks. One teacher in particular, Thomas Yocum, I credit with getting me interested in particle physics. I asked him a question after class one day and the discussion led to him lending me one of his books on special relativity. After reading this book I began to seek out books on the topic of particle physics that were accessible to my level. Another positive influence during high school was not a single person but a group of people at the University of Michigan who put together the Saturday Morning Physics series. These lectures (still ongoing at the time of this writing) showcase recent research and are tailored for the general public.

I applied to and got accepted by Michigan State University as a physics major in 2003. As an undergraduate I had many positive experiences and opportunities to learn and grow in the physics department. Probably like most physics undergraduates the course I had been anticipating the most was quantum mechanics. Both semesters were taught by Wayne Repko. Not only did I find him to be an excellent teacher but also a great mentor. He encouraged me to spend my summers participating in Research Experience for Undergraduates (REU) programs both at MSU and Rice University. These allowed me to experience different fields of physics research. When my interests kept coming back to particle physics I asked him if there were any research opportunities for an undergraduate in the department. We took a walk down the hall and he introduced me to Kirsten Tollefson and Reinhard Schwienhorst. They took me on and introduced me to particle physics research. I was able to learn by being involved in research at CDF and D0, the two experiments at the highest-energy particle collider in the world at that time. It was truly an excellent experience. I am certain that I would not be where I am today were it not for the guidance of these three people.

I was interested in going to graduate school and was encouraged to apply. Since I felt that I had found a home at MSU, I decided to stay. The first few years of my graduate career were spent completing coursework and supervising undergraduate lab classes. I struggled somewhat under the load and ended up behind in some of my courses. Here I relied on my friends and fellow graduate students (you know who you are) who worked through problems with me. I appreciate all of those study sessions. I would also like to thank Vladimir

Zelevinsky; he devoted much of his time after class to help students work through problems and provide encouragement.

I began to work with Wade Fisher shortly after he joined the MSU department. I was nervous in the beginning to be working with someone new, but Wade has a talent for making me feel at ease. He has been an absolutely wonderful advisor. He is a dedicated teacher who has spent countless hours helping me to understand everything from particle detectors to statistics. His patience and encouragement have been invaluable during my years as a graduate student. I could not have asked for a better advisor.

At MSU and D0 I had the pleasure of working closely with many people to solve common problems and collaborate on physics analyses. In particular, I would like to acknowledge Lidija Živković and Ken Herner who were my contact points and surrogate advisors at D0. Their help with this analysis in particular is greatly appreciated. I would also like to thank Savanna Shaw, my co-graduate student under Wade and an excellent teacher in her own right. Her ability to understand my thoughts and anticipate my questions is nearly unrivaled. Thanks to Brad Schoenrock and Patrick True who invited me out to social events and made me feel included, and to James Koll who answered nearly all my computing questions.

I would also like to thank the office staff at MSU, specifically Debbie Barratt, Kim Crosslan, and Brenda Wenzlick, for helping me keep it all together.

Lastly, I would like to thank my partner Bryan Moule who has been with me all through my undergraduate and graduate education. He has been an ever-present source of encouragement and support and I am glad to have him in my life.

For the rest: there are far too many people to list here by name, but know that you have my gratitude.

PREFACE

Particle physics is a fascinating field and so my hope for this Thesis is that it is readily accessible by both the veterans of the field and those who may be unfamiliar with the field. To help with this goal I've divided this Thesis into two Parts. Part I is a general overview of the tools used in particle physics as well as a theoretical overview of the field. Part II expands on this background information and describes the particulars of the research project that forms the subject of this Thesis, from the devices used to gather data to the statistical analysis and interpretation of my results. A veteran of the field will be satisfied with skipping Part I entirely to get straight to the specific analysis in Part II. Someone less familiar can read Part I to get a better grasp of Part II.

TABLE OF CONTENTS

LIST OF TABLES

LIST OF FIGURES

Part I

Introduction to Particle Physics

Part I introduces the concepts essential to understanding any particle physics experiment. Chapter 1 serves as an introduction to the field. The notational information given in Section 1.3 will be useful throughout this Thesis. Chapter 2 introduces the tools used by particle physicists to conduct research. It describes the equipment necessary to accelerate, produce, and detect high energy particles. A general overview of the theoretical structure is given in Chapter 3 with special consideration given to electroweak symmetry breaking and Higgs boson physics.

Chapter 1

Introduction

1.1 Fundamental Questions

The meaning of what is truly a *fundamental* particle has changed throughout the centuries. The atom, from the Greek *atomos* meaning ‘indivisible’, is composed of several particles, some truly fundamental and some composite. From experiments by J.J. Thompson and Rutherford it was discovered that the atom consists of a halo of very light negatively charged particles (electrons) with a heavy positively charged nucleus at the center. Rutherford named the nucleus of the lightest element hydrogen ‘proton’. Since hydrogen is electrically neutral it was assumed to contain one electron. It seemed natural to expand this idea to heavier elements with each having one more proton and electron than the previous. While this is indeed true, it was not obvious from the start because instead of weighing twice as much as hydrogen, helium weighed *four* times as much. However, helium did contain two electrons, so where did the extra mass come from? This mystery wasn’t resolved until the discovery of the neutron by Chadwick. For a few years, all matter was perceived to be made up of protons, neutrons, and electrons.

Physicists at this time were only familiar with the two forces that can be seen at work in ordinary macroscopic experiments: electromagnetism and gravity. Electromagnetism was formulated by Maxwell in the 1860s. Maxwell’s equations required that the speed of electromagnetic waves (including light) in a vacuum be constant. This led to the idea that there existed a unique frame of reference in which electromagnetic waves propagated and Maxwell's equations held. This (almost magical) frame of reference was named the *aether*. Indeed, as time went on its properties became more and more fanciful; it needed to be a fluid to fill all space but also be very rigid to accommodate the high frequencies of electromagnetic waves. Many other problems plagued the notion of the aether, not the least of which was the continual negative results of experiments designed to directly detect it. The famous *Michelson-Morley* experiment in 1887 is frequently thought of as the turning point in the belief in the existence of the aether. They found that a beam of light traveling in the same direction as the motion of the earth through the aether doesn't take any longer to travel than a beam traveling perpendicular to the motion. In the end, Einstein developed the theory of special relativity that didn't rely on the existence of the aether and perfectly explained the form of Maxwell's equations. The constant speed of light in a vacuum, along with the principle of relativity, became the postulates of special relativity.

In the 1910s Einstein developed general relativity as a relativistic description of gravity. It changed the way the community thought about space and time. Space was no longer an unchanging void but something that was intricately related to time. Mass and energy change the very nature of space-time and cause it to curve. Planets orbiting stars follow curved paths like marbles on a rubber sheet, responding to the large mass of the star.

At this time it was well known that the electrons and protons were bound by the electromagnetic force due to their opposing charges. Bohr's classical depiction of hydrogen as a single electron orbiting a proton was very successful. What held together the tightly packed protons? Since they all have the same charge they should be forced apart. It was clear that there was another force at work. What was its source? Were the proton, neutron, and electron truly fundamental particles? Questions like these have since been answered and new ones have come to take their place. The goal of particle physics has been an understanding of the fundamental particles and the forces that guide their interactions.

1.2 Standard Model & Predictions

The field of particle physics exists because the laws of physics used for speeding trains and flying cannonballs break down for very small and very fast objects[1]. Objects are considered 'relativistic' (i.e. very fast) if their speed is close to the speed of light c. The behavior of subatomic particles can be described by quantum mechanics. A visualization of the theories that are used to describe these regimes can be seen in Table 1.1. The theories that deal with very small and very fast particles are quantum field theories (QFT). Each fundamental force (with the exception of gravity) has a corresponding field theory that describes how the fundamental particles interact under its influence. The collection of these theories is called the standard model (SM) of particle physics. The SM can make predictions on the types of interactions that can occur, what a particle can decay to, and even the existence of particles. We can use these predictions as a test of the model. If the predictions don't describe reality, then at the very least the model must be incomplete. In the worst case (or

	faster	⇒
smaller	Classical $v \ll c$	Relativistic $v \sim c$
⇓	Quantum	Quantum Field Theory

Table 1.1: *Limits of Physical Laws*
A visualization of the physical theories in the high-velocity and small-scale regimes.

---

[1] It is for this reason that particle physics is also called *high energy physics* – the high velocity of the particles corresponds to their high energy.

the most interesting case, depending on your point of view) the model will have to be rebuilt. New predictions will either point to the model being correct or another reevaluation of the model. This cycle of testing and reevaluation is the scientific method. Observations made lead to a hypothesis about how the world works which in turn leads to predictions based on the hypothesis. These predictions are either confirmed and the hypothesis is strengthened or invalidated and the hypothesis discarded. Particle physics is simply the scientific method at work with the SM as its testable hypothesis.

1.3 Notes on Notation

It is prudent here to summarize a few notational quirks present in particle physics. This section is divided into information on coordinate systems, the Einstein summation convention, and natural units. This section also has several useful figures describing the coordinate system that we use in particle physics that may be useful to refer to in the following chapters.

1.3.1 Coordinate Systems

Because of the physical design of particle physics experiments, the coordinate system we use when describing various aspects of the experimental side of the field is not the cartesian coordinate system. Colliding particles naturally leads to a coordinate system where the incoming particles' trajectories are aligned along the axis of a cylinder. Because the energies of the colliding particles are high, the particles that are produced at the collision point preferentially have trajectories that are at a small angle relative to the axis. It is for this reason that particle detectors are cylindrical in design. However, because the particles produced originate from a collision point, it is convenient to define trajectories by the angle relative to the axis. The end result of this is the combination of the spherical and cylindrical coordinate systems illustrated in Fig. 1.1. We use the z coordinate of the cylindrical system as the axis of our detector. The polar angle from the spherical system is the angle that defines the trajectories of the particles produced at the center of the detector. Finally, the azimuthal angle common to both the cylindrical and spherical coordinate systems completes our coordinate system.

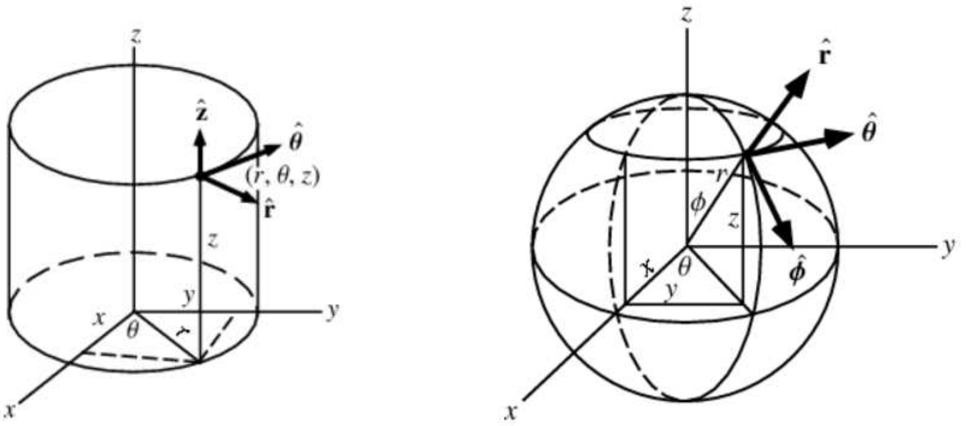

Figure 1.1: *Coordinate Systems*
Depictions of the cylindrical and spherical coordinate systems[1, 2]. In particle physics the naming convention is reversed for ϑ and φ.

While these coordinates would be sufficient to describe particles in the experimental setup, one additional change is useful. A new quantity *pseudorapidity* denoted by η is defined as

$$\eta = -\ln\left[\tan\left(\frac{\vartheta}{2}\right)\right] \tag{1.1}$$

where ϑ is the polar angle. The range of the familiar coordinate ϑ is $0 \leq \vartheta \leq \pi$ while the range of η is $-\infty < \eta < \infty$ as implied by Eq. 1.1. Figure 1.2 shows both the polar angle and the pseudorapidity variable for a few values of each. The advantage of using η instead of ϑ is that particle production is typically uniform in pseudorapidity, but not in polar angle.

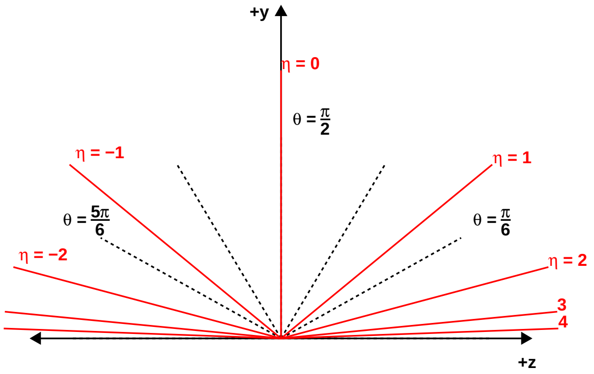

Figure 1.2: *Pseudorapidity and Polar Angle*
A comparison of pseudorapidity η and polar angle ϑ for several values of each.

1.3.2 Minkowski Space and Einstein Notation

The theories in particle physics are formulated not in traditional three-dimensional Euclidean space but in a four-dimensional space called *Minkowski space-time*. The four dimensions of this space consist of the three Euclidean spatial dimensions and one time dimension. The standard basis used by particle physicists is the set of four mutually orthogonal vectors e_μ such that $e_0 = -e_1 = -e_2 = -e_3 = 1$ where e_0 is the time component. This can be written in a more compact form:

$$g_{\mu\nu} = g^{\mu\nu} = \begin{pmatrix} 1 & 0 & 0 & 0 \\ 0 & -1 & 0 & 0 \\ 0 & 0 & -1 & 0 \\ 0 & 0 & 0 & -1 \end{pmatrix} \tag{1.2}$$

where $g_{\mu\nu}$ is called the Minkowski metric. Vectors in Minkowski space are called *four-vectors*. Perhaps two of the most easily recognizable four-vectors are the position-time four-vector

$x^\mu = (ct,\, x,\, y,\, z)$ and the four-momentum $P^\mu = \left(\frac{E}{c},\, p_x,\, p_y,\, p_z\right)$. Whether or not the indices are superscript or subscript depends on whether the vectors are *contravariant* or *covariant*, respectively. Covariant vectors have components that transform under the same matrix that transforms the basis; they co-vary with a change in basis. Contravariant vectors contra-vary with a change in basis – their components transform under the inverse of the matrix that transforms the basis. Using the Minkowski metric we can raise or lower these indices (in effect changing whether the vectors are covariant or contravariant) in the following way:

$$\begin{aligned} A^\mu &= \sum_{\nu=0}^{3} g^{\mu\nu} A_\nu \\ A_\mu &= \sum_{\nu=0}^{3} g_{\mu\nu} A^\nu \end{aligned} \tag{1.3}$$

where $g_{\mu\nu} = (g_{\mu\nu})^{-1} = g^{\mu\nu}$.

In this Thesis we will use Einstein notation, a summation convention that is clean and concise. In this convention a term with repeated indices carries an implied summation of the term over all values of the repeated index. Table 1.2 shows examples of common operations in both the traditional notation and Einstein notation for three dimensions using an orthogonal basis. This notation allows us to rewrite Eq. 1.3 as

$$\begin{aligned} A^\mu &= g^{\mu\nu} A_\nu \\ A_\mu &= g_{\mu\nu} A^\nu \end{aligned} \tag{1.4}$$

where the implied summation is over the four space-time components. Throughout this text quantities in three-dimensional space will have indices taken from the Latin alphabet (whose values $\in \{1,\, 2,\, 3\}$) while quantities in four-dimensional space-time will have indices taken from the Greek alphabet (whose values $\in \{0, 1, 2, 3\}$).

	Quantity	Summation Formulation	Einstein Notation
Vector Dot Product	$c = \boldsymbol{a} \cdot \boldsymbol{b}$	$c = \sum_{i=1}^{3} a_i b_i$	$c = a_i b^i$
Vector Cross Product	$\boldsymbol{c} = \boldsymbol{a} \times \boldsymbol{b}$	$c_i = \sum_{j=1}^{3} \sum_{k=1}^{3} \epsilon_{ijk} a_j b_k$	$c^i = \epsilon^i{}_{jk} a^j b^k$
Matrix Multiplication	$\boldsymbol{C} = \boldsymbol{AB}$	$C_{ik} = \sum_{j=1}^{3} A_{ij} B_{jk}$	$C^i{}_k = A^i{}_j B^j{}_k$
Trace	$a = Tr(\boldsymbol{A})$	$a = \sum_{i=1}^{3} A_{ii}$	$a = A^i{}_i$

Table 1.2: *Einstein Notation Examples*
Common operations involving vectors and matrices in three dimensions using an orthogonal basis.

1.3.3 Natural Units

Because the theories that describe particle physics are relativistic quantum field theories, the speed of light c and the reduced Planck constant $\hbar$ make an appearance in many equations. To simplify our equations we use a system of natural units where

$$\hbar = c = 1. \tag{1.5}$$

In this system the units of mass, length, momentum, and time are now given solely in terms of energy. The most common unit for energy we work with in particle physics is the electron volt (eV). This is the change in energy of an electron moving across a potential difference of one volt. Although not an SI unit we use the standard SI prefixes, most commonly the giga-electron volt (GeV). Mass and momentum will be in GeV while length and time will be in GeV^{-1}.

Chapter 2

Tools

To study elementary particles we need to be able to produce them, record their interactions, and then interpret the results. This Chapter will be dedicated to the basics of particle production and detection. It will be built upon in later chapters with descriptions of the machinery specific to this Dissertation.

2.1 Particle Acceleration

To produce interesting and possibly never-before-seen particles we collide matter at high energy. The first step in setting up these collisions is the acceleration of particles to velocities approaching the speed of light. Current technologies using accelerating fields necessitate the use of electrically-charged particles. There are several accelerating schemes but all are based on the Lorentz force:

$$\boldsymbol{F} = q\left(\boldsymbol{E} + \boldsymbol{v} \times \boldsymbol{B}\right) \tag{2.1}$$

where q is the charge of the particle, $\boldsymbol{v}$ is its velocity, and $\boldsymbol{E}$ and $\boldsymbol{B}$ are the electric and magnetic fields, respectively. Because the force due to the magnetic field is perpendicular to the particle's velocity it cannot be used to accelerate the particle[1]. This means that all particle acceleration is done using electric fields.

---

[1] Technically the magnetic field cannot be used to accelerate a particle *in the direction of its velocity*–it can be used to accelerate a particle perpendicular to its direction, a detail that will be discussed later in the section.

2.1.1 Electrostatic Accelerators

The simplest type of accelerator uses a static electric field to impart energy to a stream of charged particles. This static electric field is produced by generating a constant voltage difference, similar to the field between capacitor plates. For a free test charge q moving in a uniform electric field the energy gained by the test charge is equal to the work done

$$W = -q\left(V_f - V_i\right) \tag{2.2}$$

where V_f and V_i are the final and initial voltage respectively. Negative test charges will accelerate in the direction opposite the electric field and positive test charges will accelerate in the direction of the electric field. To increase the energy gained by the particles you can increase their charge or you can increase the voltage difference they accelerate through. Depending on the particle species it is possible to add or remove electrons to increase the absolute value of the charge. Typically there is a limit to the amount of charge you can accumulate so we look to increasing the voltage difference. The high voltages required by particle physics experiments are obtained by specialized voltage generators. While there are several schemes for generating these high voltages we will discuss the one that is used to accelerate particles at Fermilab: the Cockcroft-Walton generator.

The Cockcroft-Walton generator is a voltage multiplier consisting of two stacks of capacitors linked by diodes as shown in Fig. 2.1 and is sometimes referred to as the Cockcroft-Walton ladder. The capacitors on the left hold a charge and couple to the alternating current (AC) voltage source at the bottom of the stack while the capacitors on the left are DC; the charge on them is constant. During the negative half-cycle the capacitors on the left are charged. The capacitors on the right are charged during the positive half-cycle. Figure 2.1

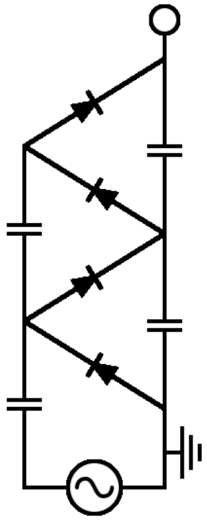

Figure 2.1: *Cockcroft-Walton Generator*
Schematic of a typical Cockcroft-Walton generator.

shows only two stages of a Cockcroft-Walton ladder, more can be added on to increase the output voltage. For a Cockcroft-Walton ladder with n stages the final output voltage is $2nV_0$.

In terms of high energy, the drawback of electrostatic accelerators is the relatively low high-voltage ceiling limited by the electrical breakdown of air. Gases with a higher dielectric constant such as sulfur hexafluoride can be used to increase the voltage limit. This gas is very commonly added to both Cockcroft-Walton and Van de Graaff generators. Getting particles to the extremely high energies used today requires a different method of accelerating particles using electromagnetic fields.

2.1.2 Oscillating Field Accelerators

Rolf Widerøe's resonance accelerator is widely known as the progenitor of all modern oscillating field accelerators. Its design effectively side-steps the breakdown problem by using several consecutive low voltage pushes. A schematic of a simple Widerøe accelerator is shown in Fig. 2.2. A particle exiting the source passes through a number of hollow cylindrical electrodes connected to an AC voltage source in such a way that adjacent electrodes carry opposing polarity. The frequency of the AC voltage source is such that when a particle is crossing a gap the accelerating field is at a maximum. The particles receive a kick from the electric field in the gap and accelerate. Once inside the cylindrical electrodes the particles are shielded from the electromagnetic field and drift down the tube at constant velocity. It is for this reason that the cylindrical electrodes are referred to as *drift tubes*. When the particles exit the drift tube the polarity has reversed and the field once again accelerates the particles. This does not allow continuous acceleration of a beam of particles. Instead, particles must be accelerated in *bunches*. To keep the particles in phase with the accelerating field as their velocity increases the lengths of the drift tubes are increased. As particles asymptotically approach the speed of light, however, the velocity gain (and hence the length difference in the drift tubes) is small.

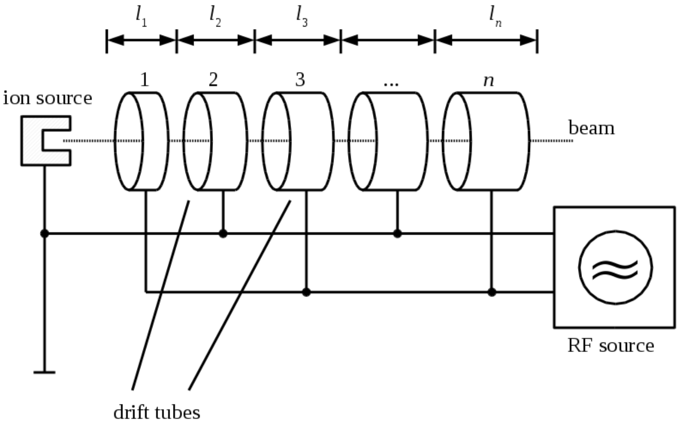

Figure 2.2: *Widerøe Accelerator*
Schematic of a simple Widerøe resonance accelerator.

Many oscillating field accelerators operate in the same manner as the Widerøe accelerator with one important improvement first made by Luis Alvarez. In order to keep the length of the drift tubes at a reasonable size the frequency must be increased. However, at high frequencies the Widerøe accelerator loses energy through electromagnetic radiation. Alvarez's solution was to place the Widerøe apparatus inside an evacuated conducting cavity. The driving power is coupled directly to the inside of the cavity and the electromagnetic fields are contained inside the conductor. Furthermore, if the resonance frequency of the cavity is equal to that of the acceleration frequency the energy transfer is the most efficient. Variations on this design lead to many different types of cavities that differ in size, shape, and conducting material. Examples of different cavities that operate in the microwave frequency range are shown in Fig. 2.3.

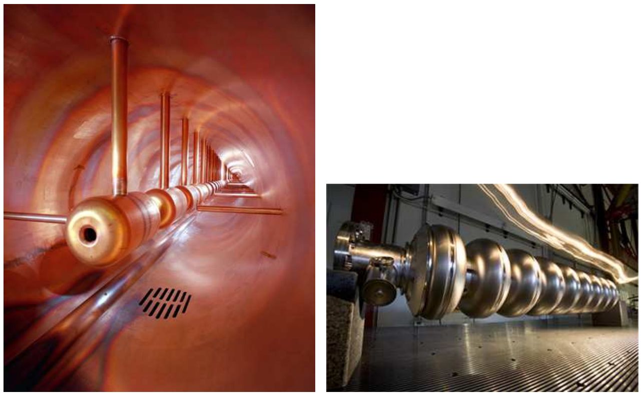

Figure 2.3: *Microwave Frequency Cavities*
Examples of cavity shapes that operate in the microwave frequency range. An Alvarez drift tube cavity and a superconducting cavity made to operate at very low temperature.

A device which has an advantage over the linear accelerators is the *synchrotron*. Acceleration is done at one or more sites along a ring and the particle can make many passes through the accelerating region(s), gaining energy with every turn. The particles are steered using magnets located around the ring. The particles' orbit has a fixed radius made possible by increasing the field strength of the magnets as the particles accelerate. With the development of strong focusing, the concept that alternating focusing and defocusing magnets will have a net focusing effect on the beam, we can separate the three functions of the synchrotron: acceleration, steering, and focusing. The acceleration is typically done in straight sections with microwave frequency cavities. The steering is handled with magnetic dipoles and the focusing is done with quadrupole and higher multipole magnets. Most accelerators that operate on the higher end of the energy spectrum are synchrotrons.

2.2 Particle Production

Relativistic kinematics allows for the production of new matter through the conservation of energy and momentum. Colliding particles at high energy and examining the particles that are produced as a result is the primary way particle physicists investigate fundamental particles and their interactions.

2.2.1 Fixed Target

One way to collide matter is to use particles to strike a target material. This was the mode of operation for many years in the field. The Bevatron (named for its ability to impart billions of electron-volts of energy) at Lawrence Berkeley National Lab (LBNL) was a machine that accelerated protons into a fixed target. The first antiproton was discovered using the Bevatron at LBNL. As an example of relativistic kinematics and the creation of a particle we can calculate the minimum energy required to produce a proton-antiproton pair. The reaction can be written as follows:

$$p + p \rightarrow p + p + p + \bar{p}. \tag{2.3}$$

Having just enough energy to create a proton-antiproton pair would mean there would be no extra energy left over for the kinetic energy of the products. It may be hard to formulate conditions for this in the frame of reference of the lab but it is relatively easy in the center of momentum (CoM) frame, where the total momentum of the system is zero. In this frame after the collision all of the products would be at rest. To solve this problem we can use the Lorentz invariance of the dot product of two *four-vectors*, vectors in four dimensional space-time. This means that the dot product of two four-vectors is the same in any frame of reference. Four-momentum, P_μ, is a four-vector with components of energy and three spatial components of momentum. The conservation of energy and momentum must be satisfied and appears as the conservation of four-momentum. We begin by writing P_μ in the lab frame before the collision and $P^{'}_\mu$ after the collision in the CoM frame:

$$P_\mu = \begin{pmatrix} E+m \\ |p| \\ 0 \\ 0 \end{pmatrix} \qquad \text{and} \qquad \mathrm{P}^{'}_\mu = \begin{pmatrix} 4m \\ 0 \\ 0 \\ 0 \end{pmatrix} \tag{2.4}$$

where E and p are the energy and momentum of the incident particle and m is the mass of the proton. Because they are expressed in different frames of reference P_μ and $P^{'}_\mu$ are not equal. We can remedy this by using the Lorentz invariance of the dot product of two four-vectors:

$$P^{\mu}P_{\mu} = \begin{pmatrix} E+m & |p| & 0 & 0 \end{pmatrix} \begin{pmatrix} E+m \\ -|p| \\ 0 \\ 0 \end{pmatrix} = (E+m)^2 - |p|^2 \tag{2.5}$$

$$P'^{\mu}P'_{\mu} = (4m)^2. \tag{2.6}$$

By setting Equations 2.5 and 2.6 equal and using the relativistic energy-momentum relation $E^2 = |p|^2 + m^2$ to eliminate $|p|$, we get the result that the incident proton must have a kinetic energy equal to *six* times its rest mass, approximately 6000 MeV. This is very close to the Bevatron's operating energy when the antiproton was discovered there in 1955[3].

This exercise illustrates a major disadvantage of fixed target experiments; much of the initial kinetic energy is unavailable for creating new mass. The rest energy of six protons is needed to create two. In a sense this energy is 'wasted' in the kinetic energy of the final products. What if the center of momentum frame was the lab frame? It would then be possible to create particles at rest in the lab frame without wasting any energy! While fixed target experiments certainly still have their use, if you want the most energy available for particle creation you better build a collider.

2.2.2 Collider

Colliders solve the problem of fixed target experiments by having the CoM frame coincide with the lab frame. If we assume that the protons collide head-on with an equal kinetic energy the four-momenta in the lab frame before and after are:

$$P_\mu = \begin{pmatrix} 2(E+m) \\ 0 \\ 0 \\ 0 \end{pmatrix} \qquad \text{and} \qquad \mathrm{P}^{'}_{\mu} = \begin{pmatrix} 4m \\ 0 \\ 0 \\ 0 \end{pmatrix}. \tag{2.7}$$

Repeating the calculation in Section 2.2.1 we find that if each proton is given a kinetic energy equal to its rest mass (≈ 940 MeV) we can create a proton-antiproton pair. This is indeed much less energy than is required by an equivalent fixed target experiment.

While it is illustrative to think of colliding two single particles, reality makes this difficult if not impossible. We instead rely on accelerating many particles at a time in a beam and colliding beams instead of individual particles. An important quantity in colliding beam experiments is the *instantaneous luminosity* L, the number of particles passing through a plane per unit time per unit area. The higher the instantaneous luminosity, the more chances there are for interactions to occur. The luminosity of a particular beam of particles is dependent on the physical aspects of the beam, e.g. its size, particle composition, and number of particles. Related to luminosity is the concept of a *cross section*, usually denoted by σ, with units of area. The term comes from scattering experiments where particles are impinged on a hard sphere. A scattering event will occur if the incident particle is within a circular area, the hard sphere's cross section. Collisions in particle physics are not as simple as a collision with a hard sphere, but the term has stuck. Interaction boundaries are fuzzy so direct contact is not necessary for an interaction to occur, unlike the hard sphere scattering. Additionally, there are a variety of outcomes each with their own probability due to the quantum mechanical nature of the interaction. For these reasons, the cross section is not a physical description of the size of a particle, but rather an *effective* cross section of a clearly-defined process. A process with a small cross section is a rare event; the probability for it to occur is small. Knowing the instantaneous luminosity and a process you are interested in, it is possible to calculate how many of those events you can expect per unit time:

$$\frac{dN}{dt} = \sigma L \tag{2.8}$$

where N is the number of events. Integrating both sides of Eq. 2.8 tells us that we can expect N events equal to the cross section multiplied by the *integrated luminosity*, $L_{int} = \int L\,dt$. One important thing to note is that the cross section for a process can be measured at any colliding experiment provided you can measure the luminosity and count the number of events.

2.2.3 Colliding Particles

There are many things to consider when deciding what type of particles to collide. Maybe the most important of these is choosing a relatively long-lived and charged particle. It is important to use long-lived particles that will not decay before they have a chance to collide. This is especially important in cyclic colliders where the beams may be in rotation for hours. Having a charged particle is necessary because accelerating the particles is done using electromagnetic fields or magnetic fields. Protons and electrons are both charged and very stable particles that are good candidates for colliders.

Another consideration is whether the particle is point-like or composite. Colliding point-like particles like electrons is a much cleaner process than colliding protons because there are fewer particles in the final state. Protons have three valence quarks and typically only one quark is involved in a collision, the rest recombine to form additional particles. These additional particles not involved in the main interaction nonetheless leave signatures in the final state and are detected with those produced in the main interaction. Weeding out these additional particles is difficult and the precision of the measurement suffers. Additionally, it is difficult to accurately calculate the energy of the collision because the total energy of the particle is divided by the constituents. However, this curse is also a gift; there are more types of interactions possible with composite particles. If the goal is precision measurements then electrons are the way to go. If on the other hand the goal is discovery of new physics then protons are the particle of choice.

So far we've assumed that both particles in the collision are identical particles. Another possibility is the use of antiparticles: particles with the same mass but opposite charge. In some ways this can simplify the design of the particle accelerator. The particles and antiparticles can share the same beam pipe and the same electromagnetic fields will accelerate them in opposite directions. Having identical particles as the colliding particles will require a more complicated accelerator complex. At relatively low energies there is an additional benefit to using protons and antiprotons due to the energy carried by the constituent quarks. At collision energies up to ~ 3 TeV, most of the energy is carried by the three valence quarks with minimal energy carried by the sea quarks and gluons. It is more likely then to get an annihilation event by colliding a proton with an antiproton. At higher energies the sea quarks and gluons get a higher percentage of the energy and the benefit of using antiparticles is reduced. This is fortunate in a way because antiparticles are very hard to produce and store.

Requiring a charged particle does have a downside for cyclic colliders: synchrotron radiation. This is a source of energy loss that is proportional to the charge and energy of the particle and inversely proportional to the particle mass and radius of the curve. Colliding very light, charged particles at very high energy means a very large accelerator. Taking into account all these factors to minimize the energy loss is a balancing act.

2.3 Particle Detection

To learn about particles and their interactions we must have a way to observe them. Traditional methods of observation are not feasible and we must rely on their interactions with matter to learn about them. Like particle acceleration, particle detection relies heavily on charged particle interactions. The next section briefly overviews high energy particle interactions with matter focusing on electromagnetic interactions and introduces particle showers. Section 2.3.2 gives an overview of the basic structure of a particle detector.

2.3.1 Matter Interactions

All energetic charged particles interact with matter via the electromagnetic force, which is mediated by photons. These interactions result in the loss of kinetic energy. These interactions can either be with orbital atomic electrons or with atomic nuclei. An interaction with an orbital electron can result in excitation or ionization. Excitation occurs when the orbital electron gains energy from the passing charged particle and is promoted to a higher energy orbital. Following excitation, the orbital electron relaxes back to a lower energy orbit and emits a photon in the process. When the energy gained from the passing charged particle exceeds the binding energy of that electron, ionization occurs and the electron becomes unbound. In an interaction with an atomic nucleus the charged particle may radiate a photon as it decelerates, referred to as bremsstrahlung[2]. The characteristic length associated with

---

[2] In German, literally "braking radiation".

this type of process is the radiation length X_0, both the mean distance through which a high energy electron loses all but $1/e$ of its energy and 7/9 of the mean free path for a high energy photon. A charged particle can also scatter off of a nucleus, losing almost no energy in the process, and be deflected. This type of scattering is collectively referred to as *coulomb scattering*. The precise mechanism by which particles lose energy and the amount of energy lost depends on the mass of the particle, its momentum, and the material. For our purposes, we divide our discussion between heavy[3] charged particles, electrons, and photons.

Heavy charged particles interact electromagnetically through ionization and excitation. The mean energy loss rate for heavy charged particles can be approximated by the Bethe formula which depends on the material, the velocity of the incident particle ($\beta = v/c$), and the mass of the incident particle at high energy. This formula is valid within a few percent for values of $\beta\gamma$ ($\gamma = 1/(\sqrt{1-\beta^2})$) between 0.1 and 1000. The mean energy loss rate vs $\beta\gamma$ for several materials is shown in Fig. 2.4.

The Bethe formula cannot be applied to electrons and positrons because of their relatively small mass and the fact that electrons that are ionized or excited must be taken as *identical* particles to the incident electron. At high momenta another energy loss mechanism becomes dominant. The energy dissipated through bremsstrahlung is inversely proportional to the square of the mass of the incident particle. Due to their small mass, electrons lose far more energy to bremsstrahlung than any other charged particle. With this taken into account, the mean energy loss rate would look similar to those in Fig. 2.4 with a steep rise at higher $\beta\gamma$ to account for bremsstrahlung and other radiative losses.

Although the photon does not carry a charge, it can interact electromagnetically as the mediator of the electromagnetic force. A photon can be absorbed by an orbital electron

---

[3] 'Heavy' particles here refer to those more massive than the electron.

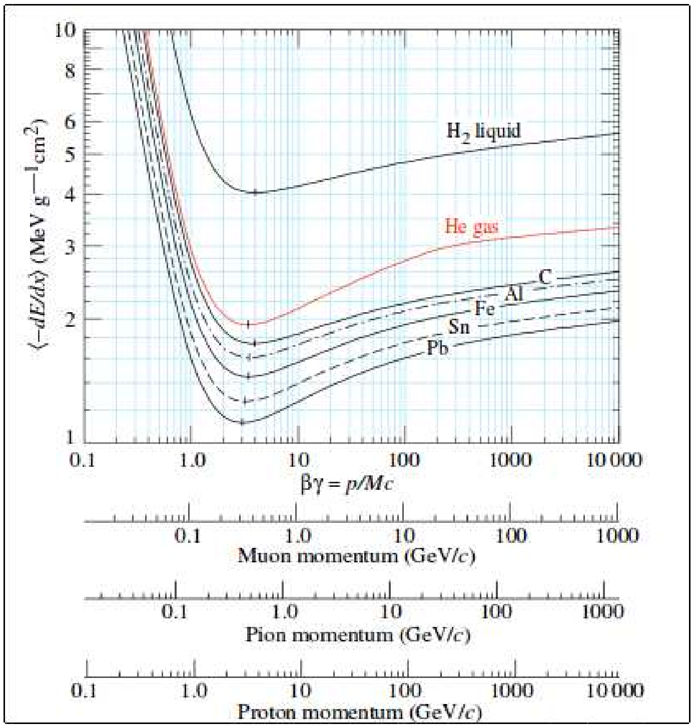

Figure 2.4: *Mean Energy Loss Rate*
Plot of the mean energy loss rate as a function of $\beta\gamma$ for several different materials. Example: a heavy charged particle with $\beta\gamma = 1.2$ would have a mean energy loss rate of ≈ 1.1 MeV cm^2/g in lead. In more intuitive units, multiplying by the density of lead gives an energy loss of 12.5 MeV per centimeter of lead traveled[4].

and either be re-emitted or, if the energy exceeds the binding energy, free the electron from its bound state. In the presence of the electromagnetic field of an electron or a nucleus a photon can convert into an electron-positron pair provided it has an energy greater than 1.02 MeV, twice the mass of an electron. At high energy photons primarily lose energy via pair production in the field of a nucleus and to a lesser extent in the field of an orbital electron.

As far as we can tell, nature has determined that quarks and gluons must be confined in hadrons as detailed by the theory governing the strong force. The property of *confinement* will be discussed in further detail in Chapter 3 but for our purposes here it is sufficient to grant its existence. The result of this property is that any gluons or quarks produced in the collision immediately form hadrons or 'hadronize' by combining with quark-antiquark pairs from the vacuum. Hadrons, whether charged or neutral, can interact with matter via the strong force. The characteristic distance in this type of interaction is the nuclear interaction length λ_A and is the mean distance a hadronic particle travels before interacting with a nuclei in the material.

When enough material is present and the particle's energy is high enough a *particle shower* can form. Incident particles, whether charged or neutral, interact with matter and produce secondary particles. If the energy imparted to the secondaries is large, they can also interact and produce additional particles. This continues until the resulting particles do not have enough energy to produce new particles. These particles continue to lose energy via ionization and excitation until they are captured or absorbed into the material. Two types of showers occur in a particle detector: electromagnetic showers and hadronic showers.

EM showers begin with a high energy photon or electron. An electron, perhaps, interacts with a nucleus and emits a photon. This photon then produces an electron-positron pair and each emit a photon through bremsstrahlung. The shower continues in this manner until the energy has decreased below the point at which pair production or bremsstrahlung is the dominant mode of energy loss. The particles continue to lose energy by other methods. The characteristic length scale of shower formation is the radiation length X_0.

Hadronic showers begin with a high energy hadron. The hadron interacts with the nuclei of the detector material producing more quarks and gluons which immediately hadronize. Secondary particles with enough energy continue to interact until their energy is too low and they are captured by the detector material. The shower depth scales as the nuclear interaction length λ_A. Because λ_A is in general larger than the radiation length, hadronic showers take longer to form than EM showers. It happens then that electromagnetic showers occur within hadronic showers when secondary particles interact electromagnetically.

It is worth noting here that of all the particles, neutrinos are the only ones that don't interact via the electromagnetic or strong force. They only interact via the weak force which has a very short interaction range. Neutrinos can therefore pass through large amounts of matter without interacting and remain undetected by most multipurpose detectors. Their existence is inferred from the momentum imbalance or missing transverse energy $\not{E}_T$ in particle collisions.

2.3.2 Detectors

The second piece of equipment necessary for a particle physics experiment is a detector. The detector acts as a camera that records information about the collision and the particles that were created. Because the design of cyclic accelerators allows for multiple interaction points, it is common for there to be multiple detectors at each of these accelerator complexes. Detectors are roughly cylindrical in shape and are situated around the collision point. To maximize the number of physics studies that can be done most detectors are general purpose – they are designed to detect many different types of signatures.

All detector components make use of electromagnetic interactions, especially ionization and excitation, to obtain information on passing particles. Ionization results in a free electron and a positive ion generally referred to as a *hole*. These electron-hole pairs can be collected and the charge measured. Photons emitted during excitations can be measured as light in a plastic scintillator. Tracking systems for multipurpose detectors are developed to trace the path of a particle without disturbing its trajectory by using small amounts of low atomic number and low atomic mass material. The particle momentum can be measured for charged particles by measuring the curvature of their track in a magnetic field. Calorimeters are used to measure the energy of a particle by initiating particle showers with high density materials and measuring the total energy deposited by charge collection or scintillation light.

Physical objects can be defined by the tracks they leave and the energy they deposit in the detector. Figure 2.5 depicts how different particles react with detector subsystems. Reconstructing particles from their signatures in the detector is the final step in obtaining physics data for analysis.

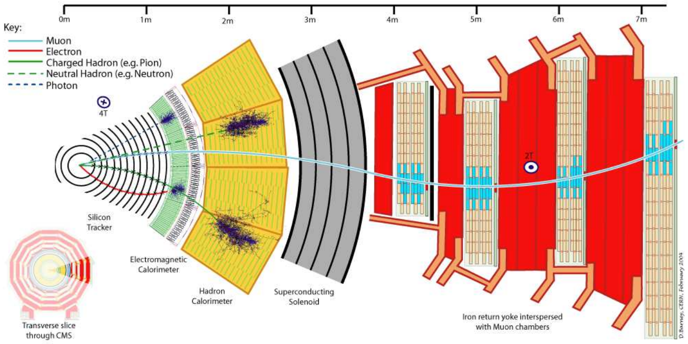

Figure 2.5: *Particle Detector Signatures*
Cartoon describing the types of signatures left by particles in a detector. The detector pictured here is the CMS detector.

2.4 Simulation

Once particle physicists have collected data and reconstructed objects it is up to them to analyze the data. The collected data is composed of many different processes in proportion to their cross sections. To look for (or perhaps stumble upon) new processes or even to test the standard model, particle physicists must be able to categorize and model the processes that make up the data. One very important tool is the construction of artificial events simulating known physical processes. There are two steps to creating these events: generation and propagation.

2.4.1 Generation

Simulated events are generated using the Monte Carlo method and as a result are commonly referred to as *Monte Carlo events* or MC events. The Monte Carlo method as it pertains to particle physics is a computational algorithm that randomly samples probability distributions governing the outcome of events. Repeating the random sampling many times creates a sample of events representative of all outcomes. First, a process is chosen that is defined by a model either the SM or otherwise. An example would be the production of a single top quark in association with a b quark, shown in Fig. 2.6. When colliding protons and antiprotons, the initial state particles must come from the constituent quarks and gluons. The momenta of the initial state particles are chosen at random from the corresponding *parton distribution function* (PDF). The PDF describes the momentum fraction of the proton carried by the partons as well as quark flavor content. Finally, the initial particles' momenta determine the possible final state momenta and one is selected at random.

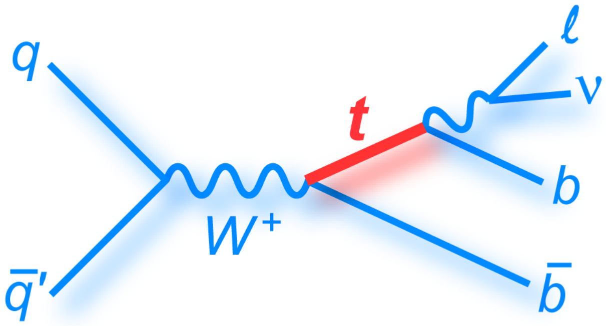

Figure 2.6: *Single Top Quark Production*
One of the Feynman diagrams for single top quark production at tree-level.

2.4.2 Propagation

After simulating the physical process what remains is simulating how it propagates and interacts with the detector. A whole host of events take place after the interaction. Particles can radiate photons or gluons, short-lived particles will decay and share their momentum with their decay products, and any quarks or gluons in the final state will immediately hadronize. The hadronization and radiation aspects are modeled by *showering* programs. All of these particles and their decay products will propagate from the interaction point outwards with trajectories that are determined from the momentum and the magnetic field within the detector. The particles that make it to the detector volume, most of which are stable, will interact with the detector material as described in Section 2.3.1. A model of the detector is constructed for this purpose and includes the active material, support structures, magnetic fields, detection thresholds and efficiencies, and geometric structure. Particles are propagated through the detector model and their interactions are recorded in the same format as real data.

Chapter 3

Theory

3.1 Introduction

In studying fundamental particles and their interactions it becomes necessary to move away from describing dynamics as systems of *particles* and towards systems of *fields*. While there are several reasons this becomes apparent perhaps the easiest way to come to terms with this is realizing that there is no reason to assume a relativistic process can be described by a single particle alone. Einstein's mass-energy relation $E = mc^2$ allows for the production of particle/antiparticle pairs. Other *virtual* particles, allowed to exist by Heisenberg's uncertainty principle $\Delta E \cdot \Delta t \geq \frac{\hbar}{2}$ for very short times, can appear in second order calculations. It makes the most sense then to instead describe systems of fields. This chapter will describe the field theories of particle physics.

In nature we know of four fundamental forces:

strong force responsible for the binding of quarks in hadrons; the residual effects of this force bind the protons in a nucleus

electromagnetic force that governs the interactions between charged particles

weak force that accounts for processes such as nuclear beta decay and the decay of the muon

gravitational force that results in planetary orbits

During the classical era in particle physics when all matter was perceived as nothing more than protons, neutrons and electrons, the two known forces were electromagnetism and gravity. This was due to the infinite range of the electromagnetic and gravitational forces. The strong and weak forces on the other hand have a very short range so were not recognizable until it was possible to examine objects on a very short length scale. We shall see that each of these forces (with the possible exception of gravity) is mediated by the exchange of one or more particles. These force carriers can be thought of as messengers between two particles that tell them how to interact through the force. We will also see that two of these forces are actually different aspects of a single force. All of these forces have a relativistic description. Three of them have a quantum description; their force carriers are the *quanta* of the field. Gravity presents a bit of a problem. Unlike the other forces, there is no satisfactory quantum theory of gravity at present and no force carrier has yet been discovered. For this reason, it will not be discussed in the following chapters. The next section gives an overview of the particle types and families in the standard model. Section 3.2 describes the quantum field theories that made up the standard model in particle physics. An overview of the searches for the Higgs boson is given in Section 3.3. A discussion of what physics may exist beyond the standard model is given in Section 3.4.

3.1.1 Particle Zoo

Before we dive into the description of the standard model theories, it is helpful to give an overview of the many types of particles, both composite and fundamental, that exist in the SM.

Fundamental particles can be divided into quarks, leptons, and mediators. Quarks are the building blocks of protons, neutrons, and other particles like them. The group of leptons include the familiar electron and neutrino. The most recognizable mediator is the photon, the light quantum. The six quarks and six leptons are divided into three families of two each differing only in mass. The first family consists of the *up* quark (u), the *down* quark (d), the electron (e), and the electron neutrino (ν_e). This family is all that is needed to make the ordinary matter around us: protons, neutrons, nuclei, and atoms. Table 3.1 gives the names and symbols for the three families of quarks and leptons.

	Quarks		Leptons	
First Family	up down	u d	electron electron neutrino	e ν_e
Second Family	charm strange	c s	muon muon neutrino	μ ν_μ
Third Family	top bottom	t b	tau tau neutrino	τ ν_τ

Table 3.1: *Three Particle Families*
A list of the quarks and leptons in each of the three families.

One attribute of particles is the intrinsic quantum number *spin*. Spin does not represent any sort of motion with respect to an axis, but is an intrinsic property of a particle. You can divide the group of all particles into two categories based on spin: fermions and bosons. Fermions have half-integer spin while bosons have integer spin. The difference in spin leads to a very strange property. Fermions follow the Pauli exclusion principle: no two identical particles can occupy the same state. Bosons do not follow this rule and arbitrarily many bosons can occupy the same state. All leptons and quarks are fermions and all force mediators are bosons.

Parity (P) is another intrinsic quantum number of particles. It refers to how the particle wavefunction transforms under a parity operation. In four-dimensional space-time a parity operation is the complete inversion of the three spatial components:

$$\mathbf{P}: \begin{pmatrix} t \\ x \\ y \\ z \end{pmatrix} \rightarrow \begin{pmatrix} t \\ -x \\ -y \\ -z \end{pmatrix}. \tag{3.1}$$

Assuming an eigenstate $\psi_{\mathbf{P}}$ of the parity operator $\mathbf{P}$ and using the fact that two applications of the parity operator leave the state unchanged (with the exception of a phase) $\mathbf{P}^2\psi_{\mathbf{P}} = e^{i\phi}\psi_{\mathbf{P}}$ we see that $\mathbf{P}\psi_{\mathbf{P}} = \pm e^{i\phi/2}\psi_{\mathbf{P}}$. Intrinsic parity is therefore an eigenvalue of the parity operator with values $P = +1$ (even) or $P = -1$ (odd). The force mediators have odd intrinsic parity while the quarks and leptons are defined to have even intrinsic parity. The antiparticles of the quarks and leptons are defined to have odd intrinsic parity. Parity is a multiplicative quantum number which is conserved in the strong and electromagnetic interactions. It is violated in the weak interactions.

For reference, Table 3.2 lists all the known fundamental particles in the standard model: their symbol, mass, electric charge, spin, and parity.

3.2 Standard Model

The standard model (SM) of particle physics encompasses the relativistic quantum field theories of the strong, electromagnetic, and weak forces. It describes the unification of the electromagnetic and weak forces into the electroweak force. Its most recent triumph is the discovery of the Higgs boson, a particle predicted by the SM and also the subject of this thesis.

	Name	Symbol	Mass	Charge (e)	J^P
Quarks	up	u	$2.3^{+0.7}_{-0.5}$ MeV	$^2/_3$	$^1/_2{}^+$
	down	d	$4.8^{+0.5}_{-0.3}$ MeV	-$^1/_3$	$^1/_2{}^+$
	strange	s	95 ± 5 MeV	-$^1/_3$	$^1/_2{}^+$
	charm	c	1.275 ± 0.025 GeV	$^2/_3$	$^1/_2{}^+$
	bottom	b	4.18 ± 0.03 GeV	-$^1/_3$	$^1/_2{}^+$
	top	t	173.21 ± 0.87 GeV	$^2/_3$	$^1/_2{}^+$
Leptons	electron	e	0.511 MeV	-1	$^1/_2{}^+$
	electron neutrino	ν_e	< 2 eV	0	$^1/_2{}^+$
	muon	μ	105.7 MeV	-1	$^1/_2{}^+$
	muon neutrino	ν_μ	< 2 eV	0	$^1/_2{}^+$
	tau	τ	1776.86 ± 0.12 MeV	-1	$^1/_2{}^+$
	tau neutrino	ν_τ	< 2 eV	0	$^1/_2{}^+$
Mediators	photon	γ	0	0	1^-
	W Boson	$W^\pm$	80.385 ± 0.015 GeV	±1	1^-
	Z Boson	Z	91.1876 ± 0.0021 GeV	0	1^-
	gluon	g	0	0	1^-
	Higgs boson	H	125.09 ± 0.24 GeV	0	0^+

Table 3.2: *Fundamental Particles*
A list of all the known fundamental particles: their symbol, mass, charge, spin J, and parity P.

The standard model is a field theory and is best described using a Lagrangian formalism. The Lagrangian $\mathscr{L}$ for the SM field theory will be a function of the fields and their derivatives $\mathscr{L}(\phi, \partial_\mu \phi)$. The theories that comprise the SM are *gauge theories*; their Lagrangians are invariant under a set of local transformations that form a symmetry or gauge group. The generators of the symmetry group are described by a Lie algebra. Associated with each generator (n generators for a group of dimension n) is a vector field. The quantization of these vector fields gives rise to physical states called *gauge bosons* which are the force carriers of the SM. As we will see in the following sections the SM is a non-abelian theory with symmetry group $U(1) \times SU(2) \times SU(3)$ with a total of twelve gauge bosons. First, Sections 3.2.1 and 3.2.2 describe the field theories of the electromagnetic and strong forces.

Section 3.2.3 describes the unification of the electromagnetic and weak forces under the *Glashow-Weinberg-Salam* (GWS) theory of weak interactions. Finally, Section 3.2.4 gives an overview of electroweak symmetry breaking and an introduction to the Higgs boson.

3.2.1 Quantum Electrodynamics

Quantum electrodynamics (QED) was the first formulation of a theory of particle interactions that took into account both quantum mechanics and special relativity. It is a relativistic quantum field theory that describes the interactions between electrically charged particles. The theory was a tremendous success in explanatory and predictive power and to this day, it boasts the highest agreement with experimental data. Because it was the first theory of its kind (and, in part, because of its wild success) other quantum field theories, such as quantum chromodynamics (QCD), are modeled after it.

We begin by writing the Lorentz-invariant Dirac Lagrangian for a free electron:

$$\mathscr{L}_{\text{Dirac}} = \overline{\psi}\left(i\gamma^{\mu}\partial_{\mu} - m\right)\psi \tag{3.2}$$

where ψ is a Dirac spinor with a Lorentz-invariant adjoint $\overline{\psi} = \psi^{\dagger}\gamma^{0}$ and the γ^{μ} are the Dirac matrices $\gamma^{0} = \begin{pmatrix} 0 & 1 \\ 1 & 0 \end{pmatrix}$ and $\gamma^{i} = \begin{pmatrix} 0 & \sigma^{i} \\ -\sigma^{i} & 0 \end{pmatrix}$[1]. We then require our field to be invariant under the following transformation:

$$\psi(x) \rightarrow e^{i\alpha x}\psi(x). \tag{3.3}$$

This transformation is a phase rotation through an angle $\alpha(x)$ and it defines the symmetry

---

[1] Here the σ^{i} are the Pauli matrices $\sigma^{1} = \begin{pmatrix} 0 & 1 \\ 1 & 0 \end{pmatrix}$, $\sigma^{2} = \begin{pmatrix} 0 & -i \\ i & 0 \end{pmatrix}$, and $\sigma^{3} = \begin{pmatrix} 1 & 0 \\ 0 & -1 \end{pmatrix}$.

group $U(1)$, the *unitary* group of dimension 1. The second term in Eq. 3.2 is invariant under this transformation but the first term is not. It is unclear what the derivative of the complex field should be when the field transformation at each point in space is different. We must introduce a new derivative that transforms like the field: the *covariant derivative*. For the transformation under $U(1)$ symmetry, the covariant derivative takes the form $D_\mu = \partial_\mu + ieA_\mu$ where e is the electron charge and A_μ is a new vector field. We can identify the new vector field with the familiar electromagnetic four-potential. This is the single gauge field expected by the Lie algebra of $U(1)$ and the quantum of this field is the photon. To complete the QED Lagrangian we must include a kinetic term for the four-potential that is locally invariant and does not depend on the field. We introduce the electromagnetic field tensor $F_{\mu\nu} = \partial_\mu A_\nu - \partial_\nu A_\mu$ for this purpose. The full QED Lagrangian can then be written as:

$$\mathscr{L}_{\mathrm{QED}} = \underbrace{\overline{\psi}(i\gamma^\mu \partial_\mu - m)\psi}_{\mathscr{L}_{\mathrm{Dirac}}} - \underbrace{e\overline{\psi}\gamma^\mu A_\mu \psi}_{\mathscr{L}_{int}} + \underbrace{\tfrac{1}{4}(F_{\mu\nu})^2}_{\mathscr{L}_{\mathrm{Maxwell}}} . \tag{3.4}$$

The first term of Eq. 3.4 is just the Dirac equation we began with and the middle term describes the interaction between the field and the four-potential. Applying the Euler-Lagrange equation to the last term yields the inhomogeneous Maxwell equations. The QED Lagrangian describes the interactions of all massive spin-1/2 particles with the electromagnetic force which includes all the quarks and charged leptons.

3.2.2 Quantum Chromodynamics

Quantum chromodynamics (QCD) is the theory that describes strong interactions. Its development began with the conception of the quark model, used to explain the many mesons and baryons discovered in the '50s and '60s. The early quark model had two problems: quarks that didn't appear to obey Fermi-Dirac statistics and particles with a fractional charge could not be found. Quarks are fermions; their wavefunctions must be antisymmetric under exchange. This problem with the early quark model can be illustrated by the Δ^{++} particle, a spin-$3/2$ particle with charge +2. This particle can be explained as a bound state of three up quarks with parallel spin – symmetric in flavor and spin. To solve this, it was proposed that an additional (hidden) quantum number was carried by quarks and that all baryons were antisymmetric in this hidden quantum number. This quantum number is called *color* and it represents an internal $SU(3)$ symmetry.

Closely related to the second problem with the early quark model is the discovery that electron-proton scattering exhibited *Bjorken scaling* [2]; at high enough energies (or a short enough timescale) the constituents of the proton behaved as free particles. How is it possible then that quarks only weakly interact yet are so tightly bound that they don't exist freely in nature? The answer to this lies in *asymptotic freedom*, the cornerstone of QCD. Asymptotic freedom is a property that causes interactions between particles to become weaker at high energies and short timescales and stronger at low energies and long timescales. The Nobel Prize in physics for 2004 was awarded to Wilczek, Gross, and Politzer for their 1973 discovery of asymptotic freedom in non-abelian[3] gauge theories and their relation to strong dynamics[5, 6].

Quantum Chromodynamics is a non-abelian gauge theory with local $SU(3)$ color symmetry. In its most compact form the QCD Lagrangian looks almost identical to the QED

---

[2] Properties that exhibit Bjorken scaling are found to be independent of the energy at which the experiment is performed while depending on dimensionless kinematic quantities like a scattering angle. Named for James Bjorken who found that structure functions of nucleons exhibited this behavior, strongly implying that the nucleons had point-like substructure.

[3] Unlike the abelian gauge theory QED, the generators of a non-abelian gauge theory do not commute. It is this characteristic that allows non-abelian gauge theories to be asymptotically free.

Lagrangian:

$$\begin{aligned}\mathscr{L}_{QCD} &= \overline{\psi}\left(i\gamma^{\mu}D_{\mu}-m\right)\psi-\tfrac{1}{4}(G^{a}_{\mu\nu})^{2},\\ G^{a}_{\mu\nu} &= \partial_{\mu}C^{a}_{\nu}-\partial_{\nu}C^{a}_{\mu}+gf^{abc}C^{b}_{\mu}C^{c}_{\nu}.\end{aligned} \tag{3.5}$$

Here $G^{a}_{\mu\nu}$ is the new field strength with the index a summed over the eight generators of $SU(3)$, g is the coupling constant, and the f^{abc} are the structure constants of $SU(3)$. The covariant derivative is defined as $D_{\mu}=\partial_{\mu}-igC^{a}_{\mu}t^{a}$ where the t^{a} are the generators of $SU(3)$. The eight new vector fields C^{a}_{μ} are the gluon fields. Unlike QED, where there is only one gauge boson QCD has eight gauge bosons – the gluons. Writing out the Lagrangian more explicitly yields:

$$\begin{aligned}\mathscr{L}_{QCD} = {} & \underbrace{\overline{\psi}\left(i\gamma_{\mu}\partial_{\mu}-m\right)\psi-\tfrac{1}{4}(\partial_{\mu}C^{a}_{\nu}-\partial_{\nu}C^{a}_{\mu})^{2}}_{\textit{free field}}+\underbrace{gC^{a}_{\mu}\overline{\psi}\gamma^{\mu}t^{a}\psi}_{\textit{fermion}}\\ & -\underbrace{gf^{abc}(\partial_{\nu}C^{a}_{\mu})C^{\nu b}C^{\mu c}}_{\textit{three-vertex}}-\underbrace{\tfrac{1}{4}g^{2}(f^{eab}C^{a}_{\nu}C^{b}_{\mu})(f^{ecd}C^{\nu c}C^{\mu d})}_{\textit{four-vertex}}.\end{aligned} \tag{3.6}$$

The first term in Eq. 3.6 is the free field Lagrangian ($g=0$) that describes the dynamics of the quarks and the gauge field. The second term is the fermion interaction term; it describes the interaction between a fermion with color quantum numbers (quarks) and a gluon. The last two terms are interesting because similar terms do not appear in the QED Lagrangian. They are self-interaction terms corresponding to Feynman diagram vertices with three and four gluons. Gluons can self-interact because they themselves carry color unlike the electrically-neutral photons in QED.

3.2.3 Glashow-Weinberg-Salam Theory of Weak Interactions

Formulating a theory of the weak force interactions presents a few problems. First, it has been experimentally observed that the W boson only couples to left-handed particles. Worse, it appears that right-handed neutrinos do not exist. Second, field theories with unbroken symmetries only have *massless* gauge bosons but the masses of the W and Z bosons are certainly not zero – they are quite heavy! As we shall see in Section 3.2.4 the mechanism for giving the weak vector bosons mass involves spontaneously breaking the symmetry of the electroweak sector. The first problem can be solved in part by assigning right- and left-handed fields to different representations of the gauge group.

These difficulties are a small price to pay for the end result: a theory which gives a unified description of the electromagnetic and weak interactions. This means that the electromagnetic and weak forces are really different aspects of the same force, the electroweak force. Glashow[7], Weinberg[8], and Salam[9] (GWS) introduced the theory which describes the weak interactions and also agrees with experiment. For this they won the Nobel Prize in physics in 1979.

We begin as always by requiring a local gauge invariance. For the GWS theory it is a $SU(2) \times U(1)$ gauge invariance: $\psi \rightarrow e^{i\omega^i T^i} e^{i\beta Y}\psi$ where the T^i are the generators of $SU(2)$ with $i = 1, 2, 3$, β and ω^i are arbitrary phases, and Y is the weak hypercharge[4] of $U(1)$. For a fermion field belonging to the general representation of $SU(2)$ the covariant derivative has the form

$$D_\mu = \partial_\mu - igW^i_\mu T^i - ig'YB_\mu \tag{3.7}$$

where the W^i_μ are the vector fields of $SU(2)$ and B_μ is the vector field of $U(1)$. The kinetic

---

[4] Weak hypercharge relates the electric charge Q to the third component of weak isospin T^3 by $Q = T^3 + Y$. In fact, this equality will become evident in our discussion of electroweak theory.

energy terms in the Lagrangian for the gauge fields are

$$\begin{aligned}\mathscr{L}_{kinetic} &= -\tfrac{1}{4}W^i_{\mu\nu}W_i^{\mu\nu} - \tfrac{1}{4}B_{\mu\nu}B^{\mu\nu} \\ W^i_{\mu\nu} &= \partial_\mu W^i_\nu - \partial_\nu W^i_\mu + g\epsilon^{ijk}W^j_\mu W^k_\nu \\ B_{\mu\nu} &= \partial_\mu B_\nu - \partial_\nu B_\mu\end{aligned} \tag{3.8}$$

which are similar to the kinetic terms in QED and QCD. We now incorporate the fact that the W bosons only interact with left-handed fermions by assigning the left-handed fermions to doublets of $SU(2)$ and right-handed fermions to singlets of $SU(2)$. To reinforce the fact that the doublets and singlets belong to different representations of $SU(2)$ we will denote the doublets as ψ_L and the singlets as χ_R. The singlets of $SU(2)$ only interact with the B_μ field leading to the Lagrangian $\mathscr{L}_R = i\overline{\chi}_R\gamma^\mu(\partial_\mu - ig'YB_\mu)\chi_R$. The doublets interact with both fields $\mathscr{L}_L = i\overline{\psi}_L\gamma^\mu(\partial_\mu - igW^i_\mu T^i - ig'YB_\mu)\psi_L$. The values of the charge Y are determined by the species of fermion. The quark fields consist of one left-handed doublet $Q_L = \left(\begin{smallmatrix} u \\ d \end{smallmatrix}\right)_L$ and two right-handed singlets u_R and d_R. Similarly for the leptons, $E_L = \left(\begin{smallmatrix} \nu_e \\ e^- \end{smallmatrix}\right)_L$ and e_R. It is tempting to assign the three gauge fields W^i_μ to the three weak vector bosons $W^\pm$ and Z and the B_μ field to the photon but that would imply that the Z boson does not couple to right-handed fermions and this is not the case. The role of W^i_μ and B_μ in producing the vector bosons is made clear if we instead write Eq.3.7 in terms of the mass eigenstates of the fields. For this we need to break the symmetry of the GWS theory.

3.2.4 Electroweak Symmetry Breaking

The method of generating gauge boson masses through spontaneous symmetry breaking was first[5] described independently by Higgs[10]; Brout and Englert[11]; and Guralnik, Hagen, and Kibble[12]. In 2013 Higgs and Englert won the Nobel Prize in physics for this work. Spontaneous electroweak symmetry breaking (EWKSB) can be incorporated into the GWS theory.

To break the electroweak symmetry spontaneously we introduce a doublet of complex scalar fields

$$\Phi = \frac{1}{\sqrt{2}} \begin{pmatrix} \phi^+ \\ \phi^0 \end{pmatrix} \tag{3.9}$$

$$\text{with} \qquad \phi^+ = \phi_1 + \mathrm{i}\phi_2 \qquad \text{and} \qquad \phi^0 = \phi_3 + \mathrm{i}\phi_4$$

with a self-interaction potential of the form $V(\Phi) = \mu^2\Phi^\dagger\Phi + \lambda(\Phi^\dagger\Phi)^2$. To preserve the symmetry of the electromagnetic sector we assign the scalar field a hypercharge Y of $+1/2$ which fixes the electromagnetic charges of the components of Φ. The covariant derivative of Φ follows from Eq. 3.7: $D_\mu\Phi = (\partial_\mu - i\frac{g}{2}W^i_\mu\sigma^i - i\frac{g'}{2}B_\mu)\Phi$ where T^i has been expanded as $\frac{\sigma^i}{2}$. We can write the Lagrangian as a kinetic term and a potential term

$$\begin{aligned} \mathscr{L} &= |D_\mu\Phi|^2 - V(\Phi) \\ &= \underbrace{|D_\mu\Phi|^2}_{\text{kinetic term}} - \underbrace{\mu^2\Phi^\dagger\Phi - \lambda\left(\Phi^\dagger\Phi\right)^2}_{\text{potential terms}}. \end{aligned} \tag{3.10}$$

Let's first look at the potential terms in the Lagrangian. Assuming $\mu^2 < 0$ and $\lambda > 0$, one component of the potential $V(\Phi)$ is plotted in the imaginary plane in Fig. 3.1 with

---

[5] Spontaneous symmetry breaking in an abelian gauge theory had already been used to explain the Meissner effect in superconductivity. The application to non-abelian gauge theories and the implications to particle physics was what was first described by Higgs, *et al.*

arbitrary units. The minimum of this potential is a circle in the complex plane: $v = \pm\sqrt{\mathrm{Re}^2(\phi) + \mathrm{Im}^2(\phi)} = \pm\sqrt{-\mu^2/\lambda}$ with another critical point at $\phi = 0$. The vacuum (or ground state) expectation value (vev) of the field ϕ will occur at a minimum in the potential. Since the ground state is degenerate the field will spontaneously choose and the symmetry will be broken. We will consider the positive solution. For the doublet scalar field Φ we choose $\phi_1 = \phi_2 = \phi_4 = 0$ and $\phi_3 = v$. In this case the positively-charged component ϕ^+ is zero and only the real part of the neutral component is non-zero. To simplify the discussion, we will work in the *unitarity gauge*, a choice of gauge that reduces the scalar field to one physical degree of freedom. Next, we consider small oscillations about the minimum and write

$$\Phi(x) = \frac{1}{\sqrt{2}} \begin{pmatrix} 0 \\ v + h(x) \end{pmatrix} \tag{3.11}$$

where $h(x)$ is a real field in our gauge choice. We can now evaluate the Lagrangian in the ground state.

$$\begin{aligned} \mathscr{L}_V &= -\mu^2 h^2 - \lambda v h^3 - \frac{1}{4}\lambda h^4 + \frac{1}{4}\mu^2 v^2 \\ &= -\frac{1}{2} m_h h^2 - \sqrt{\frac{\lambda}{2}} m_h h^3 - \frac{1}{4}\lambda h^4 + \frac{1}{4}\mu^2 v^2. \end{aligned} \tag{3.12}$$

The first term in the Lagrangian is a mass term for the h field, $m_h = \sqrt{2}\mu$. This represents a particle with non-zero mass, which we refer to as the Higgs boson. Notice that the mass for the Higgs boson is not specified; it depends only on unknown parameters.

Looking at the kinetic energy term of Eq. 3.10 we see that it takes the form of the covariant derivative of ϕ, squared. Since the symmetry has been broken we can evaluate this

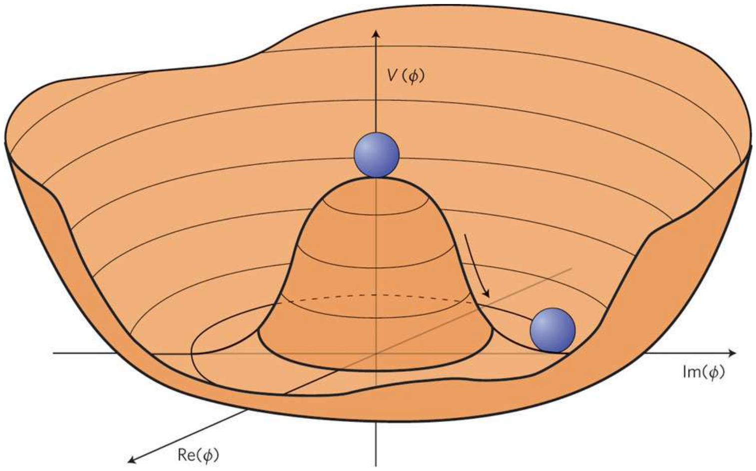

Figure 3.1: *Scalar Potential*
The potential $V(\phi) = \mu^2\phi^\dagger\phi + \lambda(\phi^\dagger\phi)^2$ assuming $\mu^2 < 0$ and $\lambda > 0$ for a complex scalar field plotted in arbitrary units[13].

term at the vev of ϕ. At this point we can evaluate the product explicitly:

$$|D_\mu\phi|^2 = \frac{1}{2}(\partial_\mu h)^2 + \frac{1}{2}\frac{v^2}{4}\left[g^2(W^{1\mu} - iW^{2\mu})(W^1_\mu + iW^2_\mu) + (gW^3_\mu - g'B_\mu)^2\right] \cdot \left(1 + \frac{h}{v}\right)^2 . \tag{3.13}$$

The terms inside the brackets are mass terms for the weak vector bosons. Our bosons have acquired mass! We can define them as follows.

$$\begin{aligned} W^\pm_\mu &= \frac{1}{\sqrt{2}}(W^1_\mu \mp iW^2_\mu) & m_W &= g\frac{v}{2} \\ Z_\mu &= \frac{1}{\sqrt{g^2 + g'^2}}(gW^3_\mu - g'B_\mu) & m_Z &= \frac{v}{2}\sqrt{g^2 + g'^2} \end{aligned} \tag{3.14}$$

The W bosons are actually a combination of the first two components of the W^i_μ. The Z boson, on the other hand, doesn't receive any contributions from these and is instead a combination of the third component of W^i_μ and B_μ. The photon of course remains massless and therefore does not appear in 3.13. It is also a combination of W^3_μ and B_μ and is orthogonal to Z_μ:

$$A_\mu = \frac{1}{\sqrt{g^2 + g'^2}}(g' W^3_\mu + g B_\mu) \qquad m_\gamma = 0. \tag{3.15}$$

We can write the transformation that changes (W^3, B) to (Z, A) as a rotation through the weak mixing angle θ_w:

$$\begin{aligned} \begin{pmatrix} Z \\ A \end{pmatrix} &= \begin{pmatrix} \cos\theta_w & -\sin\theta_w \\ \sin\theta_w & \cos\theta_w \end{pmatrix} \begin{pmatrix} W^3 \\ B \end{pmatrix} \\ \cos\theta_w = \frac{g}{\sqrt{g^2 + g'^2}}, &\qquad \sin\theta_w = \frac{g'}{\sqrt{g^2 + g'^2}}. \end{aligned} \tag{3.16}$$

Writing the covariant derivatives in terms of the mass eigenstates and identifying the electric charge quantum number Q as $T^3 + Y$ and the coefficient of the photon field $gg'/\sqrt{g^2 + g'^2}$ as e we obtain

$$D_\mu = \partial_\mu - i\frac{g}{\sqrt{2}}(W^\mu_+ T^+ + W^\mu_- T^-) - i\frac{g}{\cos\theta_w} Z_\mu (T^3 - \sin^2\theta_w Q) - ieA_\mu Q. \tag{3.17}$$

The fermion masses m_f are more difficult to include in the Lagrangian because the right- and left-handed fields live in different representations. Putting in a mass term in this way would violate gauge invariance. Using the Higgs mechanism we can construct these terms by contracting the fermion doublets F_L with the spinor ϕ evaluated at the vacuum expectation value. New dimensionless coupling constants are required. Again using the unitarity gauge we write

$$\begin{aligned} \mathscr{L}_{fermion} &= -\lambda_f \bar{F}_L \cdot \phi f_R \\ &= -\frac{v}{\sqrt{2}}\lambda_f (1 + \frac{h}{v}) \bar{f}_L f_R \\ &= -m_f \bar{f}_L f_R (1 + \frac{h}{v}). \end{aligned} \tag{3.18}$$

Our choice of the unitarity gauge obscures some of the underlying mechanics of the scalar field that are worth mentioning here. Looking back at Fig. 3.1, the potential takes the shape of the bottom of a champagne bottle. At sufficiently high energies the field does not see the potential and the system is symmetric. When the system is in its lowest energy state the field will 'settle' into the the minimum of the potential and the symmetry is broken. We saw that small oscillations of the field in the radial direction correspond to the massive Higgs boson. We can also consider another type of excitation in this picture: those around the vertical axis. Since there are an infinite number of equivalent minima the ground state is degenerate and oscillations around the bottom of the bottle move the system to a different, equivalent, ground state. These modes correspond to massless Nambu-Goldstone bosons. In EWKSB there are three of these Nambu-Goldstone bosons, one for each generator belonging to a broken symmetry. Being able to 'remove' them from the Lagrangian means that they are not physical states but represent extra degrees of freedom. We say that they are "eaten" by the weak vector bosons which gain an additional degree of freedom: a longitudinal polarization state.

3.3 Searching for the Higgs Boson

The mechanism of electroweak symmetry breaking discussed in the previous section predicts a massive physical particle which has been named the Higgs boson. In the standard model it is a scalar boson with zero spin and no electric or color charges. The only property not predicted by the standard model is its mass, $m_h = \sqrt{2}\mu$, which only depends on unknown parameters. It couples to all particles roughly in proportion to their mass; very light particles couple weakly to the Higgs boson. Unfortunately, most of the particles we can easily create are very light and make it difficult to observe. We can place constraints on the Higgs boson mass directly, by searching for excesses over a large mass range, or indirectly by precise mass measurements on strongly coupled particles.

Many experiments over the years have searched for the Higgs boson both directly and indirectly. The following sections briefly review searches for the Higgs boson at colliders. As regions of possible Higgs boson masses were excluded, precision measurements of the W boson and top quark masses improved. Figure 3.2 shows the measured mass of the W boson versus the mass of the top quark.

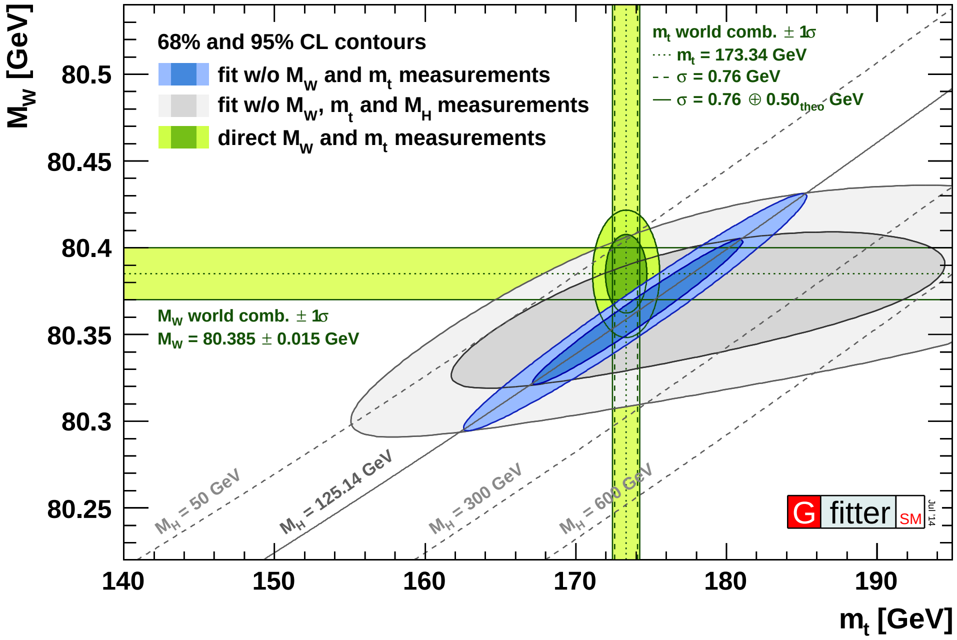

Figure 3.2: *Indirect Higgs Boson Mass Constraints*
The 68% and 95% confidence level contours resulting from a global fit using precision electroweak measurements of the mass of the W boson, the mass of the top quark, and theory calculations to constrain the mass of the Higgs boson. Also included are the measurements of the scalar boson discovered at the LHC[14].

3.3.1 LEP Searches

The Large Electron-Positron (LEP) collider at CERN collided electrons and positrons at center of mass energies between 189 GeV and 209 GeV. From 1989 to 2000 the four experiments at LEP (ALEPH, DELPHI, OPAL, and L3) collected a total of 2461 pb^{-1} of data. The decay branching ratios for the Higgs boson are plotted as a functions of the Higgs boson mass in Fig 3.3. For a Higgs boson with low mass the primary decay is to pairs of b quarks. This was the primary search mode for LEP experiments, but they also performed searches that looked for the Higgs boson decaying to pairs of vector bosons and tau leptons. The primary production mechanism considered was the Higgs boson produced in association with a Z boson in the process $e^+e^- \to ZH$. The Z boson decayed to either two quarks, two charged leptons, or two neutrinos. They were able to set a lower bound on m_h of 114.4 GeV at the 95% confidence level[15]. Figure 3.4 shows the value of CL_s as a function of the tested Higgs boson mass. Higgs boson masses are excluded if $CL_s \leq 0.05$.

3.3.2 Tevatron Searches

The Tevatron collider at Fermilab collided protons and antiprotons from 1985 to 2011 at center of mass energies up to 1.96 TeV. The experiments at the Tevatron, CDF and D0, collected up to 10 fb^{-1} per experiment. At the center of mass energy of the Tevatron the dominant Higgs boson production modes are gluon-gluon fusion, associated VH production, vector boson fusion, and associated top quark pair production ttH. Tree-level Feynman diagrams for these production modes are given in Fig. 3.5. The production cross sections for these processes are plotted over a range of Higgs boson masses in Fig. 3.6. The decay branching ratios for the Higgs boson are plotted as a function of the Higgs boson mass in

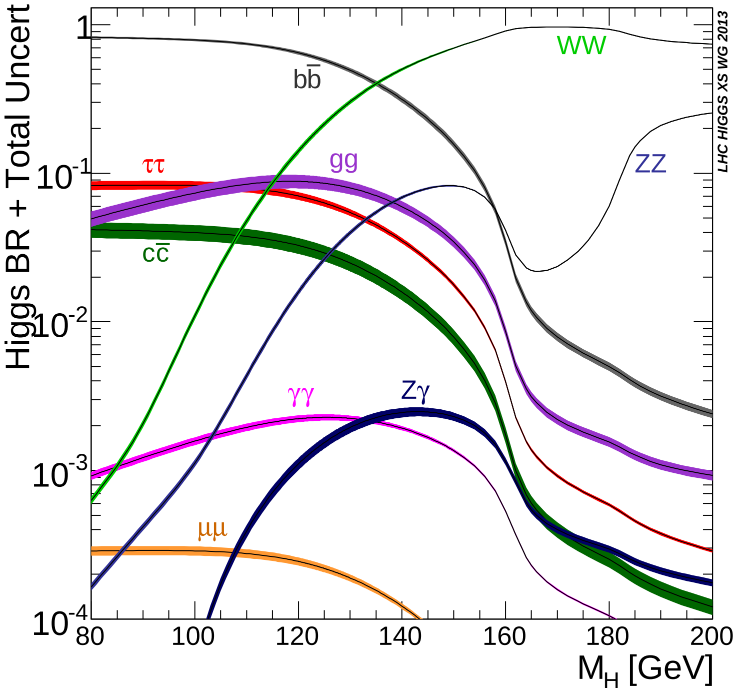

Figure 3.3: *Higgs Boson Decay Branching Ratios*
Higgs boson decay branching ratios as a function of the Higgs boson mass[16].

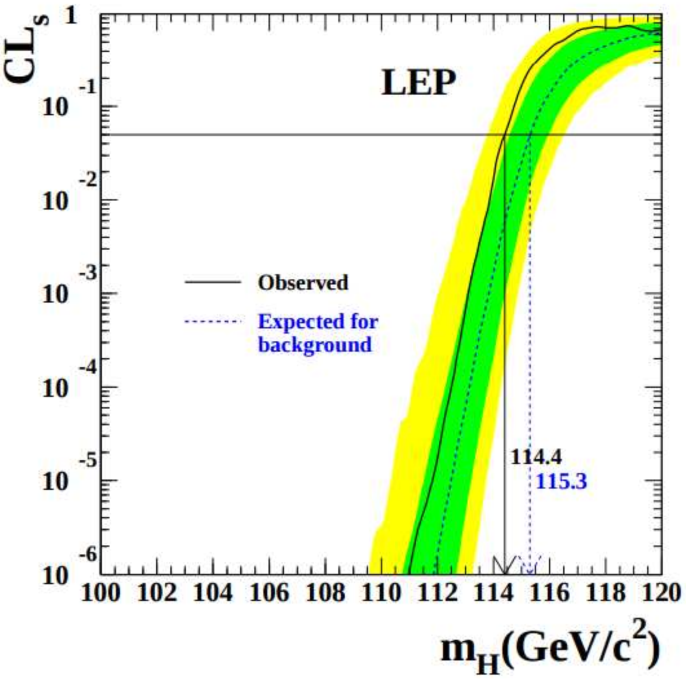

Figure 3.4: *Higgs Boson Mass Constraints from LEP*
Shown here is the value of CL_s for a range of Higgs boson masses. The yellow and green bands correspond to the 68% and 95% confidence levels for the median expected value[15].

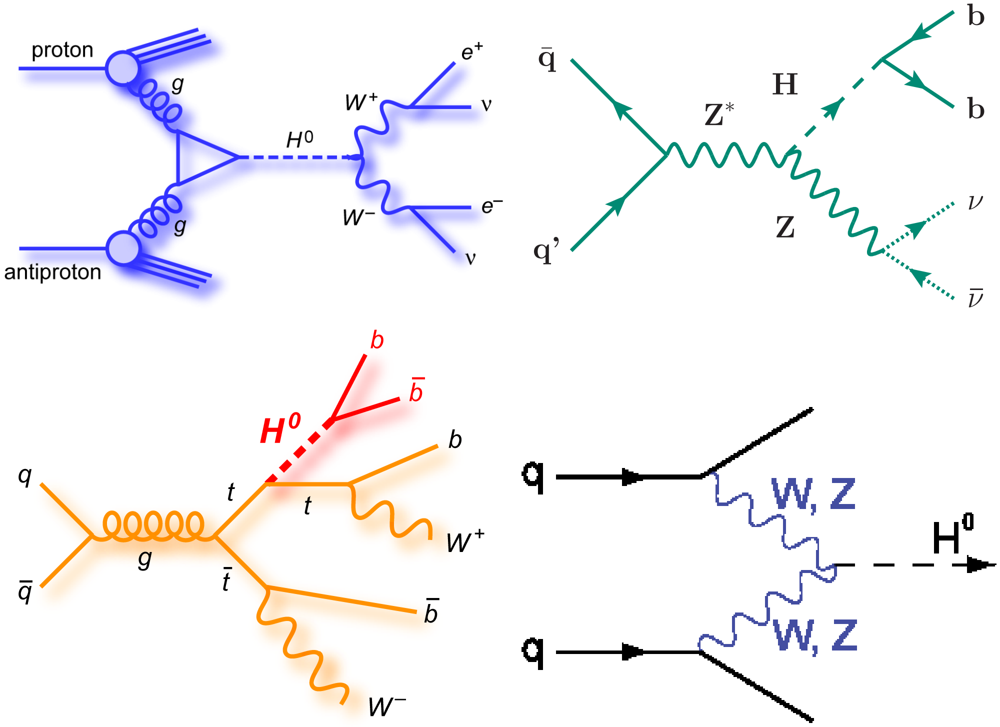

Figure 3.5: *Dominant Higgs Boson Production Modes*
Shown here are the tree-level diagrams for the dominant Higgs boson production modes at the Tevatron.

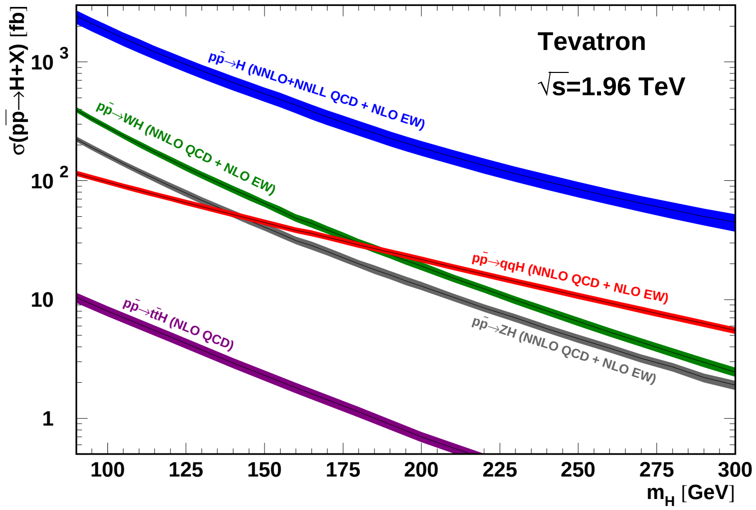

Figure 3.6: *Tevatron Higgs Boson Production Cross Sections*
Higgs boson production cross sections for gluon-gluon fusion (blue), WH (green) and ZH (gray) associated production, vector boson fusion (red), and associated top quark pair production (purple)[16].

Fig. 3.3. The most dominant decays are to a pair of b quarks up to a Higgs boson mass of 135 GeV and to a pair of W bosons at higher masses. The center of mass energy of the Tevatron restricts the mass range that can reasonably be probed to ≤ 200 GeV. Searches for the Higgs boson at the Tevatron concentrate on the production modes in Fig. 3.6 with the Higgs boson decaying to $b\bar{b}$ or to a pair of W bosons. When searching for the decay $H \rightarrow b\bar{b}$ we usually consider production modes which have leptons in the final state. Most of the interactions that occur at a hadron collider like the Tevatron produce quarks. Final states with quarks tend to get overwhelmed by these background interactions. By requiring leptons in the final state (which are rarer at hadron colliders) we can limit potential background sources.

The Tevatron was able to exclude Higgs boson masses in the ranges $90 < m_H < 109$ GeV and $149 < m_H < 182$ GeV[17] at the 95% confidence level when combining all production processes and decay modes. For a discussion of the statistical methods employed here please refer to Chapter 8. Figure 3.7 shows the observed and expected 95% confidence level upper limit divided by the standard model production cross section for a range of Higgs boson masses. When combining only VH associated production processes with the Higgs boson decaying to two b quarks we also saw evidence[6] of a new particle in the mass range $120 < m_H < 135$ which was consistent with the SM Higgs boson[18]. Figure 3.8 shows the expected and observed log-likelihood ratio as a function of the Higgs boson mass. The highest local significance is at $m_H = 120$ GeV and corresponds to 3.3 s.d. with a global significance of 3.1 s.d.

---

[6] The terms *evidence* and *observation* or *discovery* have specific connotations in particle physics. Having evidence of a new particle means that even if the particle doesn't exist, the probability of getting a result at least as extreme as the data is 0.3% corresponding to a p-value of 0.003 or a three standard deviation (s.d.) fluctuation above the background expectation. Observation or discovery corresponds to a p-value of 3×10^{-7} or a 5 s.d. fluctuation above the background expectation.

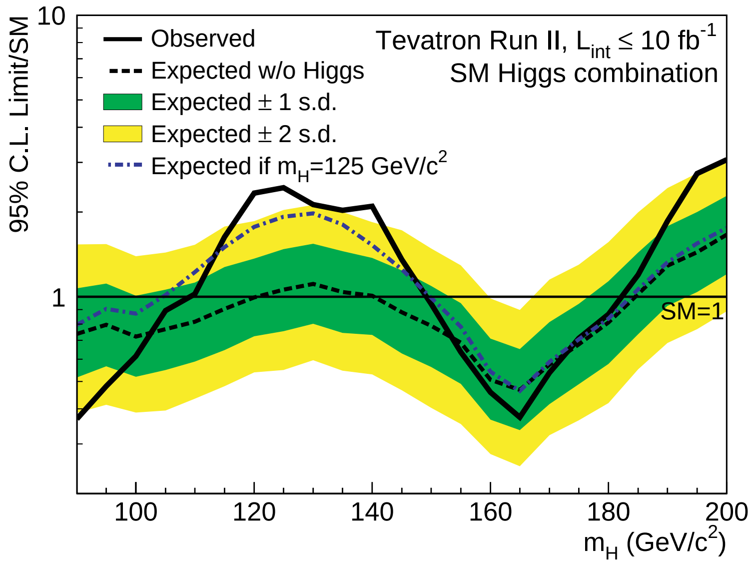

Figure 3.7: *Tevatron Higgs Boson 95% CL Limits*
Expected and observed 95% confidence level upper limits divided by the SM production cross section for a range of Higgs boson masses. The green and yellow bands correspond to 1 s.d. and 2 s.d. on the median background-only prediction.

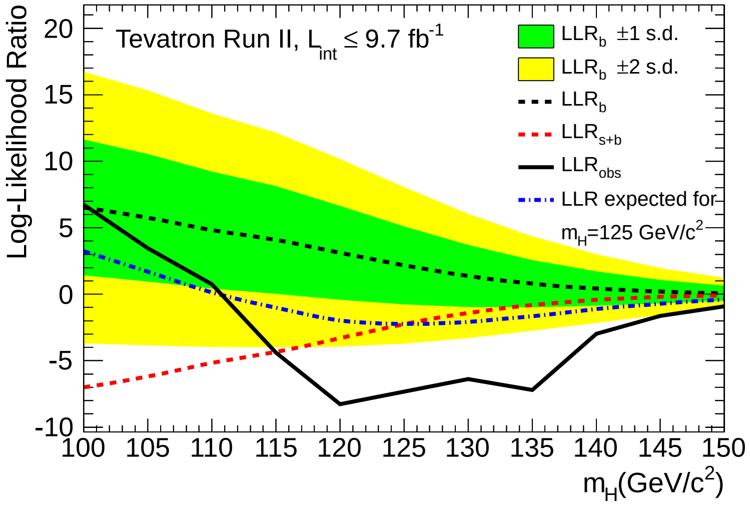

Figure 3.8: *Tevatron Log-Likelihood Ratio*
Expected and observed log-likelihood ratio (LLR) as a function of the Higgs boson mass. The green and yellow bands correspond to 1 s.d. and 2 s.d. on the median background-only prediction.

3.3.3 LHC Discovery

On July 4, 2012 it was announced that a new particle had been discovered consistent with the SM Higgs boson at the Large Hadron Collider (LHC) almost 50 years after its existence had been proposed. Both experiments at the LHC, ATLAS and CMS, were able to independently claim discovery[19, 20]. At the center of mass energies at the LHC (the discovery used data at 7 TeV and 8 TeV) choosing final states with unique signatures becomes even more important. Even though the branching ratio for the decay $H \rightarrow \gamma\gamma$ is much smaller than $H \rightarrow b\bar{b}$ its unique signature makes it much more sensitive. The discovery combined $H \rightarrow \gamma\gamma$, $H \rightarrow ZZ$, $H \rightarrow WW$, $H \rightarrow b\bar{b}$, and $H \rightarrow \tau\tau$ decay channels with most of the sensitivity coming from the first two modes. Figure 3.9 shows the local background p-value for the ATLAS and CMS experiments.

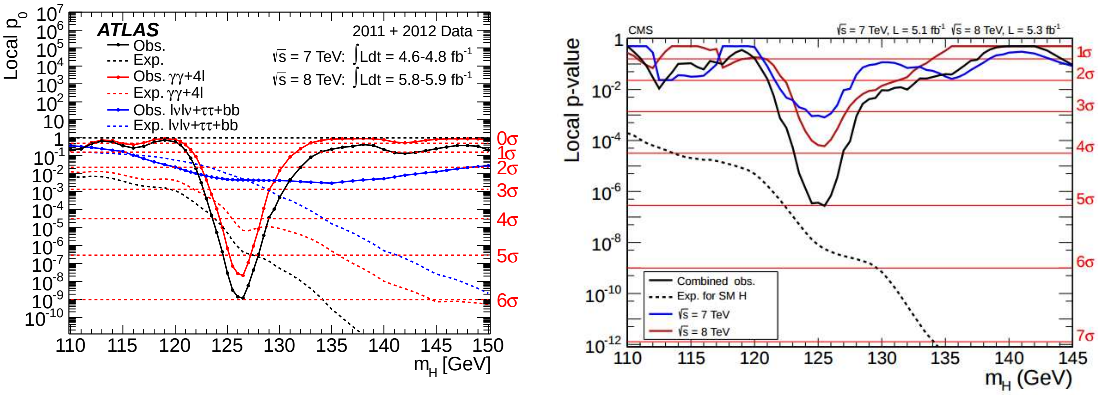

Figure 3.9: *LHC Local p-Values*
Local background p-values for the ATLAS and CMS experiments.

3.4 Beyond the Standard Model

The standard model has been a great success; its predictions have fueled experimental progress and discovery for decades. The Higgs boson was the very last of these predictions to be confirmed. However, this does not mean that the standard model is a complete theory. There are still open questions and issues that it does not address. Some of these problems are inherent, while many are external to the standard model. Below is a list of some of the problems from both categories, but it is by no means exhaustive.

There are issues which are outside the purview of the standard model. These are questions for which the standard model simply doesn't have an answer.

- **Gravity** The force of gravity is responsible for the large-scale structure of the universe. It is also the force with which we are most familiar yet it is not described by the standard model of particle physics. As of this writing there has never been a successful theory of quantum gravity.

- **Dark matter and dark energy** Cosmological studies of the matter/energy density of the universe have shown that the matter described by the standard model constitutes less than 5% of the total mass-energy content of the universe. The remaining matter content, which contributes $\approx 27\%$ does not interact electromagnetically and remains unseen. The remaining mass-energy content is an unknown type of energy which is accelerating the expansion of the universe. For this reason we refer to them as dark matter and dark energy, respectively. The particles and energies in the SM cannot account for these two strange quantities.

- **Matter-antimatter asymmetry** The abundance of matter in the universe suggests that there was an imbalance of matter and antimatter in the early universe which cannot be accounted for in the standard model.

- **Unification** In the first epoch of the universe known as the Planck era it is predicted that the gravitational force was comparable to all the other forces and that it dominated matter interactions. The energy scale at which this occurred is referred to as the Planck scale and is approximately 10^{19} GeV. It is theorized that at this scale all the forces were different aspects of a single unified force. For this to occur the coupling constants for the electroweak and strong forces would become equal at an energy scale less than the Planck scale. Unless there is new physics beyond the standard model this does not occur.

Problems inherent in the standard model are either based on disagreements between theory and experiment or are philosophical in nature.

- **Neutrino masses** In the standard model there is no way to add mass terms for neutrinos to the Lagrangian without destroying gauge invariance. The fermion mass terms in Eq. 3.18 are constructed using both the left-handed doublet and right-handed singlet states of the particles and neutrinos do not exist in a right-handed state. However, neutrino experiments have found that neutrinos undergo flavor oscillation – something that would not be possible if they did not have mass.

- **Hierarchy problem** If unification is possible at the Planck scale the SM offers no explanation as to why the Planck scale is so much higher than the other energy scales of the SM. The electroweak scale is equal to the Higgs boson vacuum expectation value of 246 GeV. From this scale all the way up to 10^{19} GeV is devoid of any interesting physics according to the standard model.

- **Fine-tuning** Quantum corrections to the third term in Eq. 3.12 produce contributions to the Higgs boson mass which are quadratically divergent. They remain finite up to the Planck energy scale but the contributions are very large. In order for the Higgs boson mass to remain small there must be very precise cancellations to the large contributions to the Higgs boson mass. This amounts to an unacceptable fine-tuning of model parameters. A model which adequately describes reality should not rely on a fine-tuning of its parameters.

All of these problems point to something *beyond* the standard model. There are many theoretical proposals on how to deal with these problems. Some involve extensions to the SM which typically include additional SM-like terms to the Lagrangian. These terms of course require additional parameters which are not predicted by the standard model. Other proposals give the theory a complete overhaul by positing some underlying structure to the standard model itself. These theories must reproduce SM predictions as well as provide new testable predictions.

Perhaps one of the most famous beyond-the-SM (BSM) theories is supersymmetry[21, 22]. Like all of the quantum field theories, supersymmetry is based on an underlying symmetry. It posits a symmetry related to particle spin and predicts a fermionic *superpartner* for every boson and a bosonic superpartner for every fermion. If supersymmetry were an unbroken symmetry (like the charge symmetry in GWS) then the superpartners would differ only by ½-spin – they would have the same mass and charges as their SM counterparts. Since this hasn't been observed we know that if supersymmetry exists it has to be a broken symmetry.

3.4.1 BSM Higgs Spin & Parity

One of the places to look for physics beyond the standard model is one of its newest discoveries: the Higgs boson. If the recently discovered boson is the SM Higgs boson it will have zero spin and even parity. There are other possibilities for the spin and parity of the discovered boson if it is not the SM Higgs boson. Many of these possibilities come from theories that solve some of the problems with the standard model, most notably the fine-tuning and hierarchy problems. A pseudoscalar with $J^P = 0^-$ is predicted for two Higgs boson doublet models of type II[23] such as those found in supersymmetry[24]. Theories postulating extra dimensions predict massive particles with tensor couplings and $J^P = 2^+$[25, 26]. Knowing the spin and parity of the discovered boson or being able to exclude specific values of J^P tells us about the structure of the underlying theory. Part II of this Thesis is designed to address this issue.

Part II

Constraints on Models for the Higgs Boson with Exotic Spin and Parity

Part II provides an in-depth discussion of the data analysis and conclusions. It begins with a description of the equipment used to produce, detect, and record the data in Chapter 4. Chapter 5 discusses the motivations behind this analysis. It includes an overview of the theoretical framework specific to analyzing the spin and parity nature of a Higgs boson at the Tevatron. The data and simulated samples used in this analysis are discussed in Chapter 6. The data analysis method is described in Chapter 7. Chapter 8 gives an overview of the statistical analysis method employed and discusses sources of systematic uncertainties. Finally, Chapters 9 and 10 discuss the results of the analysis in detail.

Chapter 4

Experimental Apparatus

4.1 Introduction

Fermi National Accelerator Laboratory[1] is a large accelerator complex. Prior to 2008 it was the site of the highest-energy particle collisions in the world. That title now belongs to the Large Hadron Collider (LHC) near Geneva, Switzerland.

The lab began life in 1965 with the approval of a high energy physics proposal aimed at bringing together experts from universities across the country and the world. The project broke ground in 1968 for the first stage of the proton accelerator and was able to reach its design collision energy of 200 GeV by early 1972. By the end of 1972 it had doubled its energy to 400 GeV. From 1972 to 1985 the accelerator provided beam solely for fixed target experiments. During the early '80s the lab approved and implemented a plan to use the accelerator chain to collide protons and antiprotons. In the fall of 1985 the first proton-antiproton collisions were seen at a center of mass energy equal to 1.6 TeV. When collisions stopped in the fall of 2011 the center of mass energy was 1.96 TeV.

The D0 experiment is one of two experiments that detected collisions at Fermilab. The D0 Collaboration was founded in 1983, two years before Fermilab saw its first collisions. Construction of the 5,000 ton, three-story tall detector that was the centerpiece of the experiment was completed in early 1992. It took data until 1996 when it was given a major

---

[1] Located in Batavia, Illinois.

upgrade. After the upgrade was complete in 2001 it collected data until collisions were halted in the fall of 2011. The collaboration has 68 member institutions from 15 countries and, as of 2015, is still analyzing its data.

4.2 Accelerating Particles at Fermilab

Figure 4.1 shows a bird's-eye view of the Fermilab accelerator complex. During the colliding beams era the centerpiece of the Fermilab accelerator complex was the Tevatron, a superconducting proton-antiproton synchrotron. This machine was tasked with boosting the energy of each beam to their final energy of 980 GeV as well as initiating and maintaining collisions at two points around its ring. However, the Fermilab accelerator complex is home to a total of *ten* accelerators and storage rings. Particles start in one of two Preaccelerators (1 & 2) where they are accelerated to 750 keV. The first section of the linear accelerator (3), the Linac, further accelerates them to 116 MeV while the second section (4) accelerates them to

Figure 4.1: *Fermilab Campus*
Aerial view of the Fermilab accelerator complex. The large ring is the Tevatron.

400 MeV. After the Linac the particles are sent to the first synchrotron, the Booster (5), and given a boost up to 8 GeV. From there they move on to the second synchrotron, the Main Injector (6), and leave with an energy of 150 GeV. Antiprotons begin in the antiproton source and are shuffled to a set of storage rings called the Debuncher (7) and the Accumulator (8) which condense and accumulate them. They are then sent to the Recycler (9), a permanent magnet storage ring. Eventually, when enough antiprotons have been accumulated, they are accelerated in the Main Injector along with the protons to 150 GeV. The Tevatron (10) is the final step where the particles reach an energy of 980 GeV. More details on the Fermilab accelerator chain at the time it ceased to operate as a colliding beam facility can be found in Appendix A.

4.3 D0 Detector

The D0 detector was one of two general-purpose hadron collider detectors situated around the Fermilab Tevatron ring. Design began in 1983 during construction of its sister detector, the *Collider Detector at Fermilab* (CDF). This timing motivated a design that was complementary to CDF's strengths and weaknesses, namely one with an enhanced ability to detect leptons. Physics goals at the time, reachable at the expected center of mass energy of the Tevatron at 2 TeV, included precision measurements of the $W^\pm$ and Z bosons; exploration of new phenomena at and above their mass scales, including searches for the top quark; and investigation of high transverse momentum p_T particles. This required good, full solid angle coverage to obtain an accurate measurement of missing transverse energy indicating the presence of neutrinos. Measurement of high p_T particles required the development of a sophisticated hadronic calorimeter. All of these specifications were taken into account in the design of the D0 detector.

Construction of the detector was completed in early 1992. It operated during Run I of the Tevatron from 1992-1996. During Run I, the Tevatron operated at a center of mass energy of 1.8 TeV with six bunches each of protons and antiprotons with a bunch spacing of 3500 ns. It had a typical peak instantaneous luminosity of 1–2$\times 10^{31}$ cm^{-2}s^{-1}. D0 collected approximately 120 pb^{-1} of data and was able to meet most of its physics goals including the discovery of the top quark alongside CDF in 1995[27, 28]. From 1996-2001 the Fermilab accelerator complex received an upgrade that included the installation of the Main Injector and Recycler. During this time the D0 detector was also upgraded with a brand new tracking system and electronics to handle the new Tevatron operating conditions. Run II began in 2001 and ended on September 30, 2011 with the shutdown of the Tevatron. Typical peak luminosity near the end of Run II was 2–3$\times 10^{32}$ cm^{-2}s^{-1}. The Tevatron operated with three trains of twelve bunches each of protons and antiprotons with a bunch spacing of 396 ns. The total integrated luminosity delivered by the accelerator during Run II was 11.9 fb^{-1}. D0 was able to collect 10.9 fb^{-1} of data during this time. After data quality cuts the total integrated luminosity available for physics analyses was 9.7 fb^{-1}.

The original detector is described in detail in Ref. [29] with the upgraded detector of Run II described in Ref. [30]. An additional upgrade of the tracking system was installed in 2006 and is described in Ref. [31]. For the purposes of this Thesis the next sections describe the detector in the state it was in after the upgrade in 2006.

The D0 detector is a large machine weighing approximately 5500 tons with approximate dimensions $30' \times 30' \times 50'$. The detector is roughly cylindrically symmetric around the beam line and nearly covers the full solid angle. There are three main components to the D0 detector: the tracking system, the calorimeter, and the muon system. These components are arranged similar to the skin of an onion. From the inside moving radially out, a particle would pass through the beryllium beam pipe, the silicon tracking detector (SMT), the scintillating fiber tracker, a solenoid magnet, into the liquid argon (LAr)/depleted uranium electromagnetic (EM) and hadronic calorimeters, one layer of the muon system, an iron toroid magnet, and a second layer of the muon system. The EM and hadronic calorimeters are divided into three cryostats: two end cryostats (EC) and one central cryostat (CC). The central cryostat covers the region $|\eta| \lesssim 1$ and the end cryostat covers the $|\eta| \lesssim 4$ region. A cutaway view of the detector and its subsystems is shown in Fig. 4.2. The central region is illustrated in Fig. 4.3. In addition to these three main components are two other systems essential for recording and analyzing data: the triggering system and the luminosity detectors. Additional details on each component of the D0 detector are given in Appendix B.

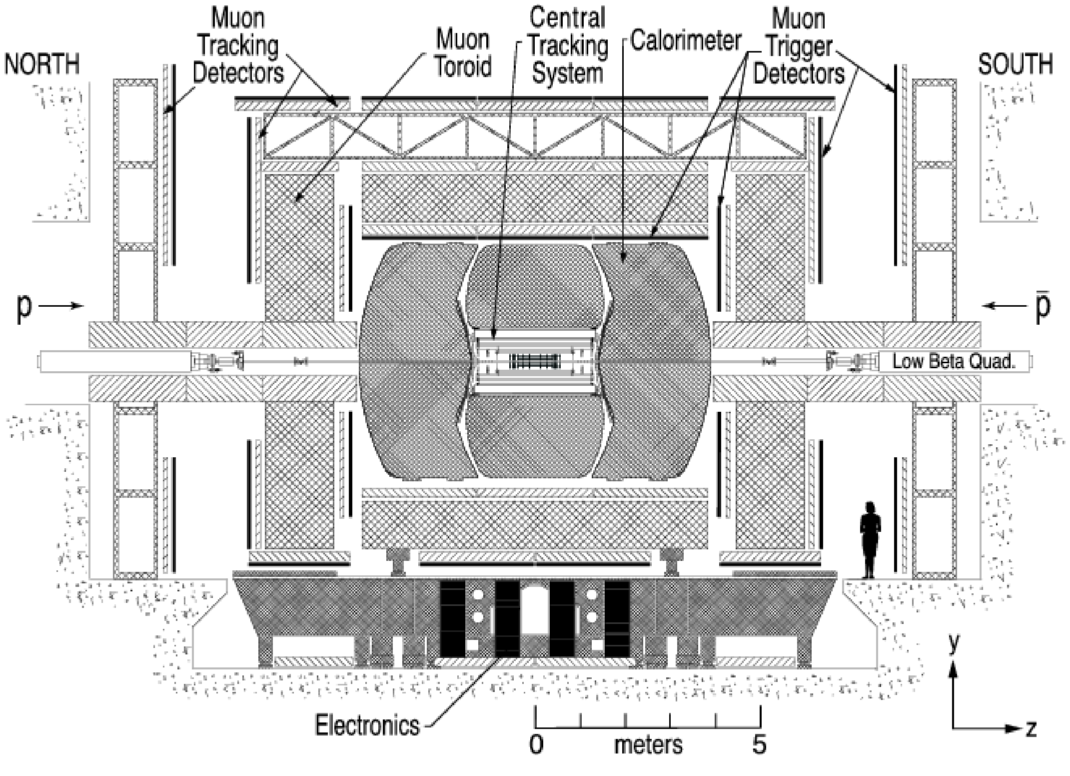

Figure 4.2: *D0 Detector*
Cutaway view of the D0 detector showing the onion skin layering of the detector subcomponents.

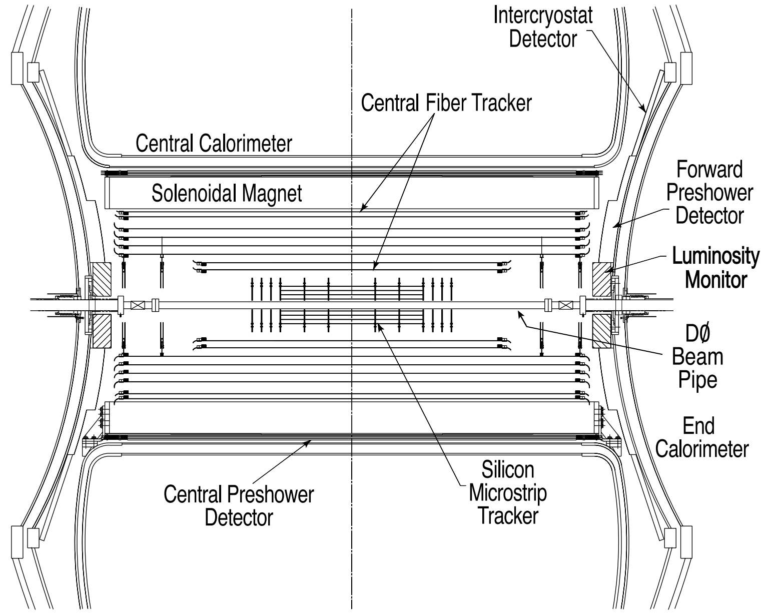

Figure 4.3: *Central D0 Detector*
Cutaway view of the center of the D0 detector.

4.4 Object Reconstruction

In order to study the collisions recorded by the D0 detector we must have an accurate measurement of the four-momentum of the particles produced. We must reconstruct physics objects from the signatures left in the detector. For the D0 detector there are three main types of signatures: *jets* which result from hadronic particle showers, charged leptons, and missing transverse energy $\not\!\!E_T$ which signifies the production of an undetectable neutrino in the final state.

4.4.1 Primary Vertex

Interactions in the D0 detector do not in general occur in the center of the detector and may be offset spatially. Since all other reconstructed objects are defined in reference to the interaction point or *primary vertex*, care must be taken to reconstruct it accurately. Tracks with a transverse momentum p_T of at least $0.5\,\mathrm{GeV}$ and at least two hits in the SMT are clustered in 2 cm intervals based on the z coordinates of their distance at closest approach from the beamline. These z clusters are then refined by removing outlying tracks with respect to the beamline. Selected tracks in a cluster are then fit to a common vertex. Several vertices may be found resulting from multiple $p\bar{p}$ interactions per beam crossing. Many are the result of soft $p\bar{p}$ interactions and some are the result of hard scatter interactions distinguished by their higher than average track p_T. The vertex that is most likely to have been the result of hard scattering is chosen as the primary vertex.

4.4.2 Jets

Quarks produced in the interaction will hadronize and produce a hadronic shower of particles which deposit most of their energy in the hadronic calorimeter. These energy depositions in the calorimeter are referred to as jets. By identifying the shower structure and measuring the energy deposited by the jet we can reconstruct position and energy measurements of the initial quark. In the following, jets are only reconstructed in the central calorimeter which corresponds to the region $|\eta| \leq 2.5$. While there are several good techniques for finding jets in the energy deposition in the calorimeter, we use a simple cone algorithm in this analysis. The Run II Midpoint Cone Algorithm is a clustering algorithm that assigns calorimeter towers to jets within a fixed cone of radius $\mathcal{R}_{cone} = \sqrt{(\Delta\eta)^2 + (\Delta\phi)^2} = 0.5$ in η-ϕ space. The Run II Midpoint Cone Algorithm can be described in four steps: tower reconstruction and pre-clustering, clustering into proto-jets, addition of midpoints, and merging and splitting. These four steps are described briefly below.

1. *Tower reconstruction and pre-clustering:* Pseudo-projective calorimeter towers of the same η and ϕ (see shaded regions of Fig. B.5) are reconstructed by assigning a (mass-

less) four-momentum vector to each calorimeter cell defined with respect to the primary vertex and then adding the four-momentum of all cells in a tower. Calorimeter towers with a $p_T \geq 1\,\mathrm{GeV}$ are used as seeds in the pre-clustering algorithm. Towers within $\Delta\mathcal{R} < 0.3$ of the seed tower are clustered together.

2. *Clustering:* A cone of radius $\mathcal{R}_{cone}$ placed around each pre-cluster centered at its centroid defines a proto-jet. Towers within the cone are added to the proto-jet and its center is adjusted according to the scheme:

$$\begin{aligned} p^{\mu} =& (E, \vec{p}) = \sum_i (E_i, \vec{p}_i) & \phi =& \tan^{-1}\left(\frac{p_y}{p_x}\right) \\ p_T =& \sqrt{p_x^2 + p_y^2} & y =& \frac{1}{2}\ln\left(\frac{E + p_z}{E - p_z}\right) \end{aligned} \tag{4.1}$$

   where the direction of the four-momentum defines a new cone. This procedure continues until the four-momentum of proto-jet coincides with the axis of the cone and is considered stable. Proto-jets with momentum less than $3\,\mathrm{GeV}$ are discarded.

3. *Addition of midpoints:* To reduce the algorithm's sensitivity to soft radiation we repeat the previous step using p_T-weighted midpoints between pairs of proto-jets as seeds.

4. *Merging and splitting:* To avoid double-counting the energy, overlapping proto-jets must be merged or split. In this analysis we merge the proto-jets if more than 50% of the p_T of the lower energy proto-jet is in the overlap region. Otherwise the cells in the overlap region are assigned to the nearest jet. The four-momenta of the jets are recomputed according to Eqs.4.1 and those with $p_T < 6\,\mathrm{GeV}$ are discarded.

To avoid the inclusion of "noisy" jets – jets that contain a large portion of fake calorimeter energy – in physics analyses we impose additional restrictions on the selected jets with the aim of ensuring reasonable energy deposits. We use an algorithm to remove calorimeter cells whose nearest neighbors are unlikely to be from a true jet. The fraction of a jet's energy deposited in the EM calorimeter must be between 5% and 95% and the energy fraction in the coarse hadronic calorimeter should be less than 40%.

4.4.2.1 Heavy-flavor Jets

Heavy quarks (specifically charm (c), bottom (b), and top (t)) are important as the decay products of heavy particles such as the W and Higgs bosons and are of interest when looking for physics beyond the standard model. With the exception of the top quark (which decays before it hadronizes), these quarks hadronize and are detected as jets. To a certain degree we are able to distinguish light-flavor from heavy-flavor jets and to a lesser degree between c and b quark jets by their lifetime. Hadrons with charm and bottom content have a relatively long lifetime compared to the top quark and can travel ≈ 3 mm before decaying. This distance is just short enough that the products are still in the tracking volume of the detector. Figure 4.4 depicts an event with a possible heavy-flavor jet. Some characteristics of heavy-flavor jets we might look for in the detector are a displaced vertex and tracks with large impact parameters denoted by d_0 in Fig. 4.4. D0 exploits these features using multivariate analysis (MVA) techniques to 'tag' jets as originating from b and c quarks. The output of the MVA is a continuum used to identify jets originating from the hadronization of b quarks. Using this output we can define requirements that correspond to characteristic "true" b quark jet tagging efficiencies and light-flavor jet rejection rates

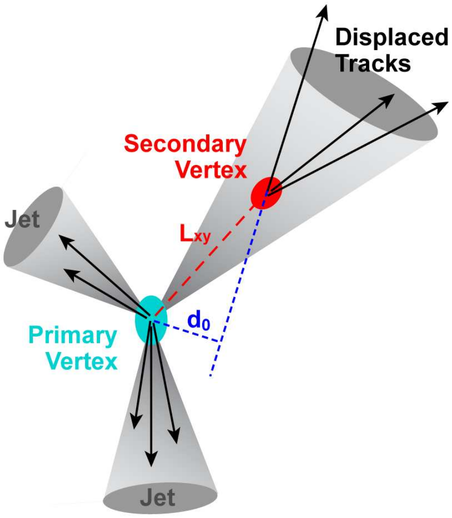

Figure 4.4: *Heavy-flavor Tagging*
Graphic representation of a heavy-flavor jet depicting the secondary vertex and impact parameter resulting from the decay of the heavy-flavor hadron.

4.4.3 Charged Leptons

Charged leptons in the D0 detector all have the ability to leave tracks. As described in Section 2.3.1, it is the way they interact in matter that determines their signature in the detector.

4.4.3.1 Electrons

Electrons leave tracks in the tracking detector and deposit the bulk of their energy in the electromagnetic sections of the calorimeter. Photons leave similar shower signatures in the detector and are included in the reconstruction of EM energy clusters. The reconstruction of the EM clusters proceeds in a similar manner as the hadronic jets. Electromagnetic clusters are reconstructed differently in the CC and EC calorimeters. Pseudo-projective towers in the calorimeter are formed and the transverse energy is summed in the four layers of the EM calorimeter and the first layer of the fine hadronic section of the calorimeter[2]. Towers with $E_T < 500$ MeV are discarded. In the CC, beginning with the tower with the highest E_T adjacent towers within a cone of radius 0.4 in η-ϕ space are added to form an EM cluster. In the EC, clusters are formed from adjacent towers within a transverse distance of 10 cm from the cell with the highest energy in the third layer of the EM calorimeter. Electrons are distinguished from photons by requiring a track with $p_T > 1.5\,\text{GeV}$ within a $\Delta\eta \times \Delta\phi = 0.05 \times 0.05$ window around the center of the cluster. For clusters in the CC (EC) we require that 97% (90%) of their energy be deposited in a cone of radius $\sqrt{(\Delta\eta)^2 + (\Delta\phi)^2} = 0.2$ in the EM calorimeter layers. In the CC region, a reconstructed isolated track must be associated with the EM cluster. Additional information such as the transverse and longitudinal shower shape, the EM energy fraction, number of hits in the various layers of the tracking detector, and cluster information from the preshower detectors is used to train a multivariate tool called a boosted decision tree (BDT) to identify electrons.

4.4.3.2 Muons

In contrast to electrons, muons do not produce showers in the EM calorimeter. However, they leave tracks in both the tracking detector and the muon system. Hits in both muon scintillator and wire chambers are used to form track segments in the muon system. These track segments are then matched to tracks in the central tracking detector to form muon candidates. Muon candidates are categorized based on the number of hits in the muon system, the quality of the track reconstruction in the central tracker, and isolation parameters in both the calorimeter and tracking system. The muon system has detectors both inside and outside the toroid and we require any muon candidates to have hits in both of of these

---

[2] The fine hadronic layer is included in the sum to account for leakage of EM showers into the hadronic section of the calorimeter.

regions, except where the detector support system limits coverage. To reduce the cosmic ray background we use scintillator hit timing information to ensure that hits coincide with a beam crossing.

4.4.3.3 Tau Leptons

Tau leptons are very short-lived and decay before they can leave a track. Because the tau lepton has a charge of 1, it decays most often to one or three charged particles and some number of neutral particles. Thirty-five percent of the time they decay leptonically to a muon or an electron and two neutrinos. The other 65% of the time they decay hadronically. This analysis does not attempt to reconstruct or reject tau leptons. The effect of their inclusion in the data and simulated samples on the analysis is negligible.

4.4.4 Missing Transverse Energy

As described in Section 2.2.2, colliding beams of particles with equal momentum results in a lab frame that is equivalent to the center of momentum frame and the initial momentum is zero. However, the hard scatter interaction occurs between the partons inside the proton and antiproton. The partons do not carry the full momentum of the proton but instead share it with the other constituents. This means that the total momentum of the interaction is not zero. Fortunately for us the partons carry very little *transverse* momentum and the total transverse momentum can be assumed to be zero.

This is essential to our reconstruction of neutrinos. Neutrinos only interact via the extremely short-range weak force and hence leave the detector without a trace. Their production in an event must be inferred. We look for an imbalance in the transverse energy of the event to identify neutrinos. This "missing" transverse energy or $\not{E}_T$ is calculated from the transverse energy. The transverse energy of individual calorimeter cells in the electromagnetic and fine hadronic calorimeter sections and clustered energy in the coarse hadronic section are added vectorially and the $\not{E}_T$ is taken to be a vector with the same magnitude with a direction of 180° with respect to the total sum. Any identified muons, which do not leave showers in the calorimeter, are subtracted from the total transverse energy.

Chapter 5

Models for the Higgs Boson with Exotic Spin and Parity

In Chapter 3 we discussed the possibility of looking for physics beyond the standard model by examining the spin (J) and parity (P) of the recently discovered Higgs boson. If it is truly the Higgs boson predicted by the SM then it should have $J^P = 0^+$. Two of the most highly-motivated BSM J^P states are $J^P = 0^-$ and $J^P = 2^+$. The pseudoscalar state $J^P = 0^-$ can result from two Higgs doublet models of type II[23] such as those found in supersymmetric models[24]. A boson with tensor couplings $J^P = 2^+$ can arise in models with extra dimensions such as generic models predicting a bulk Randall-Sundrum graviton[25, 26].

The experiments at the LHC have made measurements on the spin and parity of the Higgs boson in the $H \to WW$, $H \to \gamma\gamma$, and $H \to ZZ$ decay channels. The ability of the LHC experiments to distinguish between different J^P assignments is based primarily on the angular analysis of the Higgs boson decay products. The measurements have been consistent with the SM J^P assignment of $J^P = 0^+$ and they have been able to exclude some models with exotic spin and parity[32, 33].

The experiments at the Tevatron have found evidence of a particle decaying to two b quarks[18], which is consistent in mass and production rate with the Higgs boson discovered at the LHC[19, 20]. This is unique relative to the LHC measurements which rely on bosonic final states. Thus, we are in a unique position to study the spin and parity of this boson in its direct decay to fermions. This is well-motivated because if the Higgs sector is more complex we might expect multiple Higgs bosons which couple separately to fermions and bosons. It is therefore important to study the J^P character of the Higgs boson in its decays to both bosons and fermions. The VH associated production channels are among the most sensitive channels at the Tevatron and offer a method for studying the spin and parity of the Higgs boson in a (mostly) model-independent way. In this Thesis we will focus on the WH associated production channel but the general method of analysis is nearly identical to the ZH associated production channels. In Chapter 9 we will discuss the results of the combination of VH channels both at the D0 Collaboration and with the CDF Collaboration.

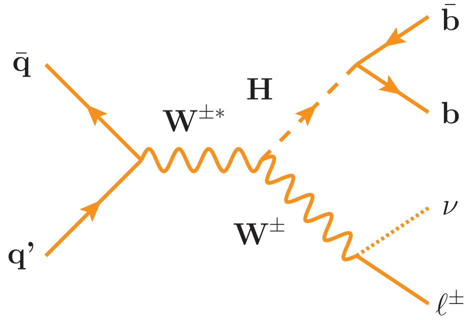

Figure 5.1: *WH Associated Production*
Example tree-level Feynman diagram of the WH associated production channel with the Higgs boson decaying to a pair of b quarks and the W boson decaying leptonically.

5.1 Threshold Production

An example tree-level Feynman diagram of this process is shown in Fig. 5.1. By studying the kinematics of this final state we can distinguish different J^P states. At a hadron collider the hard-scatter interaction occurs between the constituent partons of the (anti)proton.

Since the partons carry only a fraction of the total momentum of the proton the amount of energy available for the production of final state particles is significantly reduced relative to the total center-of-mass energy of the colliding hadrons. If the interacting partons carry momentum fractions x_1 and x_2 then the center-of-mass energy of the partons $\sqrt{\hat{s}}$ is related to the center-of-mass energy of the colliding beams $\sqrt{s}$ by $\hat{s} = x_1 x_2 s$. The momentum fractions of the interacting partons are described by probability densities called parton distribution functions (PDFs). The PDFs describe the relationship between the momentum fraction x and the momentum exchange Q^2 of the interaction and are derived from experiment. The proton parton distribution functions are plotted as a function of x for two values of Q^2 in Fig. 5.2. To estimate the momentum fractions needed to produce a final state with mass M we use the rule of thumb $\sqrt{\hat{s}} \sim M \sim Q$. Figure 5.3 depicts the parton kinematics at the Tevatron as a function of the momentum exchange.

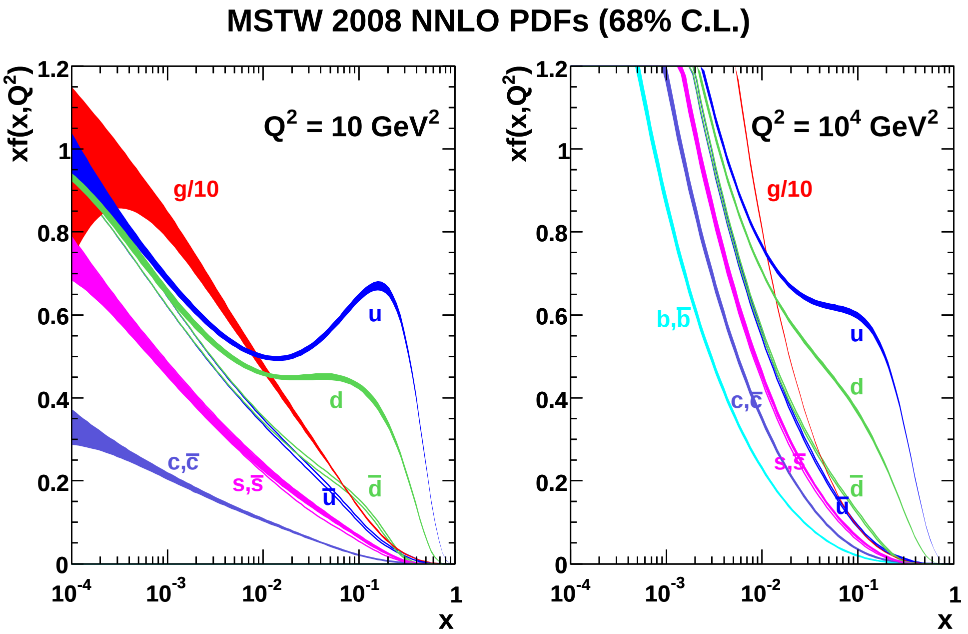

Figure 5.2: *Proton Parton Distribution Functions*
Proton parton distribution functions from the MSTW2008 next-to-next-leading-order calculation for two different values of the momentum exchange[34].

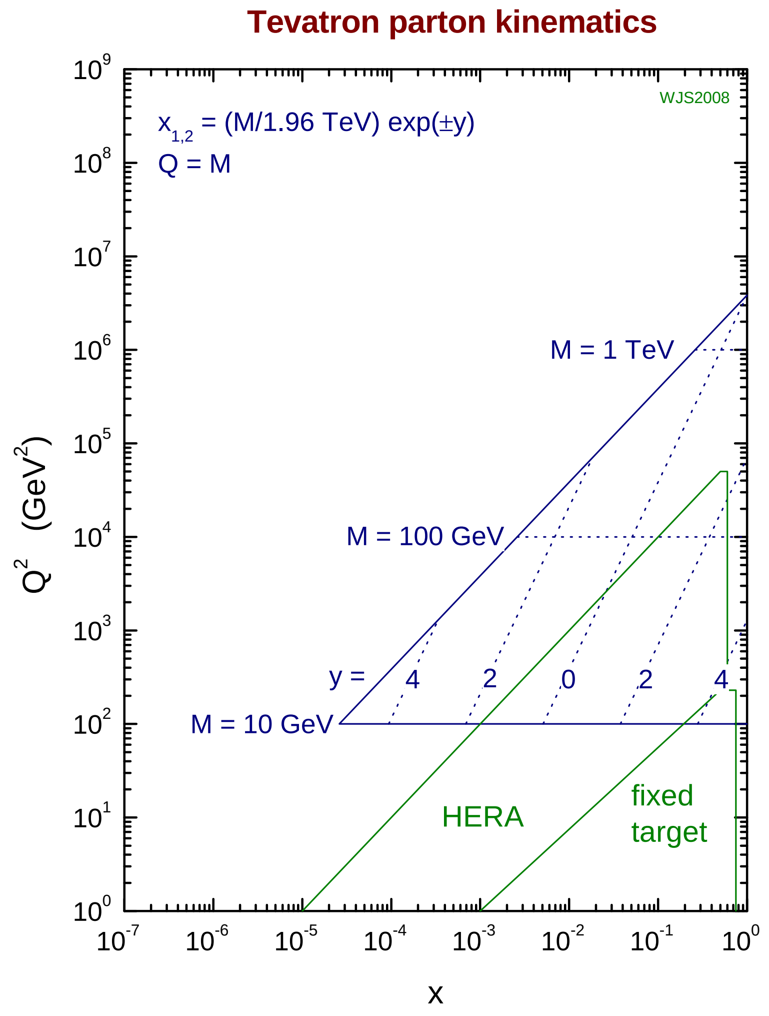

Figure 5.3: *Tevatron Parton Kinematics*
Tevatron parton kinematics as a function of the momentum exchange[35].

Producing the WH final state requires an energy of at least $125 + 80 = 205\,\mathrm{GeV}$. The necessary momentum fraction for $M^2 \approx 4 \times 10^4 \sim Q^2$ can be read from Fig. 5.3. Assuming a rapidity of zero this corresponds to a momentum fraction of approximately $x = 0.1$. At a momentum fraction $x = 0.1$ the parton-parton luminosity is near a local maximum and the WH system is almost always produced near threshold. We can define how far the WH system is from threshold as $\beta = 2p/\sqrt{s}$ where p is the WH three-momentum in the center-of-mass frame of the colliding beams in units of the center-of-mass energy.

5.2 Helicity Amplitudes

The method of determining the Higgs boson spin and parity assignments used in this analysis was first described in the context of electron-positron collisions[36], but its application to hadron collisions is straightforward. The form of the production cross section and angular distributions at threshold depend on the J^P character of the Higgs boson. Because we are only interested in the *behavior* of these observables at threshold it is not necessary to know the exact form of the couplings. This allows us to distinguish different J^P assignments in a model-independent way. In the following we will work in the helicity formalism (see for example Ref. [37]) which is well-suited for analyzing states with definite spin and parity.

Helicity is defined as the dot product of the spin of the particle with the unit vector in the direction of its momentum $h = \vec{S} \cdot \hat{p}$[1]. A massive particle with spin $S = J$ has $2J + 1$ helicity states with values $\lambda = -J, -J + 1, \ldots, J$. Massless particles on the other hand have only two helicity states $\lambda = \pm J$ due to the fact that there are no components of spin

---

[1] Here I use S to refer to the spin of the particle to be precise; helicity depends on the spin of the particle $\vec{S}$ not the total angular momentum $\vec{J} = \vec{L} + \vec{S}$ which is defined to be perpendicular to the motion. In collision physics we define our axes such that the orbital angular momentum $\vec{L}$ is zero and $\vec{J} = \vec{S}$.

transverse to the direction of motion[2]. The helicity amplitude $\mathcal{A}$ of the $W^* \to WH$ process with the azimuthal angle set to zero takes the form $\mathcal{A} \propto d^1_{M,\lambda}(\theta) A_{\lambda_W \lambda_H}$ where $d^1_{M,\lambda}(\theta)$ are the Wigner small d matrices which relate a rotated state to an original unrotated state and $\lambda = \lambda_W - \lambda_H$ are helicities. The $A_{\lambda_W \lambda_H}$ are reduced amplitudes which only depend on the helicities of the W and H bosons. The reduced helicity amplitudes are related to states with negative helicity by $A_{\lambda_W \lambda_H} = n_H A_{-\lambda_W - \lambda_H}$. The normality of the Higgs boson n_H is defined by $n_H = (-1)^J P$. The angular differential cross section is proportional to the square of the helicity amplitudes summed over the final state helicities λ_H and λ_W. Performing the summation we obtain:

$$\begin{aligned} \frac{1}{\sigma}\frac{d\sigma}{d\cos\theta} &= \frac{3}{4A^2}\sin^2\theta\big[|A_{00}|^2 + 2|A_{11}|^2\big] + (1+\cos^2\theta)\big[|A_{01}|^2 + |A_{10}|^2 + |A_{12}|^2\big] \\ A^2 &= |A_{00}|^2 + 2|A_{11}|^2 + 2|A_{01}|^2 + 2|A_{10}|^2 + 2|A_{12}|^2. \end{aligned} \tag{5.1}$$

Equation 5.1 is the general form for a Higgs boson spin $J \leq 2$ and not all terms are nonzero for a specific J. To study the threshold dependence, we can parametrize the reduced amplitudes as a function of β. As an example we can examine the SM case: $J^P = 0^+$. The spin of the SM Higgs boson restricts the reduced helicity amplitudes to those of the form $A_{\lambda_W 0}$. The W boson has $J^P = 1^-$ with helicity values $\lambda_W = 0, \pm 1$. Only two terms in Eq. 5.1 remain: A_{00} and A_{10}. Substituting the standard model values $A_{00} = -E_W/m_W$ and $A_{10} = -1$ and rearranging Eq. 5.1 yields

$$\frac{1}{\sigma}\frac{d\sigma}{d\cos\theta} = \frac{3}{4}\frac{\beta^2\sin^2\theta + 8m_W^2/s}{\beta^2 + 12m_W^2/s}. \tag{5.2}$$

At threshold $\beta \to 0$ and WH production is isotropic. To leading order, the total cross

---

[2] Because massless particles travel at the speed of light it is impossible to boost into the rest frame of the particle; it has no rest frame. You can only measure the spin along its momentum.

section near threshold goes as one power of β from the phase space integration. At high boosts (large β) it has a characteristic $\sin^2\theta$ dependence. Near threshold, where the cross section $\sim \beta$, the production mechanism is thus referred to as *s*-wave production.

To further investigate the implications of Eq. 5.1 we can examine a state with negative normality: $J^P = 0^-$. The equation relating reduced helicity amplitudes with positive and negative helicities forbids the A_{00} term for states with negative normality. Everything else remains the same and this leaves only the A_{10} term. For a spin and parity assignment of $J^P = 0^-$, the A_{10} term is of the form $-i\beta s a_1$ where a_1 is a coefficient that does not depend on the momenta near threshold. At threshold the production is isotropic and develops a $\cos^2\theta$ dependence at higher β. The cross section rises as $\sim \beta^3$ and the production mechanism is *d*-wave. Other spin and parity assignments can be examined in the same manner. In general, the cross section rises as the square of the leading order β dependence of the reduced amplitudes plus one factor of β from the phase space integration.

5.3 Invariant Mass as a Discrimination Tool

The form of the angular distribution above threshold and the β-dependence of the cross section near threshold affect the final state kinematics in observable ways. The angular distribution can be examined by measuring the angular correlations between the decay products in the final state. At the LHC this is the primary method of measuring the spin and parity of the Higgs boson. Compared to the LHC, the Tevatron has a much smaller integrated luminosity and the behavior of the cross section near threshold is more important. The β-dependence of the cross section affects the final state kinematics by enhancing or suppressing the contributions of parton-parton interactions with a particular momentum fraction. As an example, consider the case of $J^P = 0^-$ pseudoscalar versus the SM Higgs boson, $J^P = 0^+$. Just above threshold the $J^P = 0^-$ cross section is heavily suppressed by the β^3 dependence compared to the β dependence of the standard model. This pushes production of the WH system to higher energies and, thus, to higher momentum fractions.

This effect is observable in the invariant mass distribution of the final state. The square of the invariant mass is defined as the Minkowski inner product of the four-momentum $P^\mu P_\mu$. As an invariant it is the same in all reference frames. In the rest frame of the W^* boson the invariant mass is simply the mass of the W^* boson M. Referring back to Section 5.1 we saw that $M^2 \sim x_1 x_2 s$ and threshold production of the WH system requires the momentum fractions to be ~ 0.1. Larger average momentum fractions will increase the mass of the W^* boson and the invariant mass of the system. For WH production the invariant mass as defined in the lab frame is:

$$m = \sqrt{(E_W + E_H)^2 - (\vec{p}_W + \vec{p}_H)^2}. \tag{5.3}$$

As a proof of concept, the authors of Ref. [38] produced Monte Carlo event samples for $ZX \to \ell\ell b\bar{b}$, $WX \to \ell\nu b\bar{b}$, and $VX \to \nu\nu b\bar{b}$ production with spin and parity assignments of $J^P = 0^+$, 0^-, and 2^+ and applied the same cuts as the D0 and CDF published analyses of the same production channels. Figure 5.4 shows the invariant mass of the $ZX \to \ell\ell b\bar{b}$ final state using D0 cuts. As expected, the $J^P = 0^-$ state has on average a higher invariant mass. The effect is stronger for the $J^P = 2^+$ state because the cross section rises $\sim \beta^5$ above threshold, thus forcing x values higher.

Because the lifetimes of the W and H bosons are so short we must instead make measurements on their decay products. When considering leptonic decays of the W or Z boson

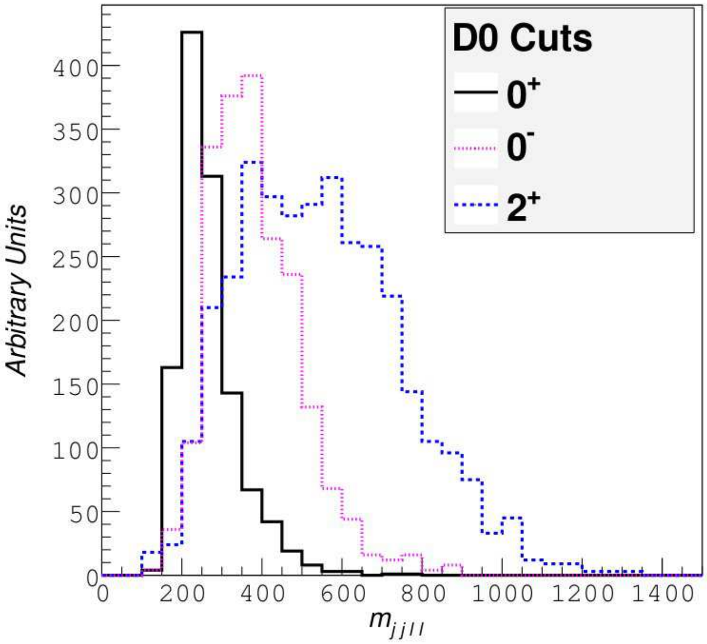

Figure 5.4: *Simple Model of the Invariant Mass of the* $ZX \to \ell\ell b\bar{b}$ *System*
Plot of the invariant mass of the $ZX \to \ell\ell b\bar{b}$ system from the simple model in Ref. [38] using the selection requirements from the published D0 $ZH \to \ell\ell b\bar{b}$ analysis[39].

with one or more neutrinos the invariant mass of the final state cannot be measured. We can only infer the presence of neutrinos by the approximate conservation of momentum in the transverse direction; their momenta in the z direction is not measured. We instead define a quantity that is invariant to boosts in the z direction and behaves in the same manner as the invariant mass: the transverse mass m_T. For the $WX \rightarrow \ell\nu b\bar{b}$ production channel the transverse mass is

$$\begin{aligned} m_T^2 &= (E_T^W + E_T^X)^2 - (\vec{p}_T^W + \vec{p}_T^X)^2, \\ p_T^W &= \not{E}_T + p_T^\ell. \end{aligned} \tag{5.4}$$

Figure 5.5 is the transverse mass distribution for the $WX \rightarrow \ell\nu b\bar{b}$ channel using the selection cuts from the CDF experiment's published $WH \rightarrow \ell\nu b\bar{b}$ analysis[40], again from Ref. [38].

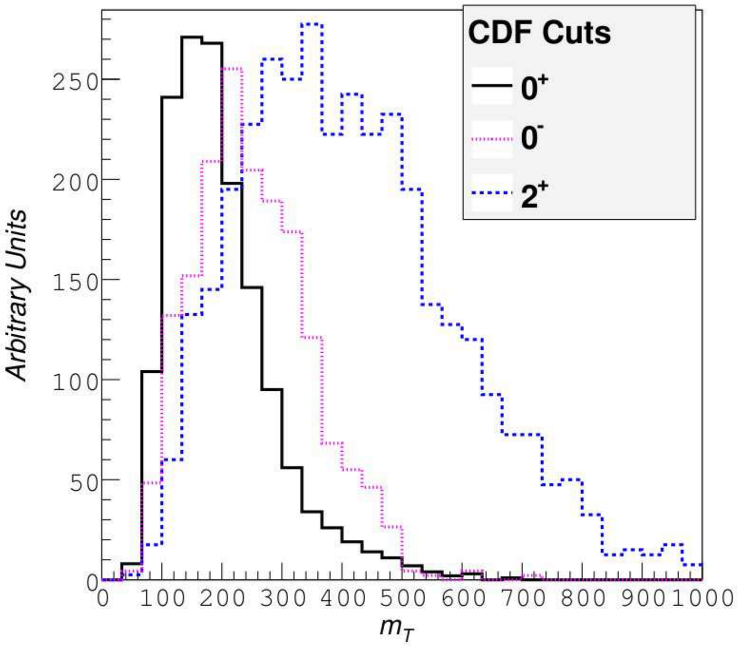

Figure 5.5: *Simple Model of the Transverse Mass of the* $WX \rightarrow \ell\nu b\bar{b}$ *System*
Plot of the transverse mass of the $WX \rightarrow \ell\nu b\bar{b}$ system from the simple model in Ref. [38] using the selection requirements from the published CDF $WH \rightarrow \ell\nu b\bar{b}$ analysis.

The difference in the average value of the transverse mass of the WX system between the J^P assignments is the key to determining if the excess of Higgs-like events observed at the Tevatron is indeed a Higgs boson and if it has similar spin and parity quantum numbers as the boson discovered at the LHC. This makes the analysis method relatively simple: 1) generate Monte Carlo samples for $WX \to \ell\nu b\bar{b}$ production with $J^P = 0^-$ and $J^P = 2^+$, 2) reanalyze the data using the published analysis method, this time including the new samples, and 3) use the transverse mass of the WX system to discriminate between J^P assignments. The rest of this Thesis will describe this analysis method in detail. Chapter 6 describes the data and the simulated event samples. The analysis method including the selection criteria is described in Chapter 7. The statistical method used to analyze the transverse mass distribution is discussed in Chapter 8. Finally, the results and conclusions are given in Chapters 9 and 10.

Chapter 6

Data & Simulation

The data studied in this analysis were collected over a period of ten years using the D0 detector. The data were taken starting after the commissioning of the Main Injector and the upgrade of the D0 detector, and is referred to as Run II. Run II is divided into two major subsets, Run IIa and Run IIb, by the addition of a new layer to the silicon detector. Run IIb is further divided into four epochs; Run IIb1, Run IIb2, Run IIb3, and Run IIb4; each representing roughly a year of running. Each of the five epochs (including Run IIa) are treated separately to account for differences between epochs such as instantaneous luminosity profiles, tracking detector efficiency, and detector changes. We produce simulated event samples via Monte Carlo (MC) for each epoch to properly model the detector response.

With the exception of the multijet sample, we used Monte Carlo to simulate nearly all SM processes which could result in our final state signature. All simulations use the CTEQ6L1[41] leading-order parton distribution function (PDF) set in the event generation. Parton showering and hadronization is done with PYTHIA[42] for all MC samples. Events are processed through a full detector simulation using GEANT[43]. To simulate the operating conditions of the detector such as residual signals from the previous beam crossing (referred to as pile-up), noise in the detector, and additional $p\bar{p}$ interactions (or underlying events) we overlay events from randomly selected beam crossings with the same luminosity. Finally, the simulated events are put through the same reconstruction process as data.

6.1 Data

6.1.1 Luminosity

Over the course of Run II, the accelerator division was able to deliver 11.9 fb^{-1} of integrated luminosity to the D0 experiment. Figure 6.1 shows the delivered and recorded integrated luminosity over the course of Run II. The D0 detector was able to record 10.7 fb^{-1} of data during this period. Detector latency and deadtime as well as unexpected malfunctions reduce the data collection efficiency to below 100%. Once data are recorded we enforce requirements on the quality; if any part of the detector was functioning in a manner that compromised its ability to identify physics objects the recorded data during that time is cut. After data quality cuts the total integrated luminosity used in this analysis is 9.74 fb^{-1}. Table 6.1 shows the integrated luminosity distribution across all epochs. The uncertainty on the luminosity measurement is 6.1%.

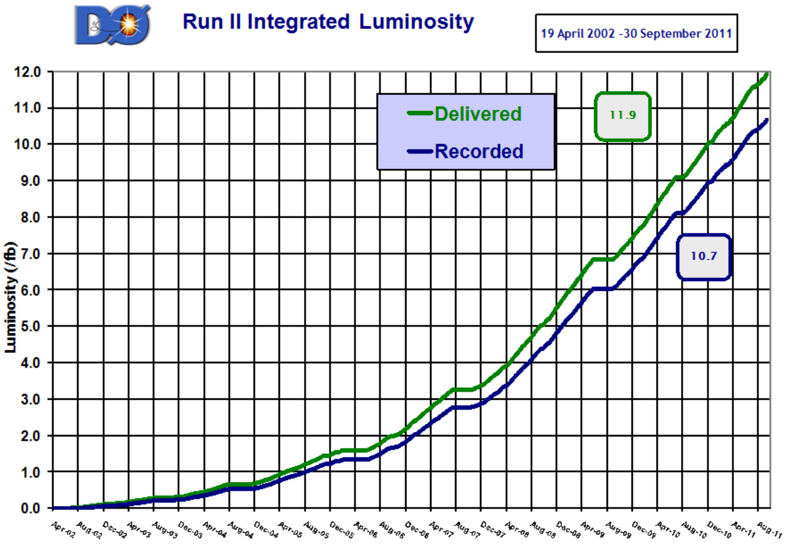

Figure 6.1: *Recorded Luminosity*
Shown above is a graph of the integrated luminosity over the whole of Run II. A total integrated luminosity of 11.9 fb^{-1} was delivered by the accelerator division. D0 was able to record 10.7 fb^{-1}.

	Epoch	Integrated Luminosity (fb^{-1})
Run IIa	Run IIa	1.08
Run IIb	Run IIb1	1.22
	Run IIb2	3.04
	Run IIb3	1.99
	Run IIb4	2.40

Table 6.1: *Integrated Luminosity*
Total integrated luminosity after data quality requirements for each epoch.

6.1.2 Triggers

The data sample for this analysis was obtained through the use of specific triggers defined by D0 to capture events with the signature of high-p_T electroweak interactions. Of particular importance to this analysis are triggers based on single, charged leptons.

For the electron channel we use the logical OR of the single EM and EM+jets trigger suites. Both trigger suites require a good EM trigger object to be above pre-defined thresholds and the EM+jets trigger requires at least one high-p_T jet. Minimum electron and jet p_T thresholds are different for each trigger. The efficiency of these triggers is approximately (90-100)% for the events passing the event selection outlined in Section 7.1 depending on the individual trigger and the location of the electron candidate in the detector volume. We model the trigger response in Monte Carlo by applying a weight to events. The weight is calculated by measuring the trigger efficiency as a function of electron ϕ, η, and p_T.

In the muon channel the equivalent trigger suites – single muon and muon+jets – have an efficiency of approximately 70% for our selected events. To increase the acceptance in the muon channel we do not require any specific trigger and instead use the logical OR of all available D0 triggers with the exception of those aimed at identifying heavy-quark jets. The full complement of triggers which contribute to this *inclusive* event sample is large and varied, making it difficult to model in the Monte Carlo. We therefore take a two-step approach to modeling the muon trigger response. First, we verify good data and simulation agreement for events selected by the well-modeled single muon and muon+jets trigger suites, collectively $T_{\mu OR}$. We then compare the data events selected by the inclusive trigger T_{incl} to the data events selected by $T_{\mu OR}$ and define a trigger correction for MC intended to account for the additional contribution from T_{incl}:

$$P_{corr} = \frac{(N_{Data} - N_{MJ})_{incl} - (N_{Data} - N_{MJ})_{\mu OR}}{N_{MC}}. \tag{6.1}$$

Here N_{MC} is the total number of MC events with trigger efficiency set to 1, N_{Data} is the number of data events, and N_{MJ} is the number of multijet events. Multijet events, as detailed in Section 6.4, are estimated from data and do not have this correction applied; their influence on P_{corr} is removed by subtracting them from the data events. The final trigger efficiency applied to each MC event is the sum of P_{corr} and the efficiency of $T_{\mu OR}$ with the constraint that the total efficiency must be less than unity. The most significant contributions to T_{incl} beyond $T_{\mu OR}$ triggers are based on jets and $\not\!\!E_T$. To account for this, the trigger correction P_{corr} is parametrized as a function of the scalar sum of the p_T of all jets and the $\not\!\!E_T$. To account for the changing trigger composition as a function of detector η and the partial muon coverage due to support structures we derive separate corrections for regions in muon η and ϕ.

6.2 Simulated Signal Samples

To test the compatibility of models for a Higgs boson with non-SM J^P assignments with data we study the $WH \rightarrow \ell\nu b\bar{b}$ process. We include the $ZH \rightarrow \ell\ell b\bar{b}$ process in our signal samples to account for scenarios where only one of the leptons is identified and the other contributes to the $\not\!\!E_T$. All samples have been generated for a Higgs mass m_H of 125 GeV. The SM Higgs boson signal processes, which have $J^P = 0^+$, are generated using PYTHIA. Both non-SM Higgs boson signals, the pseudoscalar $J^P = 0^-$ and the graviton-like $J^P = 2^+$ signals, are generated using MADGRAPH[44]. We use a Randall-Sundrum (RS) extra-dimensional model[25, 26] which has a $J^P = 2^+$ particle with graviton-like couplings to simulate a non-SM $J^P = 2^+$ Higgs boson. A generic model of this type has been implemented in MADGRAPH[45, 46]. To generate events using this model we assign the $J^P = 2^+$ particle a mass of 125 GeV and specify the production mechanism and final state. In addition to the models available in MADGRAPH, it is possible to implement user-defined models. The model used for the generation of events with a non-SM $J^P = 0^-$ Higgs boson was written by the authors of Reference [38]. We have verified that the SM Higgs boson sample generated with PYTHIA agrees with a SM Higgs boson sample produced with MADGRAPH.

All signal samples are normalized to the cross section times decay branching ratio as predicted by the standard model. The signal cross sections are calculated at next-to-next-to-leading order (NNLO) using the MSTW2008 NNLO PDF set[34]. We use HDECAY[47] to obtain the decay branching fraction for the Higgs boson. Table 6.2 lists all the signal processes, the spin and parity values, the event generator, and the cross section times branching ratio $\sigma \times BR$.

Process	J^P	Generator	$\sigma \times BR$ [pb]
$WH \to \ell\nu b\bar{b}$	0^+	PYTHIA	0.02425
$ZH \to \ell\ell b\bar{b}$	0^+	PYTHIA	0.00458
$WX \to \ell\nu b\bar{b}$	0^-	MADGRAPH	0.02425^*
$ZX \to \ell\ell b\bar{b}$	0^-	MADGRAPH	0.00458^*
$WX \to \ell\nu b\bar{b}$	2^+	MADGRAPH	0.02425^*
$ZX \to \ell\ell b\bar{b}$	2^+	MADGRAPH	0.00458^*

Table 6.2: *Signal Cross Section Times Branching Ratio*
Signal cross sections times branching ratio. Items marked with * do not have a theoretically defined cross section so they are normalized to the SM process.

6.3 Simulated Background Samples

We consider SM processes which are able to reproduce the final state products as backgrounds. These include multijet events, vector boson plus jets events (V+jets), diboson production VV, single top quark production, and top quark pair $t\bar{t}$ production. These backgrounds, with the exception of multijet, are all simulated by D0 and have standard corrections applied. The type of correction depends on the background sample.

6.3.1 V+jets Samples

Our V+jets samples are generated with ALPGEN[48]. We produce separate samples for W and Z bosons. Both bosons decay leptonically with the Z boson decaying to two leptons ($\to \ell\ell$) and the W boson decaying to a lepton and a neutrino ($\to \ell\nu$). We produce vector bosons and light-flavor (lf) jets separately from vector bosons and heavy-flavor (hf) jets. The W+lf sample consists of events with one W boson and between 1–5 light-flavor jets. Heavy-flavor jets are defined as having b or c quark content and the W+hf sample consists of one W boson, two b (c) jets, and 1–3 light-flavor jets. The Z+lf and Z+hf samples are generated in a similar manner with one Z boson and 1–3 light-flavor jets or two b (c) jets and 1–2 light-flavor jets, respectively. The Z+jets samples are produced in four regions depending on the mass of the Z boson to increase statistics.

We reweight our V+jets samples to account for known issues (see for example Ref. [49]) in ALPGEN leading to incorrect modeling of certain kinematic distributions. The reweightings are designed to correct the *shape* of the distribution without affecting the overall normalization. To minimize contamination from signal we derive the correction before events are b-tagged. Corrections are derived in event samples selected with the muon+jets triggers by a direct comparison between V+jets MC and data with all non-V+jets backgrounds subtracted and are applied to both electrons and muons. We correct the η distribution of the two highest p_T jets for both W+jets and Z+jets events. The lepton η distribution in W+jets events is also corrected. Discrepancies in the transverse momentum of the W boson p_T^W and the jet separation in η-ϕ space $\Delta\mathcal{R}(j_1, j_2)$ are correlated and a two-dimensional correction is derived. The p_T^W reweighting is only applied to W+jets events while the $\Delta\mathcal{R}(j_1, j_2)$ reweighting is applied to all V+jets events. The V+jets sample and the multijet sample are normalized to data after the event selection. A simultaneous fit of the V+jets and multijet samples to data with all other SM backgrounds subtracted is performed in the m_T^W distribution. Tables 6.3 and 6.4 summarize the events generated for the V+jets sample.

6.3.2 Diboson VV Samples

Diboson processes include WW, ZZ, or WZ production where one weak vector boson decays leptonically and one decays hadronically. All diboson processes are generated with PYTHIA. Table 6.5 summarizes the cross section times branching ratio for the diboson processes.

	Process	$\sigma \times BR$ [pb]
$W + jj$	+0 light parton	5875.679
	+1 light parton	1656.399
	+2 light partons	388.983
	+3 light partons	91.519
	+4 light partons	20.920
	+5 light partons	6.599
$W + bb$	+0 light parton	17.828
	+1 light parton	8.127
	+2 light partons	2.971
	+3 light partons	1.392
$W + cc$	+0 light parton	45.684
	+1 light parton	25.639
	+2 light partons	10.463
	+3 light partons	5.08

Table 6.3: *W+Jets Event Sample*
Cross section times branching ratio for W+jets events. All processes are generated using ALPGEN.

6.3.3 Single Top Quark Samples

The electroweak production of a single top quark occurs at the Tevatron in two main channels: *s-channel* and *t-channel*. The two production channels are illustrated in Fig. 6.2. We consider top quarks decaying into a W boson and a b quark where the W boson decays leptonically. We produce both s-channel and t-channel samples separately for each lepton flavor using SINGLETOP[50]. Their cross sections multiplied by branching ratio are outlined in Table 6.5.

6.3.4 Top Quark Pair $t\bar{t}$ Samples

Top quark pair production is illustrated in Fig. 6.3. We consider the decay chain $t \rightarrow Wb$ where the W bosons either both decay leptonically or one decays hadronically and the other

Process	Mass Range [GeV]	$\sigma \times BR$ [pb]
Z+lf Production		
$Z(\to \ell\ell)$+lf	15–75	1488.0800
	75–130	710.7280
	130–250	5.3353
	250–1960	0.4380
Z+hf Production		
$Z(\to \ell\ell) + b\bar{b}$+lf	15–75	4.5482
	75–130	4.0986
	130–250	0.0353
	250–1960	0.0034
$Z(\to \ell\ell) + c\bar{c}$+lf	15–75	34.8360
	75–130	10.9150
	130–250	0.0965
	250–1960	0.0085

Table 6.4: *Z+Jets Event Sample*
Cross section times branching ratio for Z+jets events. For all processes $\ell = e$, μ, τ. The Z+lf processes are produced with an additional 0, 1, 2, or 3 light partons. The Z+hf processes are produced with an additional 0, 1, or 2 light partons. All processes are generated using ALPGEN.

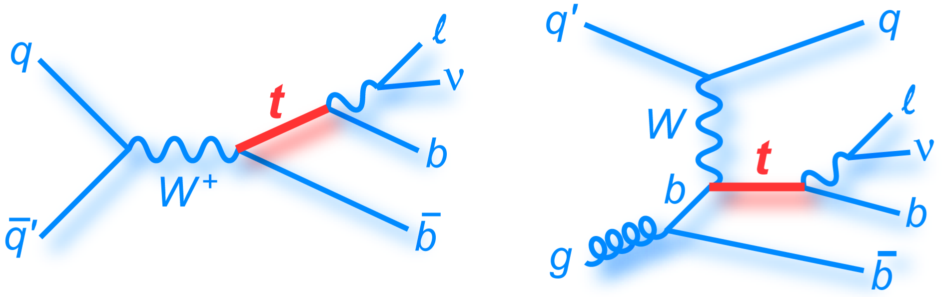

Figure 6.2: *Single Top Quark Production Diagrams*
Representative Feynman diagrams for single top quark production in the s-channel and t-channel.

decays leptonically for all $t\bar{t}$ samples. The contribution from events where both W bosons decay hadronically is negligible in this analysis. Samples are produced with an additional 0, 1, or 2 light quark jet(s) to account for possible additional jets in the final state from higher-order diagrams and multiple collisions. We use ALPGEN to generate events inclusively for all lepton flavors. Table 6.5 outlines the generated processes.

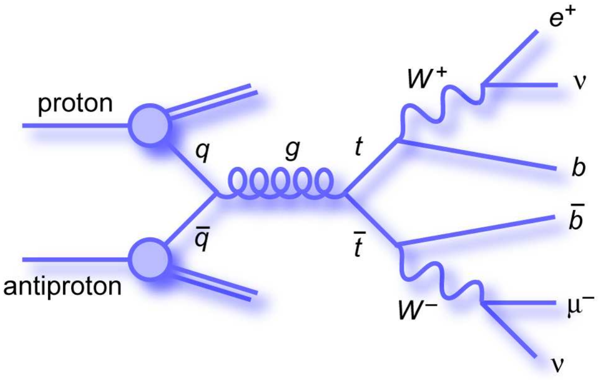

Figure 6.3: *Top Quark Pair Production Diagram*
Representative Feynman diagram for top quark pair production.

6.4 Multijet Sample Derivation

Rather than being simulated with Monte Carlo, the multijet sample is derived using data. A template sample is created by reweighting individual data events and is then scaled after the event selection to estimate the number of multijet events that pass our selection. To do this we make use of the "loose" and "tight" lepton identification criteria described in Section 7.1. Events that pass the *tight* lepton identification criterion are considered in the analysis while those events only passing the *loose* criterion are not. The number of events in data with a lepton that passes the *loose* criterion N_L will be

$$N_L = N_\ell + N_{MJ} \tag{6.2}$$

where N_ℓ is the number of events with a real lepton in the *loose* sample and N_{MJ} is the number of misidentified multijet events in the *loose* sample. To obtain the number of events

Process		Generator	$\sigma \times BR$ [pb]
WW inclusive		PYTHIA	11.34
ZZ inclusive		PYTHIA	1.20
WZ inclusive		PYTHIA	3.22
Single top quark s-channel ($tb \rightarrow e\nu b\bar{b}$)		SINGLETOP	0.1050
Single top quark s-channel ($tb \rightarrow \mu\nu b\bar{b}$)		SINGLETOP	0.1180
Single top quark s-channel ($tb \rightarrow \tau\nu b\bar{b}$)		SINGLETOP	0.1260
Single top quark t-channel ($tqb \rightarrow e\nu bq\bar{b}$)		SINGLETOP	0.2520
Single top quark t-channel ($tqb \rightarrow \mu\nu bq\bar{b}$)		SINGLETOP	0.2470
Single top quark t-channel ($tqb \rightarrow \tau\nu bq\bar{b}$)		SINGLETOP	0.2630
$t\bar{t} \rightarrow b\bar{b} + \ell^+\nu\ell^-\bar{\nu}$	+0 light parton	ALPGEN	0.4900
	+1 light parton	ALPGEN	0.1980
	+2 light partons	ALPGEN	0.0941
$t\bar{t} \rightarrow b\bar{b} + \ell\nu + 2j$	+0 light parton	ALPGEN	2.0340
	+1 light parton	ALPGEN	0.8270
	+2 light partons	ALPGEN	0.4050

Table 6.5: *Diboson and Top Quark Backgrounds*
Cross sections times branching ratio and number of events for diboson and top quark backgrounds.

in data with a lepton that passes the *tight* requirement N_T we define two efficiencies: *i*) the efficiency for a real lepton that passes the *loose* requirement to also pass the *tight* requirement ϵ_ℓ and *ii*) the efficiency for a jet misidentified as a lepton that passed the *loose* requirement to subsequently pass the *tight* requirement f_j. N_T is then defined as

$$N_T = \epsilon_\ell N_\ell + f_j N_{MJ}. \tag{6.3}$$

Because our goal is to reweight actual data events to create a background sample we must be careful to keep our samples orthogonal to avoid correlated fluctuations in our results. We do this by creating the template sample such that it only contains those events which pass the *loose* requirement but fail the *tight* requirement. The template sample then does not contain any events which are also considered in the analysis. Equations 6.2 and 6.3 can be combined to find the number of misidentified multijet events in the *tight* sample N_{MJ}^{T} as a function of the number of *loose-not-tight* events N_{L-T}:

$$N_{MJ}^{T} = \frac{f_j}{1-f_j} N_{L-T} - \frac{f_j(1-\epsilon_\ell)}{(1-f_j)\epsilon_\ell} N_\ell^T \tag{6.4}$$

where N_ℓ^T is the number of events with a real lepton in the *tight* sample. This equation illustrates the composition of the multijet background sample; it is the number of *loose-not-tight* events modified by a factor *minus* the number of real lepton events in the *tight* sample modified by another positive factor. It would be sufficient here to derive weights for the *loose-not-tight* events, but I will make one more adjustment for clarity. Substituting Eq. 6.4 into Eq. 6.3 we obtain the total number of events in the *tight* sample:

$$N_T = \frac{f_j}{1-f_j} N_{L-T} + \left(1 - \frac{f_j(1-\epsilon_\ell)}{(1-f_j)\epsilon_\ell}\right) N_\ell^T. \tag{6.5}$$

Rather than being constant values, the efficiencies f_j and ϵ_ℓ are functions of the event kinematics q_i. Using this information we can devise an event-by-event weighting scheme to calculate the number of events in the *tight* sample.

$$\begin{aligned} N_T &= \sum_{i=1}^{N_{L-T}} \frac{f_j(q_i)}{1-f_j(q_i)} + \sum_{i=1}^{N_\ell^T} \left(1 - \frac{f_j(q_i)(1-\epsilon_\ell(q_i))}{(1-f_j(q_i))\epsilon_\ell(q_i)}\right) \\ &= \sum_{i=1}^{N_{L-T}} \Omega_i + \sum_{i=1}^{N_\ell^T} (1-|\omega_i|) \end{aligned} \tag{6.6}$$

The weights Ω_i and $1-|\omega_i|$ are applied to the *loose-not-tight* sample and real lepton events in the *tight* sample, respectively. Real lepton events in the *tight* sample are a source of signal contamination in the multijet background sample. The weight applied to these events is expected to be a second-order effect and as such is only applied to the dominant source of real leptons in the *tight* sample: V+jets events.

The lepton efficiencies ϵ_ℓ are derived from a sample of $Z/\gamma^* \rightarrow \ell\bar{\ell}$ events and are functions of lepton p_T. The jet efficiencies f_j are calculated in an event sample with $5 < \not\!\!E_T < 15\,\mathrm{GeV}$ and no triangle cut (see Section 7.1) meant to reduce the multijet background. All other event selection criteria are applied. In the electron channel the efficiency is parametrized as a function of detector $|\eta|$ in regions of electron p_T and the minimum ϕ angle between the vector $\not\!\!E_T$ and jet $\Delta\phi(\not\!\!E_T, jet)$. The efficiency in the muon channel is parametrized as a function of muon p_T in regions of detector $|\eta|$ and $\Delta\phi(\not\!\!E_T, \mu)$.

Chapter 7

Analysis Method

As described in Chapter 5, searches for the associated production of a Higgs boson H and a vector boson V ($V = W, Z$) are sensitive to the different kinematics of non-standard-model (non-SM) spin and parity J^P states, X, in several observables, namely the invariant mass or transverse mass of the VX system. In this analysis we search for a Higgs boson produced in association with a W boson where the Higgs decays to a pair of b quarks and the W boson decays leptonically to a charged lepton and a neutrino. The tree-level Feynman diagram for this process is shown for reference in Figure 7.1.

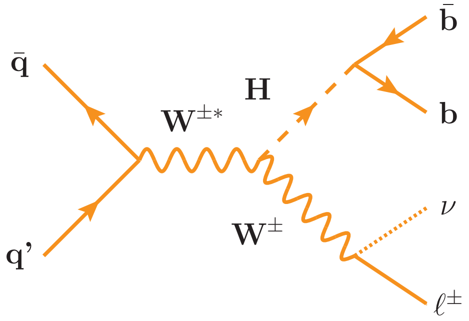

Figure 7.1: *WH Associated Production*
Tree-level Feynman diagram of the $WH \to \ell\nu b\bar{b}$ process.

Many other standard model processes can have the same final state as our signal processes, and are undesirable backgrounds in the search for the signal processes. As discussed in Chapter 6, the largest sources of backgrounds to WH associated production are multijet events, V+light-flavor jets, V+heavy-flavor jets, diboson production VV, single-top events, and top pair production ($t\bar{t}$).

In any search it is necessary to be able to discriminate between signal and background events through event selection and background rejection. Careful event selection maximizes the number of signal events included while minimizing the amount of background. Section 7.1 describes the event selection in detail. Signals can be further discriminated from backgrounds by training a multivariate analysis tool to differentiate between signal and background events using many observables. We use a Boosted Decision Tree (BDT) as described in Section 7.2 for this purpose. The final observable, the transverse mass of the WX system, is discussed in Section 7.3.

7.1 Event Selection

With the goal of reconstructing the W and Higgs bosons, we search for events with one charged lepton (e or μ)[1], significant missing transverse energy, and at least two jets. Additional requirements on the event and objects within the event are applied to help reject backgrounds and aid in object reconstruction. The event selection used in this analysis is described in the following. Table 7.1 summarizes the event selection.

7.1.1 Reconstructing the W Boson

To reconstruct the W boson we require exactly one electron or muon in the event along with significant $\not{E}_T$. Electrons and muons are identified following the prescription in Section 4.4. The $\not{E}_T$ is calculated as described in Section 4.4. Our samples are divided into channels based on the flavor of the identified lepton. In this analysis two sets of identification requirements are applied to leptons in order to form “loose” and “tight” lepton samples. The *loose* lepton

---

[1] We do not select tau leptons directly and their contribution to the event sample is small.

Leptons ($\ell = e$ or μ)	$\not{E}_T$	Jets
1 electron $\|\eta\| < 1.1$ **(CC)** *or* $1.5 < \|\eta\| < 2.5$ **(EC)** $p_T^e > 15\,\text{GeV}$	$\not{E}_T > 15\,\text{GeV}$	**2 *or* 3 jets** divided into **4 b-tagging categories:** *one-tight-tag* (1TT) $\mathcal{D} > 0.15$ *two-loose-tag* (2LT) $0.02 < \bar{\mathcal{D}} \leq 0.35$ *two-medium-tag* (2MT) $0.35 < \bar{\mathcal{D}} \leq 0.55$ *two-tight-tag* (2TT) $\bar{\mathcal{D}} > 0.55$
1 muon $\|\eta\| < 2.0$ $p_T^\mu > 15\,\text{GeV}$	$\not{E}_T > 20\,\text{GeV}$	

Table 7.1: *WX Event Selection*
Summary of the event selection used in the WX analysis. The output of the b-tagging MVA discriminant $\mathcal{D}$ defines the single-b-tagged category while its average $\bar{\mathcal{D}}$ defines the double-b-tagged categories.

sample is used to estimate the multijet background as described in Section 6.4 while the *tight* sample is used to perform the analysis. Figure 7.2 shows the p_T of the lepton for all channels combined.

Electrons are selected in the pseudorapidity regions $|\eta| < 1.1$ and $1.5 < |\eta| < 2.5$ corresponding to the CC and EC calorimeters respectively. They are required to have a transverse momentum of at least 15 GeV. Electrons that pass these cuts are required to satisfy additional identification requirements to form *loose* and *tight* samples. These *loose* and *tight* samples are defined by making different requirements on the output of the electron identification BDT[2]. These samples are chosen to retain a high electron selection efficiency while simultaneously rejecting backgrounds at different rates.

Muons are reconstructed as described in Section 4.4.3.2 and are selected in the pseudorapidity region $|\eta| < 2.0$. Muon candidates must also satisfy $p_T > 15\,\text{GeV}$. We also require a minimum separation between the nearest jet and the muon candidate of 0.5 in η-ϕ space for the *loose* muon sample. The *tight* muon sample satisfies the above requirements and

---

[2] This criterion discriminates between real and fake electrons, allowing for the sample purity to be defined according to the cut made.

has additional isolation requirements: *i*) the scalar sum of the p_T of tracks within a cone of radius $\mathcal{R} = 0.5$ must be less than $0.4 \times p_T^\mu$ and *ii*) the transverse energy in the calorimeter within a hollow cone of $0.1 < \Delta\mathcal{R} < 0.4$ must be less than $0.12 \times p_T^\mu$.

The missing transverse energy $\not{E}_T$, shown in Fig. 7.3, must exceed 15 GeV in the electron channel and 20 GeV in the muon channel. With the information from the $\not{E}_T$ and the lepton we are able to reconstruct the transverse momentum p_T^W and the transverse mass $m_T^W = \sqrt{(E_T^W)^2 - (\vec{p}_T^W)^2}$ of the W boson. The transverse momentum of the W boson is shown in Fig. 7.4. To reduce the multijet background described in Section 6.4 we apply a two-dimensional "triangle" cut of $m_T^W > 40 - 0.5\not{E}_T$.

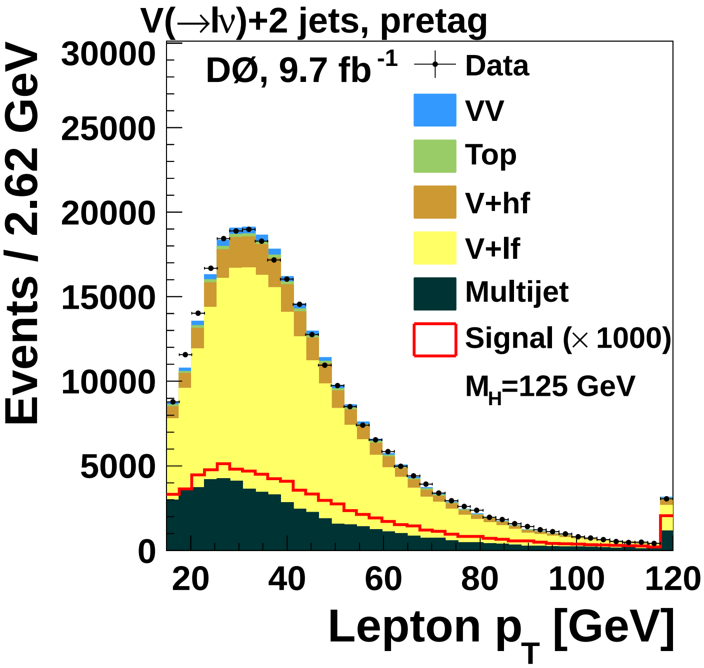

Figure 7.2: *Lepton* p_T
Distributions of lepton p_T for all channels combined.

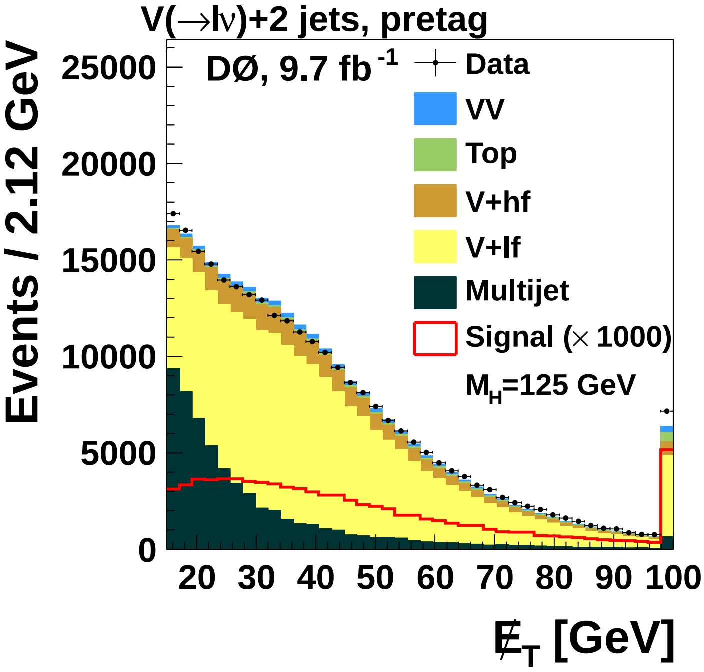

Figure 7.3: *Missing Transverse Energy*
Missing transverse energy for the electron and muon channels combined.

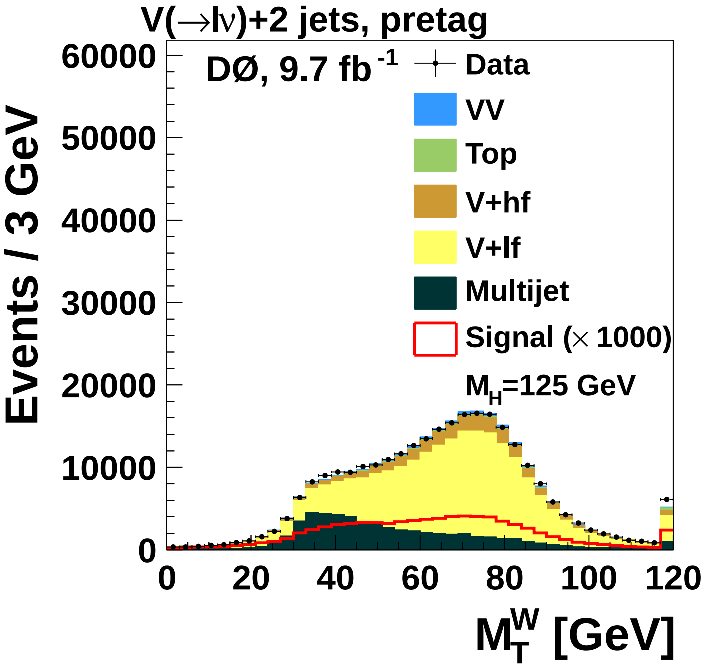

Figure 7.4: *Transverse Mass of the Reconstructed W Boson*
The transverse mass of the W boson as reconstructed by the lepton and $\not{E}_T$ in the electron and muon channels combined.

7.1.2 Reconstructing the Higgs Boson

Higgs bosons with exotic spin and parity are reconstructed in the same manner as the SM Higgs boson with $J^P = 0^+$. In the following, the term 'Higgs boson' refers to the three J^P states considered. At least two jets are required to reconstruct the Higgs boson. We require two or three jets in the event with $p_T > 20\,\text{GeV}$ to account for possible initial-state radiation, pile-up events, or the underlying event. Jets are reconstructed in the pseudorapidity region $|\eta| < 2.5$. Jet transverse momentum distributions are shown in Fig. 7.5. We require that jets originate from the primary vertex. Thus, selected jets must be matched to at least two tracks with $p_T > 0.5\,\text{GeV}$ with at least one hit in the SMT and with a distance of closest approach with respect to the primary vertex of less than 0.5 cm in the transverse plane and less than 1 cm along the beamline.

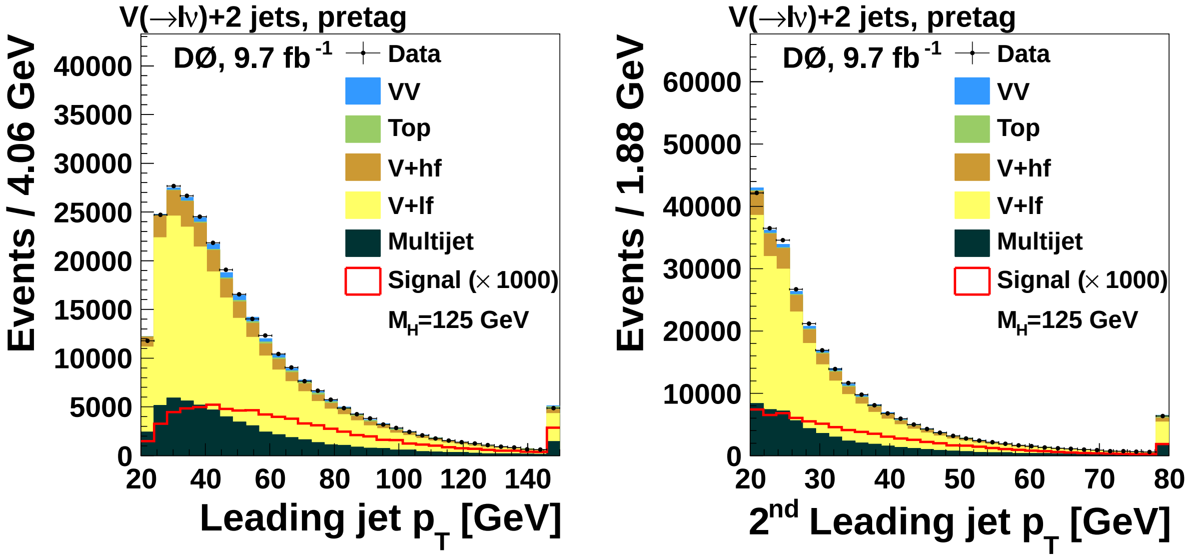

Figure 7.5: *Jet p_T*
Transverse momentum distributions for the leading and 2$^{\text{nd}}$-leading jets before b-tagging is applied. These distributions are for the 2-jet sample and are summed over lepton flavor.

Jets from the decay of the Higgs boson can be identified by their b quark content using the heavy-flavor tagging method described in Section 4.4.2.1. We require one or two of the jets in an event to be b-tagged and define four b-tagging samples by placing requirements on the output of the b-tagging MVA discriminant $\mathcal{D}$. For events with only one b-tagged jet a "tight" requirement of $\mathcal{D} > 0.15$ must be met. This category is referred to as *one-tight-tag* or 1TT. Events with two b-tagged jets are divided into three categories based on the average of the output of the b-tagging MVA for the two jets with the highest MVA output. Figure 7.6 shows the average $\bar{\mathcal{D}} = (\mathcal{D}_{j1} + \mathcal{D}_{j2})/2$ for events with two tagged jets. The *two-loose-tag* (2LT) category corresponds to $0.02 < \bar{\mathcal{D}} \leq 0.35$, the *two-medium-tag* (2MT) category corresponds to $0.35 < \bar{\mathcal{D}} \leq 0.55$, and the *two-tight-tag* (2TT) category corresponds to $\bar{\mathcal{D}} > 0.55$. The Higgs boson is reconstructed from the two b-tagged jets or, in the 1TT category, from the b-tagged jet and the jet with the highest p_T. Figure 7.7 shows the invariant mass of the two jets used to reconstruct the Higgs boson in each b-tag category.

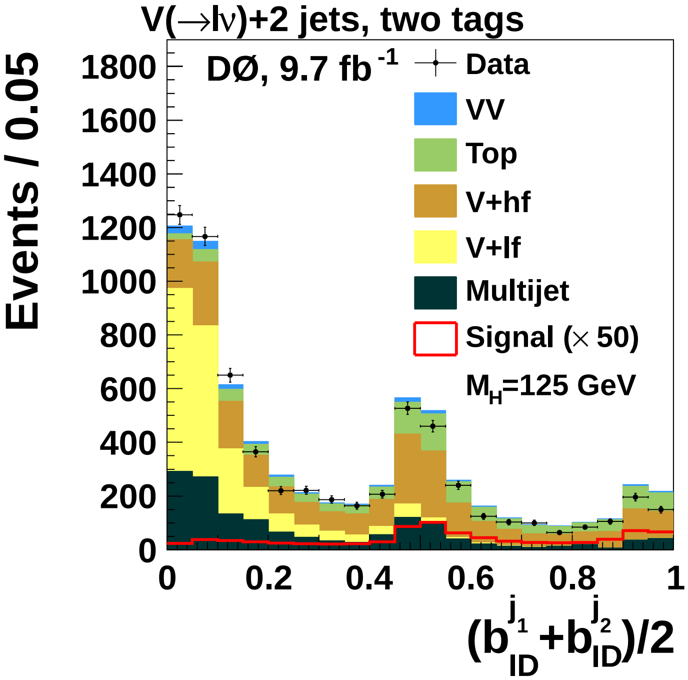

Figure 7.6: *Average b-Tagging MVA Output*
Average b-tagging MVA output for two jets summed over lepton flavors.

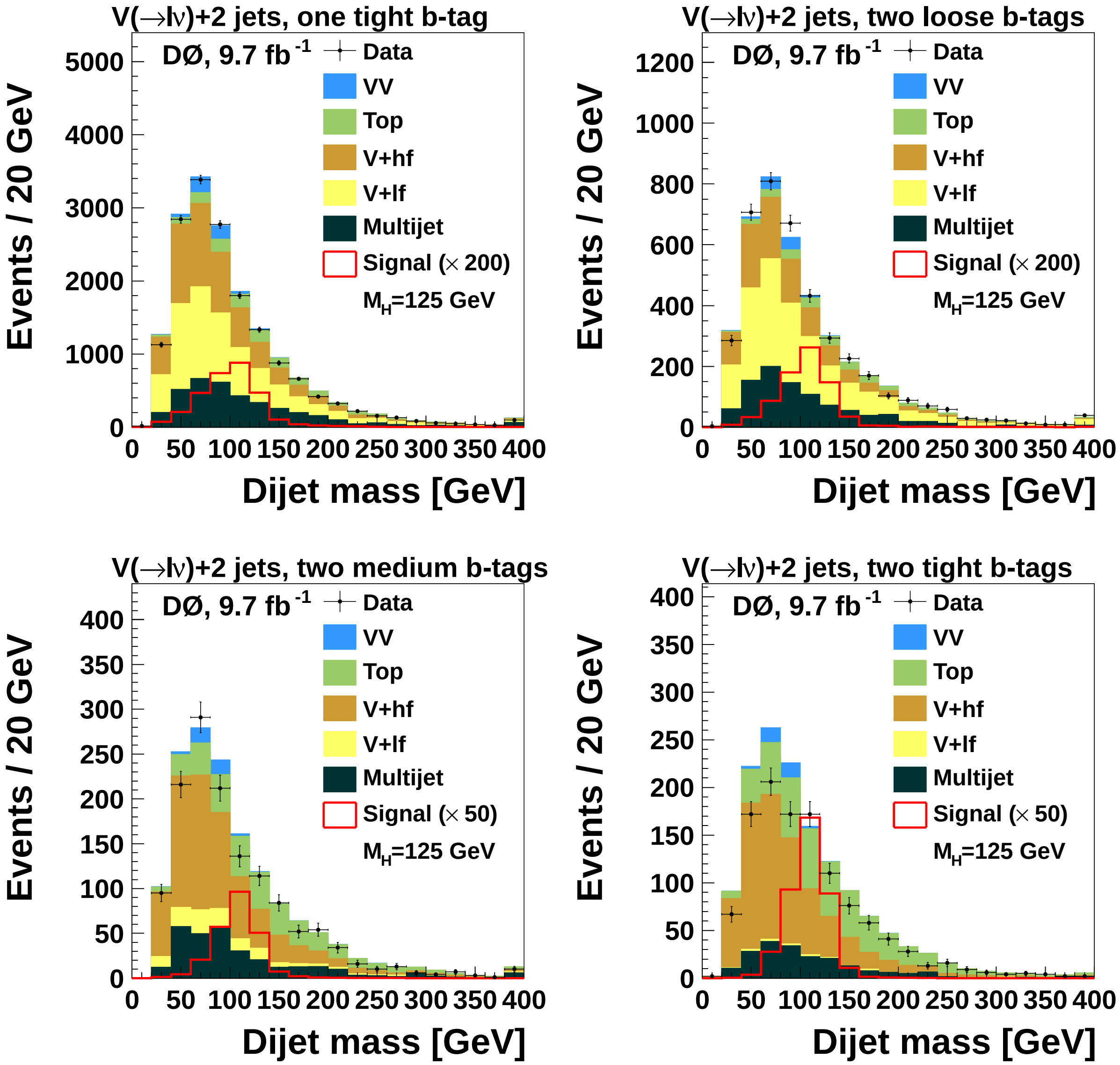

Figure 7.7: *Dijet Invariant Mass*
Dijet invariant mass for each b-tag category for the 2-jet sample combined over lepton flavor.

7.2 Multivariate Analysis Technique

We use a Boosted Decision Tree (BDT) as implemented in the TMVA package[51] to distinguish the SM and non-SM signals from the SM background processes. A decision tree is a classifier that takes events as input and sorts them according to how signal-like or background-like they appear. The output of the decision tree is distributed typically from -1 to 1 with background-like events occupying the lower values and signal-like events occupying the higher values. Decision trees are trained on events from known signal and background classes. Events are split into "leaves" by making cuts on input distributions that maximize signal to background separation. Splitting continues until the resulting leaves have the desired signal purity or a minimum leaf size has been reached. We combine the results of trees trained on random subsets of the input distributions (referred to as *bagging*) to improve the discriminating power. A *boosted* decision tree assigns higher weights to misclassified events on subsequent training cycles. We train a BDT for each lepton flavor, jet multiplicity, and b-tagging channel using SM WH signal events. Because the BDT is primarily sensitive to the mass of the two b quarks and not to the angles between the Higgs boson and the vector boson, we expect to see little difference in the output of the BDT for either non-SM J^P signal. We do not expect any significant bias in either the $J^P = 0^-$ or $J^P = 2^+$ signals if we train only on the SM J^P signal. Figure 7.8 shows the output of the BDT for each b-tagging channel combined in lepton flavor and jet multiplicity.

7.3 Final Observable

Because the z momentum of the neutrino from the decay of the W boson is not measurable, the observable we are primarily interested in is the transverse mass of the WX system defined

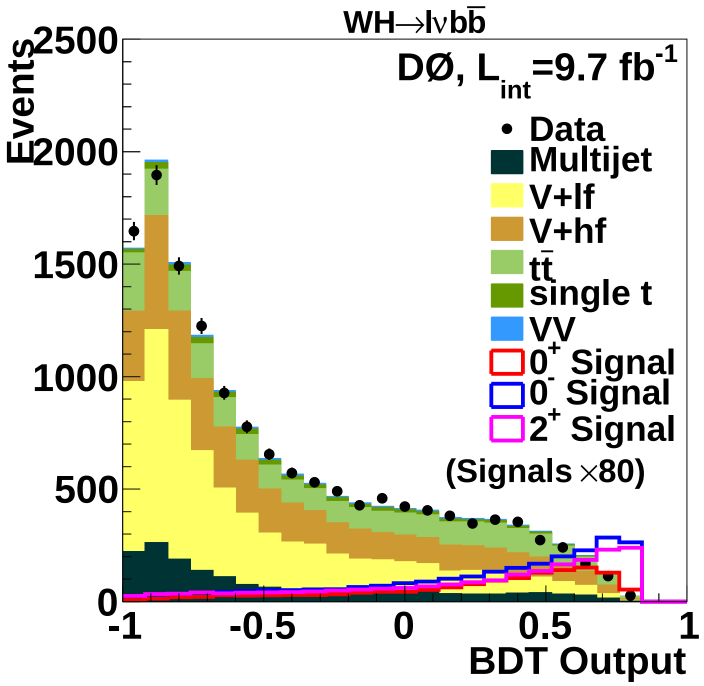

Figure 7.8: *BDT Output*
BDT output combined in lepton flavor, b-tagging category, and jet multiplicity.

as follows.

$$\begin{aligned} m_T^2 &= \left(E_T^W + E_T^H\right)^2 - \left(\vec{p}_T^{\,W} + \vec{p}_T^{\,H}\right)^2 \\ \vec{p}_T^{\,W} &= \vec{\not{E}}_T + \vec{p}_T^{\,\ell} \end{aligned} \tag{7.1}$$

When constructing the p_T and E_T of the Higgs boson we consider either the two b-tagged jets in the case of the two-tag categories or the b-tagged jet and the highest-p_T non-tagged jet in the case of the one-tag category. It is clear from the transverse mass distributions that there is a significant amount of background events, particularly in the region where the SM signal peaks. To improve search sensitivity, we thus split the events into separate purity regions according to the output of the BDT. The most sensitive region with the highest signal purity requires a BDT response value BDT_{out} above 0.5. An intermediate region is defined by $0 < BDT_{out} \leq 0.5$. The lowest purity region are the events with $BDT_{out} \leq 0$. This region provides insignificant sensitivity in the final result relative to the other two regions and we do not include this region in the statistical analysis. The region with a BDT output above 0.5 is referred to as the "high-purity" (HP) channel and the region with $0 < BDT_{out} \leq 0.5$ is referred to as the "low-purity" (LP) channel. The final observables, split into high- and low-purity regions, are given in Figs. 7.9 and 7.10. There are 32 channels that enter into the statistical analysis described in Chapter 8 resulting from splitting the events by lepton flavor, jet multiplicity, b-tagging category, and purity region.

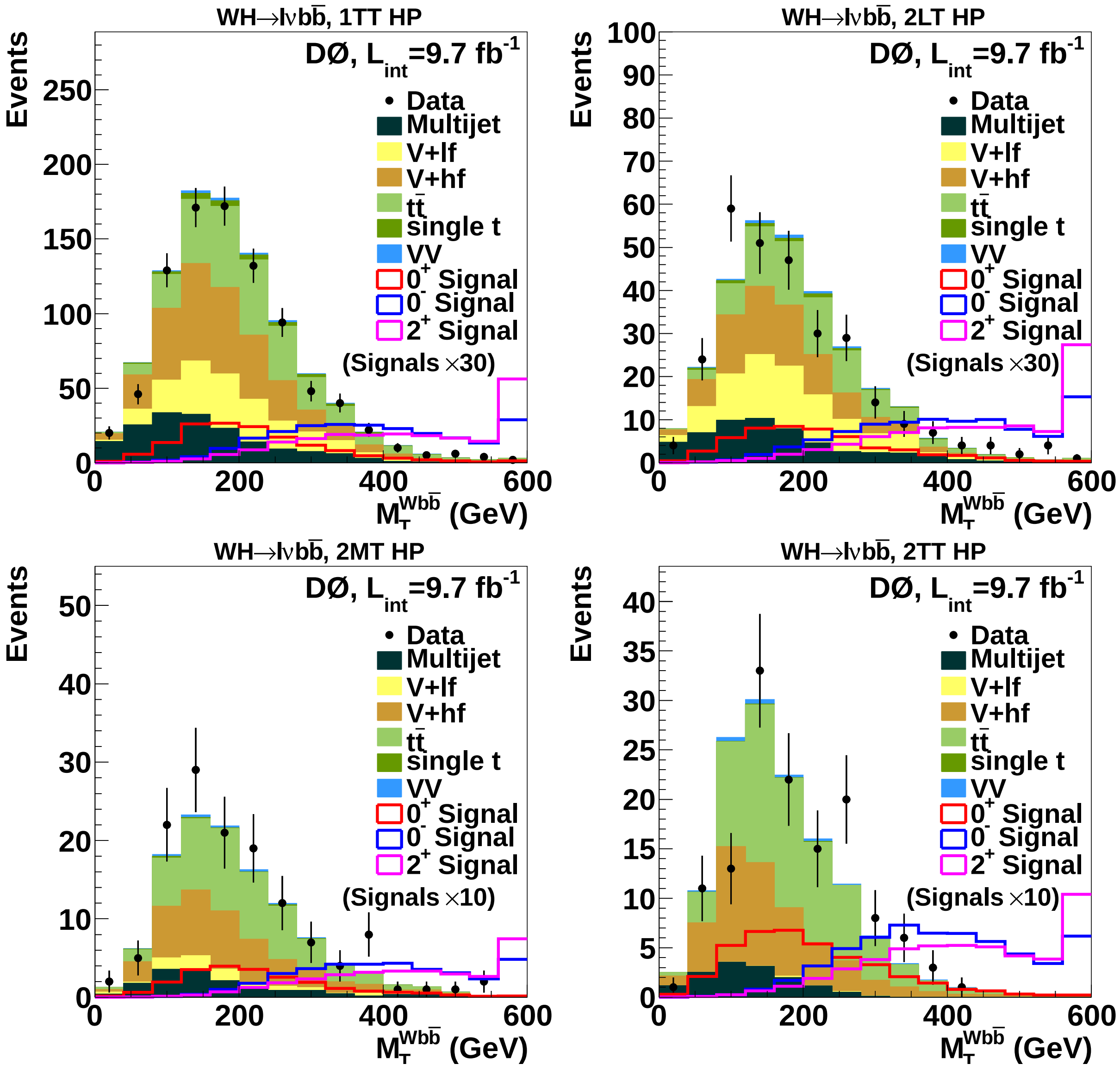

Figure 7.9: *Transverse Mass of the WX System, High-Purity Region*
Transverse mass of the WX system for each of the b-tagging categories in the high-purity channel summed over lepton flavor and jet multiplicity.

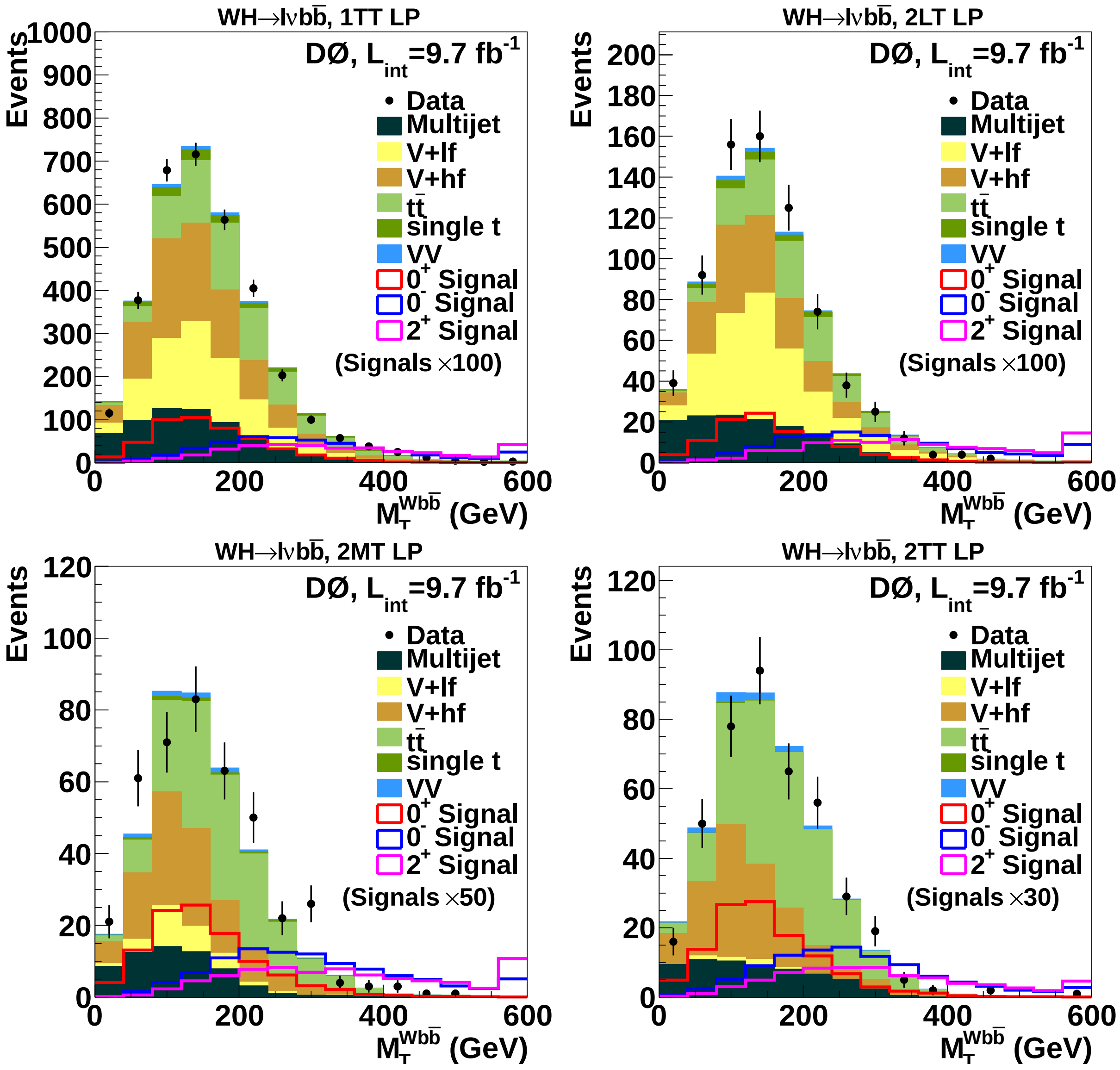

Figure 7.10: *Transverse Mass of the WX System, Low-Purity Region*
Transverse mass of the WX system for each of the b-tagging categories in the low-purity channel summed over lepton flavor and jet multiplicity.

Chapter 8

Statistical Analysis

To answer the questions posed in Chapter 5 we must develop a framework to determine the relative agreement of the data with our SM and non-SM Higgs boson hypotheses. The probabilistic nature of particle interactions leads us to collect a large data sample to look for rare processes and to accurately describe those which are more common. The most natural framework is then a statistical one. Section 8.1 describes the hypothesis test and the test statistic used in this analysis. The particular method we use for interpreting the results of the hypothesis test, the CL_s method, is described in Section 8.2. Finally, a description of the systematic uncertainties present in this analysis is described in Section 8.3.

8.1 The Hypothesis Test

As described in Chapter 7, the result of a search for a new physics process is one or more final variable distributions meant to distinguish between the new physics process and the backgrounds. In this analysis the final variable is the transverse mass of the WH system. We would like to define a hypothesis test based on this distribution that distinguishes between having a Higgs boson with SM J^P and one with exotic J^P. The discriminating power of the transverse mass comes from differences in the shape of the distribution for the SM and non-SM J^P signals. To incorporate the shape of the distribution in the statistical analysis we perform a counting experiment in each bin of the final distribution. In the following, the null hypothesis H_0 refers to the standard model case: the final distribution will contain all SM backgrounds and the SM Higgs boson signal with $J^P = 0^+$. Each test hypothesis H_1 will consider all SM backgrounds and the non-SM Higgs boson with one of the exotic J^P values, $J^P = 0^-$ or $J^P = 2^+$.

The *Neyman-Pearson lemma* states that the likelihood ratio is the most powerful hypothesis test when considering hypotheses which are fully-specified. The likelihood ratio is defined as

$$Q = \frac{\mathcal{L}(H_1|\,\text{data})}{\mathcal{L}(H_0|\,\text{data})} \tag{8.1}$$

where $\mathcal{L}(H|\,\text{data})$ is the likelihood of hypothesis H given the data[1]. If we consider each bin of the final variable distribution as a counting experiment with Poisson statistics then the likelihood of hypothesis H given the distribution of the data is the product of individual Poisson likelihood functions over all bins:

$$\mathcal{L}(H|\,\text{data}) = \prod_{i}^{N_{bins}} \left(\frac{p_i}{d_i}\right)^{d_i} e^{d_i - p_i} \tag{8.2}$$

where p_i is the predicted number of events and d_i is the number of data events in the i^{th} bin. The predicted number of events will depend on the hypothesis considered. For the null hypothesis the predicted number of events will be the sum of the SM Higgs boson signal (s_i^{SM}) and background (b_i) predictions. For the test hypotheses p_i will be the sum of the non-SM Higgs boson signal (s_i^{nSM}) and background (b_i) predictions. Because the natural logarithm is monotonic, we can use the more convenient log-likelihood ratio LLR as our test statistic without sacrificing the power of the likelihood ratio test. This changes the

---

[1] The likelihood is not a probability in the standard sense; it refers to events with known outcomes where the probability deals with future (unknown) events.

product in Eq. 8.2 to a simple summation. For our purposes we define the log-likelihood ratio as $LLR = -2 \ln Q$ where the prefactor is chosen such that $LLR \rightarrow \chi^2$ as the sample size approaches infinity. Combining Eqs. 8.1 and 8.2 and performing some simple arithmetic we obtain

$$LLR = 2 \sum_{i}^{N_{bins}} (s_i^{\text{nSM}} - s_i^{\text{SM}}) - 2 \sum_{i}^{N_{bins}} d_i \ln \left(\frac{s_i^{\text{nSM}} + b_i}{s_i^{\text{SM}} + b_i} \right). \tag{8.3}$$

A test statistic provides an ordering rule with which sets of data can be determined as belonging to one hypothesis over another. More positive values of the LLR defined in Eq. 8.3 indicate that the observed data agree better with the null hypothesis while more negative values indicate better agreement with the test hypothesis. However, without context, the LLR value calculated from the data is essentially meaningless. We can calculate the expected values of the LLR by substituting the d_i in Eq. 8.3 by $s_i^{\text{SM}} + b_i$ or $s_i^{\text{nSM}} + b_i$ but in order to gauge the importance of any deviations we need to know the distribution of LLR values for each hypothesis. This is done by simulating the outcomes of repeated experiments or *pseudo-experiments*. Again, to retain the information stored in the shape of the final variable distribution we proceed with a per-bin calculation. In each bin we assume that the data was drawn randomly from a Poisson parent distribution with a mean equal to the predicted number of events p_i. We then generate pseudo-data by randomly drawing a value from this Poisson parent distribution. We iterate over the total number of bins and the value of the LLR is calculated. This process is repeated many times to create two LLR distributions: one assuming the null hypothesis is true and one assuming the test hypothesis is true.

A complication arises from the fact that the hypotheses we consider are not fully-specified. The background and signal predictions depend on many parameters such as the integrated luminosity, selection efficiencies, and cross sections. These parameters are not of primary interest themselves but must be taken into account because of their associated uncertainties. We refer to them as ‘nuisance parameters’. One method of dealing with these nuisance parameters is to assume they are Gaussian-distributed with a mean equal to the best estimate of the nuisance parameter θ_j^0 and a standard deviation σ_j equal to its uncertainty. By varying the values of the nuisance parameters for each pseudo-experiment we can incorporate the effect their uncertainties have on the results. Changing the values of the nuisance parameters will produce a change in the number of predicted events. For an individual bin, the number of predicted events $\hat{p}_i$ can be written in terms of the nominal prediction p_i and a deviation from the best estimate for each nuisance parameter $R_j = (\theta_j - \theta_j^0)/\sigma_j$ as

$$\hat{p}_i = p_i + \sum_j^{N_{par}} R_j \delta_j \tag{8.4}$$

where δ_j is the fractional change in the number of events for the nuisance parameter j and the sum is over the number of nuisance parameters. This Gaussian represents our prior knowledge of the values of the nuisance parameters. Before generating a set of pseudo-data we vary the values of the nuisance parameters by randomly sampling their Gaussian priors and adjust the predicted number of events accordingly. Next we generate the pseudo-data by randomly drawing a value from the Poisson parent distribution with a mean equal to the (adjusted) predicted number of events. The likelihood function in Eq. 8.2 is modified by the introduction of a Gaussian likelihood term. The likelihood function is thus a product of a Poisson likelihood $\mathcal{L}_\mathcal{P}$ and a Gaussian likelihood $\mathcal{L}_\mathcal{G}$:

$$\begin{aligned} \mathcal{L}(H|\,\text{data}) &= \mathcal{L}_\mathcal{P} \times \mathcal{L}_\mathcal{G} \\ &= \prod_i^{N_{bins}} \left(\frac{\hat{p}_i}{d_i}\right)^{d_i} e^{d_i - \hat{p}_i} \times \prod_j^{N_{par}} e^{-R_j^2/2} \end{aligned} \tag{8.5}$$

where the d_i are the (pseudo-)data and the products go over the number of bins N_{bins} and the number of nuisance parameters N_{par}. Note that the predicted number of events $\hat{p}_i$ is now a function of the deviation R_j. The second term reflects the deviations of the nuisance parameters as a function of their prior which takes into account the relative agreement with the prior estimate.

The uncertainties on the nuisance parameters can be large, sometimes as large as $\approx 30\%$ of the nominal value. Allowing the nuisance parameters to vary according to their uncertainties therefore has the unfortunate effect of diluting the power of the statistical test by broadening the width of the LLR distribution for each hypothesis. We mitigate this effect by performing a "best-fit" to the data by maximizing the likelihood function in Eq. 8.5 over the R_j. The Gaussian likelihood term $\mathcal{L}_{\mathcal{G}}$ serves as a penalty term for the maximization. The effect of the prior is to constrain the fit within the uncertainty of the best estimate. Two fits, one for each hypothesis, are performed for each pseudo-experiment and the data. The final test statistic is the log-likelihood ratio of the maximized likelihood functions and can be summarized as the following:

$$LLR = -2\ln\left(\frac{\mathcal{L}(H_1|\,\mathrm{data}, \hat{\theta})}{\mathcal{L}(H_0|\,\mathrm{data}, \hat{\hat{\theta}})}\right) \tag{8.6}$$

where the $\hat{\theta}$ ($\hat{\hat{\theta}}$) represent the values of the nuisance parameters that maximize the likelihood for the H_1 (H_0) hypothesis.

In the preceding we have implicitly assumed only one source of events but in reality there are often several sources of backgrounds and signals that must enter into the predicted number of events. This can be accomplished with additional summations in Eq. 8.4. Multiple channels can be incorporated in a similar matter. They can either represent subdivisions in the data or a complete set of final variable histograms with their associated predicted number of events and nuisance parameters.

8.2 CL_s Method

After obtaining the LLR distributions we use them to interpret our observed data. Figure 8.1 illustrates example LLR distributions for the null and test hypotheses and well as an example observed value. Two important p-values can be calculated from the LLR distributions and the observed data. A p-value is defined as the probability of obtaining a result at least as or more extreme than what was observed, assuming the hypothesis under consideration is true. If we consider that the test hypothesis is true more extreme LLR values than the observed LLR value lie towards the null hypothesis distribution. The p-value for the test hypothesis p_{test} is therefore the integral of the H_1 LLR distribution to the right of the observed value LLR_{obs} as indicated by the red region in Fig. 8.1. On the other hand if we assume that the null hypothesis is true more extreme values lie towards the test hypothesis distribution and the p-value for the H_0 hypothesis p_{null} is the integral of the H_0 LLR distribution to the left of LLR_{obs}. This is illustrated by the blue region in Fig. 8.1. We select a *significance level* α of 5% against which we will test our result. If the resulting p-value is less than or equal to α we reject the hypothesis at the $1 - \alpha$ confidence level (CL). A strict frequentist interpretation would only consider p_{test} when determining whether to reject the test hypothesis. However, as demonstrated in the previous section, the null and test hypotheses depend on many parameters which can result in poor modeling of either hypothesis. To provide some protection against this poor modeling we use the CL_s method[52, 53, 54]. We define a new quantity CL_s:

$$CL_s = 1 - \frac{p_{\text{test}}}{1 - p_{\text{null}}} \tag{8.7}$$

and use this in determining whether to reject the test hypothesis. If the value of CL_s is greater than $1 - \alpha$ we reject the test hypothesis. In general this method overcovers but is considered acceptable in light of the uncertainty of the modeling process.

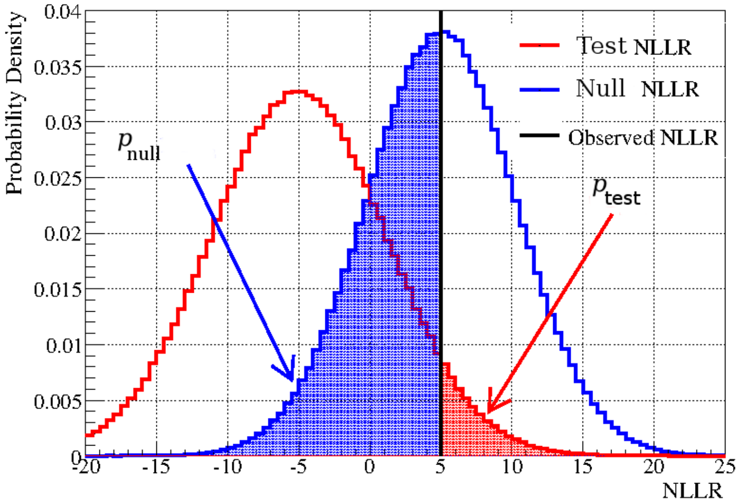

Figure 8.1: *Example LLR Distributions*
Example LLR distributions for the null (blue) and test (red) hypotheses. An example observed LLR value is illustrated by the black line[55].

8.3 Systematic Uncertainties

Systematic uncertainties on the signals and backgrounds are assessed for each lepton flavor, jet multiplicity, and b-tagging category by repeating the analysis independently for each source of uncertainty varied by ±1 standard deviation. Three types of systematics are considered; those affecting the normalization of the final variable, those affecting the shape of the final variable, and those that affect both shape and rate. Sources of systematic uncertainties can come from theoretical predictions, detector effects such as object reconstruction, and the generation of Monte Carlo events. The uncertainty on the integrated luminosity is calculated independently in Ref. [56] to be 6.1%. This systematic is fully correlated across all simulated samples. The following sections describe the sources of our systematic uncertainties and their values in this analysis. Table 8.1 serves as a summary.

	Systematic	Value
Rate	Integrated luminosity	6.1%
	Top quark pair production cross section (σ)	7%
	Single top quark σ	7%
	Diboson σ	6%
	W+heavy-flavor σ	14%
	W+light-flavor σ	4%
	V+jets three-jet scale factor	4% (e) 6% (μ)
	Multijet rate uncertainty	4%–20%
Shape	b-tagging efficiency	4.0%–4.2% per heavy-flavor jet
	Light-flavor jet misidentification	10% per jet
	Jet identification (ID) efficiency	$\sim 3\%$
	Jet smearing, shifting, and removal	1%–4%
	Jet energy resolution	1%–4%
Shape and Rate	Muon trigger efficiency	1%–2%
	Lepton ID	3%
	ALPGEN modeling	0.3%
	Parton Distribution Functions	2%
	Multijet shape uncertainty	4%–30%

Table 8.1: *Systematic Uncertainties*
List of systematic uncertainties affecting rate and/or shape of the final variable distribution.

8.3.1 Modeling Uncertainties

Systematics related to the modeling of simulated samples and those related to the derivation of the multijet sample are described below. In general these uncertainties can affect both event rate and shape.

alpgen modeling: We assess uncertainties for all five ALPGEN reweighting functions used to correct the V+jets samples. We adjust the functions by shifting the parameter that gives the largest shape difference by ±1 s.d. We also evaluate the systematics related to the jet-to-parton matching scheme and the underlying event modeling used by ALPGEN.

V+jets three-jet scale factors: When we simultaneously normalize the V+jets and multijet samples by performing a fit to the data we find that the scaling factors we apply to the 3-jet V+jets sample differ significantly from unity. We therefore apply an additional uncertainty on the 3-jet V+jets sample that is uncorrelated with lepton flavor. We also apply a normalization uncertainty on V+jets events that is anti-correlated with the multijet rate systematic.

Multijet rate: We assign uncertainties on the multijet event rate of 15% in the electron channel and 20% in the muon channel. This systematic is uncorrelated across lepton flavor, jet multiplicity, and b-tagging category.

Multijet shape: To determine the uncertainty on the shape of our multijet estimate we relax the triangle cut introduced in Section 7.1 to $m_T^W > 30 - 0.5\not\!\!E_T$ and repeat the analysis. The positive and negative variations are taken to be symmetric.

8.3.2 Theoretical Uncertainties

Theoretical systematic effects can enter into the analysis from several sources such as predicted cross sections and PDF sets. These can affect both the event rate and shape of the final distribution. We therefore assess uncertainties associated with these items.

Cross section predictions: For single top quark production and top quark pair production this uncertainty is 7%[57, 58] The uncertainty on the diboson production cross section is 6%[59]. The uncertainties on W+hf and W+lf production are 14% and 4%, respectively. The uncertainties on W+hf are estimated with MCFM[60, 61].

PDF sets: Sets of parton distribution functions are calculated from theory and experimental results. The choice of PDF set used in Monte Carlo event generation affects the signal and background rates. We assign an uncertainty of 2% to account for this.

8.3.3 Jet Systematics

There are several systematics associated with the presence of jets in the final state. These uncertainties come from detector effects, object reconstruction, and b-tagging algorithms.

Jet energy scale: The energy we measure for a jet is corrected to account for detector effects such as uranium decay in the calorimeter, electronics noise, residual energy from previous collisions, and inactive areas of the detector. This correction is referred to the Jet Energy Scale (JES) correction and it is applied to both the data and MC events. The uncertainty on the JES correction is assessed by shifting the JES parameters up and down by 1 s.d.

Jet smearing, shifting, and removal: Jets produced in MC events must be smeared and shifted in energy to match the characteristics of jets in data. We apply the Jet Smearing Shifting and Removal (JSSR) correction to jets in MC. The uncertainty on this correction is found by shifting the parameters by ±1 s.d.

Jet identification: We assign a 2% uncertainty on the jet identification efficiency.

***b* quark identification:** The uncertainty on the b-tagging efficiency is determined by varying the tagging rate functions up and down 1 s.d. in samples containing heavy-flavor jets. The uncertainty on the light-flavor misidentification rate is determined by varying the light-flavor tag rates by ±1 s.d. in samples with no heavy-flavor jets.

8.3.4 Lepton Systematics

There are several systematics associated with the presence of leptons in the final state. These systematics can affect both event rate and shape.

Electron identification: We assign an uncertainty of 3% on the electron identification efficiency. Included in this uncertainty is the uncertainty associated with the EM trigger.

Muon identification: We also assign an uncertainty of 3% on the muon identification efficiency.

Muon trigger: The ALPGEN reweightings are calculated using the $T_{\mu OR}$ trigger suite and applied to both events with electrons and events with muons. Additional reweightings are applied to the muon channel which are calculated from events selected with T_{incl}. To account for the difference between the ALPGEN reweightings as applied to the electron events and muons events we apply an uncertainty on the muon trigger. It is calculated as the difference between applying the nominal trigger correction and applying a trigger correction derived using the ALPGEN reweightings calculated using the $T_{\mu OR}$ trigger suite.

Chapter 9

Results and Interpretations

The statistical method outlined in Chapter 8 can be used to investigate several questions related to the spin and parity of the particle discovered at the LHC. Is the new particle really the SM Higgs boson? At what level can we exclude other non-SM J^P assignments? Is the particle an admixture of different J^P states? Under the assumption that it is, would it be possible to rule out any fraction of non-SM J^P content? To answer these questions, I've divided the results into two cases:

1. **The new particle exists as a pure J^P state**

   Of primary interest is whether or not the new particle is the SM Higgs boson. Since the Tevatron cannot measure the spin and parity of the particle directly we can only exclude models with exotic J^P. Whether or not we exclude these models depends in part on the total predicted cross section for the process. Unfortunately, the total predicted cross section for the $J^P = 0^-$ and $J^P = 2^+$ states is incalculable and the exclusion will depend on an assumed signal cross section. One very reasonable starting point would be the observed rate in data.

2. **The new particle exists as an admixture of J^P states**

   Another important possibility to exclude is whether the discovered particle is a pure J^P state or an admixture of J^P states. Excluding this possibility in its entirety requires excluding all possible fractions of non-SM signals. Any exclusions in this case will again depend on an assumed total cross section. This analysis is limited to cases where the different J^P states do not interfere.

Section 9.1 defines the hypothesis tests for cases (1) and (2) in detail. The results of these tests for the $WX \to \ell\nu b\bar{b}$ analysis are discussed in Section 9.2. Details for the combination of the $ZX \to \ell\ell b\bar{b}$ and $VX \to \nu\nu b\bar{b}$ analyses with the $WX \to \ell\nu b\bar{b}$ analysis are discussed in Section 9.3. Results of the combination within D0 and with CDF are discussed in the same section.

9.1 Hypothesis Construction

In the previous chapter we loosely defined the hypothesis tests for the sake of simplicity. Here they are defined in detail. The null hypothesis we want to consider for both cases is that the data is described by the standard model backgrounds and a boson with $J^P = 0^+$. To investigate the exclusion potential for other values of the cross section we normalize the SM signal to $\mu \times \sigma_{0^+}^{\mathrm{SM}}$ where μ is the signal strength and $\sigma_{0^+}^{\mathrm{SM}}$ is the Higgs boson SM cross section times branching ratio. The normalization of the SM background processes remains the same as what is described in Chapter 6.

The test hypothesis for case (1) assumes that the data is described by the SM backgrounds and a boson with exotic spin and parity, either $J^P = 0^-$ or $J^P = 2^+$. For case (2) the assumption is that the data contains an admixture of two different J^P states – one with exotic J^P and one with $J^P = 0^+$. Because the test hypotheses are very similar we can define a general hypothesis test that can be applied in both cases. The general hypothesis is the sum of the SM backgrounds, the SM signal, and the non-SM signal with $J^P = 0^-$ or $J^P = 2^+$. Like the null hypothesis, the normalization of the SM backgrounds remains as described previously. The normalizations of the signals are defined based on the fraction of non-SM signal $f_{J^P} = \sigma_{J^P}/(\sigma_{J^P} + \sigma_{0^+})$. The non-SM J^P signal is normalized to $\mu_{\text{tot}} \times \sigma_{0^+}^{\text{SM}} \times f_{J^P}$ and the SM J^P signal is normalized to $\mu_{\text{tot}} \times \sigma_{0^+}^{\text{SM}} \times (1 - f_{J^P})$ so that the overall normalization is equal to $\mu_{\text{tot}} \times \sigma_{0^+}^{\text{SM}}$. For the case assuming a pure non-SM J^P state, $f_{J^P} = 1$ and the total signal strength μ_{tot} is simply equal to the non-SM J^P signal strength μ_{J^P}. Table 9.1 summarizes the signal normalizations for the null and test hypotheses.

Hypothesis	SM signal normalization	non-SM signal normalization
Null hypothesis H_0	$\mu \times \sigma_{0^+}^{\text{SM}}$	–
Test hypothesis H_1	$\mu_{\text{tot}} \times \sigma_{0^+}^{\text{SM}} \times (1 - f_{J^P})$	$\mu_{\text{tot}} \times \sigma_{0^+}^{\text{SM}} \times f_{J^P}$

Table 9.1: *Signal Normalizations*
Signal normalizations for the null and test hypotheses. The fraction of non-SM J^P signal is denoted by f_{J^P}. For the case of a test hypothesis with pure non-SM J^P signal, $f_{J^P} = 1$ and $\mu_{\text{tot}} = \mu_{J^P}$.

9.2 WX Analysis Results

Discrimination between non-SM and SM J^Passignments is achieved by analyzing the distribution of the transverse mass of the WX system. The transverse mass m_T of the WX system is defined in Eq. 7.1. To increase the sensitivity the event sample has been divided into orthogonal channels based on lepton flavor, jet multiplicity, b-tagging category, and signal purity region. Figure 9.1 shows the transverse mass of the WX system for the two-tight-tag high-purity channel. Plots for other channels can be found in Chapter 7.

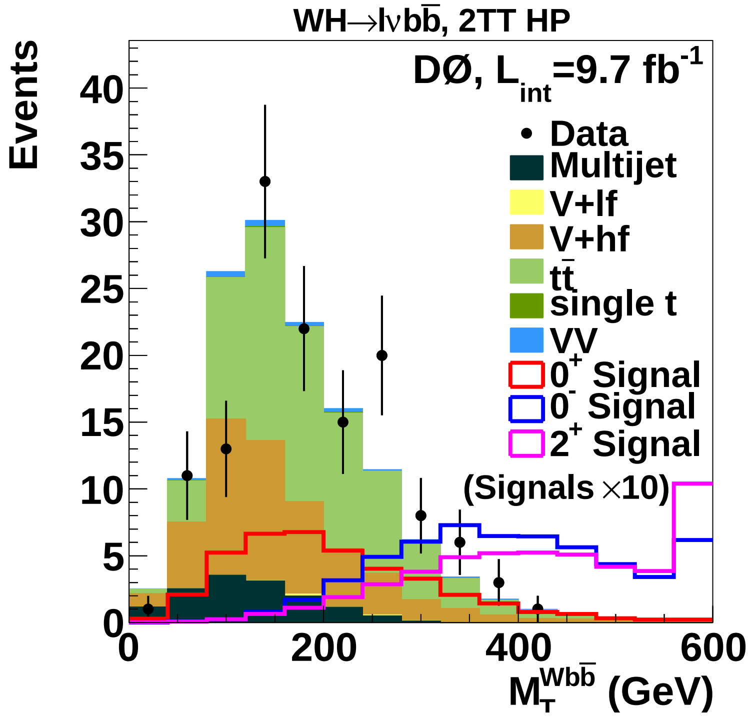

Figure 9.1: *Transverse Mass of the WX System, High-Purity Region*
Transverse mass of the WX system for the two-tight-tag b-tagging category. Other plots can be found in Chapter 7.

9.2.1 Pure Non-SM J^P States

We first consider the case where the signal is a pure non-SM J^P state. Here the non-SM J^P signal fraction f_{J^P} is one and $\mu_{\text{tot}} = \mu_{J^P}$. We are free to choose any values for μ and μ_{J^P}, the signal strengths for the SM and non-SM signals in the calculation. This choice is arbitrary and smaller values simply reduce the sensitivity of the test. One simple choice is the SM predicted value for Higgs boson production: $\mu = \mu_{J^P} = 1.0$. This choice is what we expect from the SM and is an easy point for comparison with other analyses. We perform the statistical analysis with the signal normalizations listed in Table 9.1 for the $J^P = 0^-$ and $J^P = 2^+$ signals individually. Figures 9.2 and 9.3 show the distribution of the log-likelihood ratio (LLR) test statistic calculated for each pseudoexperiment and the data for $J^P = 0^-$ and $J^P = 2^+$, respectively.

By examining the expected LLR distributions we can get an idea of the discriminating power of the transverse mass for the $J^P = 0^-$ and $J^P = 2^+$ signals. Because the test statistic is an ordering rule we expect that the farther apart the null and test hypotheses are the more discriminating power there is. For example, if the null and test hypotheses produce LLR distributions that overlap completely it will be impossible to discriminate between them no matter where the observation falls. Comparing Figs. 9.2 and 9.3 we see that the two distributions are closer together in the case of $J^P = 0^-$ than they are for $J^P = 2^+$. This suggests that the discriminating power is stronger for the case of $J^P = 2^+$ than for $J^P = 0^-$. This also agrees with the transverse mass distribution in Fig. 9.1. The $J^P = 0^-$ signal peaks significantly closer to the SM signal and backgrounds than the $J^P = 2^+$ signal. In addition to the expected LLR distributions we can consider the observed value. In both cases the observed value falls just inside 2 standard deviations (s.d.) from the median expected value.

This indicates an excess in the data from an upward fluctuation. In Figure 9.1 some of this excess is visible in 4–5 bins which are in the tail of the distribution. Since this plot represents the channel with the most sensitivity in the $WX \to \ell\nu b\bar{b}$ analysis, it is not surprising that we see an overall excess.

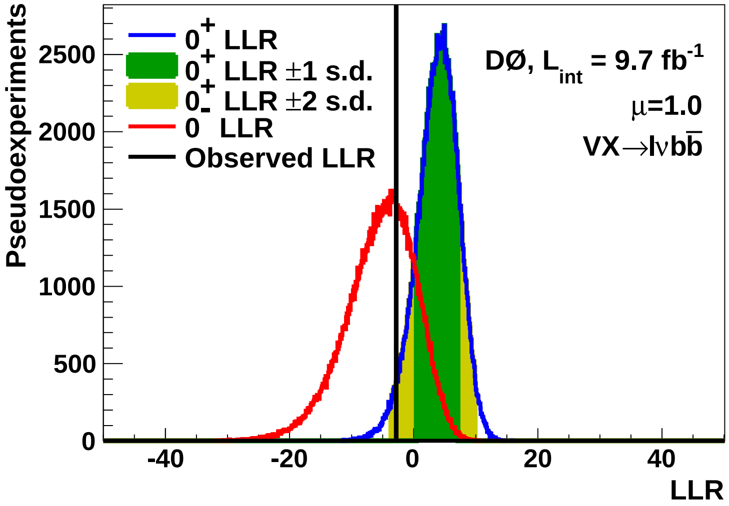

Figure 9.2: *Log-likelihood Ratio Distributions for* $J^P = 0^-$
The log-likelihood ratio (LLR) test statistic calculated for each pseudoexperiment and the data assuming $\mu = 1.0$ for $J^P = 0^-$. The LLR distribution for the null (test) hypothesis is shown in blue (red) and the observed value is represented by the black vertical line. The green and yellow shaded bands represent 1 and 2 standard deviations on the median expectation from the null hypothesis, respectively.

We proceed to calculate the p-values by integrating the LLR distributions for each hypothesis from the observed value to $\pm\infty$. We denote the p-value for the null hypothesis as p_{null} and the p-values for the test hypotheses as $p_{\text{test}}^{0^-}$ and $p_{\text{test}}^{2^+}$. The value of CL_s is calculated as $1 - p_{\text{test}}/(1 - p_{\text{null}})$. We interpret CL_s as the confidence level at which we exclude the non-SM test hypothesis in favor of the SM prediction. If $CL_s \geq 0.95$ we exclude the test hypothesis in favor of the null hypothesis at a confidence level $\geq 95\%$. To calculate the expected p-values we instead integrate from the median expectation of the null hypothesis. Table 9.2 gives the expected and observed p-values as well as the value of CL_s assuming

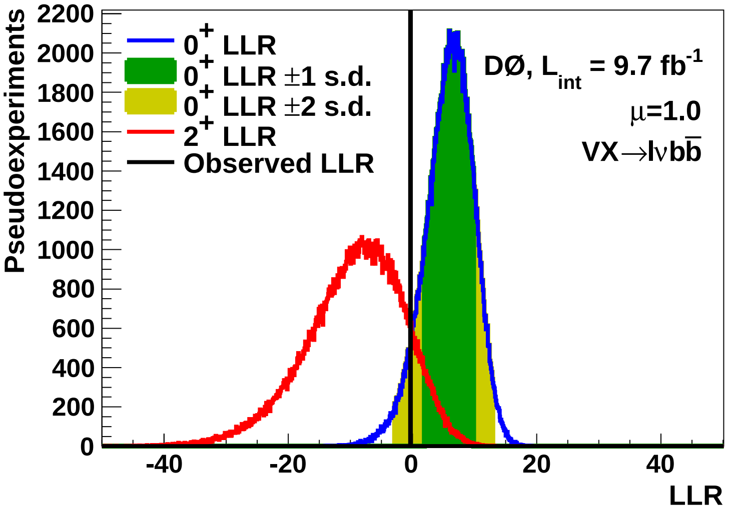

Figure 9.3: *Log-likelihood Ratio Distributions for* $J^P = 2^+$
The log-likelihood ratio (LLR) test statistic calculated for each pseudoexperiment and the data assuming $\mu = 1.0$ for $J^P = 2^+$. The LLR distribution for the null (test) hypothesis is shown in blue (red) and the observed value is represented by the black vertical line. The green and yellow shaded bands represent 1 and 2 standard deviations on the median expectation from the null hypothesis, respectively.

$\mu = \mu_{J^P} = 1$. We also give the corresponding significance in units of standard deviations (s.d.) using a one-sided Gaussian tail calculation. When testing a pure non-SM J^P state of $J^P = 0^-$ our expected CL_s value is 0.941 and we observe a value of 0.637. Although we do not expect to be able to exclude the $J^P = 0^-$ hypothesis our observed value is much lower. This is due to an upwards fluctuation in the data near the tail of the transverse mass distribution.

The $WH \rightarrow \ell\nu b\bar{b}$ channel is one of the inputs to the SM Higgs boson search at D0 that yielded an excess in the data above the SM expectation consistent in both shape and rate to the Higgs boson discovered at the LHC. When we combine all channels in which the Higgs boson decays to a pair of b quarks we can measure the signal strength of this excess by performing a best fit to the data. This gives a value of $\mu = 1.23$. By setting $\mu = 1.23$ and repeating the analysis we can attempt to scale the signal to match what we measure from

$J^P = 0^-$ vs. $J^P = 0^+$	
$p_{\text{test}}^{0^-}$ Expected	0.030
$p_{\text{test}}^{0^-}$ Observed	0.351
$1 - p_{\text{null}}$ Expected	0.500
$1 - p_{\text{null}}$ Observed	0.965
CL_s Expected	0.941 (1.56 s.d.)
CL_s Observed	0.637 (0.35 s.d.)
$J^P = 2^+$ vs. $J^P = 0^+$	
$p_{\text{test}}^{2^+}$ Expected	0.009
$p_{\text{test}}^{2^+}$ Observed	0.114
$1 - p_{\text{null}}$ Expected	0.500
$1 - p_{\text{null}}$ Observed	0.932
CL_s Expected	0.982 (2.09 s.d.)
CL_s Observed	0.878 (1.16 s.d.)

Table 9.2: *D0* CL_s *Values for* $\mu = 1.0$
Expected and observed p-values and CL_s values for $J^P = 0^-$ and $J^P = 2^+$ WX associated production, assuming signal cross sections equal to the 125 GeV SM Higgs production cross section multiplied by $\mu = 1.0$. The null hypothesis is taken to be the sum of the SM Higgs boson signal and background production.

the best fit. However, the $WH \to \ell\nu b\bar{b}$ channel is only one of several inputs to the $H \to b\bar{b}$ combination so this is only an approximation. Table 9.3 gives the p-values for the case of $\mu = \mu_{J^P} = 1.23$ for both $J^P = 0^-$ and $J^P = 2^+$ states. We observe a CL_s value of 0.747 with an expected value of 0.975. Again, the observed value is much less than the expected value.

$J^P = 0^-$ vs. $J^P = 0^+$		
$p_{\text{test}}^{0^-}$	Expected	0.012
$p_{\text{test}}^{0^-}$	Observed	0.245
$1 - p_{\text{null}}$	Expected	0.500
$1 - p_{\text{null}}$	Observed	0.971
CL_s	Expected	0.975 (1.96 s.d.)
CL_s	Observed	0.747 (0.67 s.d.)
$J^P = 2^+$ vs. $J^P = 0^+$		
$p_{\text{test}}^{2^+}$	Expected	0.003
$p_{\text{test}}^{2^+}$	Observed	0.056
$1 - p_{\text{null}}$	Expected	0.500
$1 - p_{\text{null}}$	Observed	0.937
CL_s	Expected	0.995 (2.56 s.d.)
CL_s	Observed	0.941 (1.56 s.d.)

Table 9.3: *D0 CL_s Values for $\mu = 1.23$*
Expected and observed p-values and CL_s values for $J^P = 0^-$ and $J^P = 2^+$ WX associated production, assuming signal cross sections equal to the 125 GeV SM Higgs production cross section multiplied by $\mu = 1.23$.

9.3 Combining Analyses

The method for discriminating between SM and non-SM J^P states outlined in Chapter 5 can be applied to all vector boson associated Higgs boson production channels. These VH production channels include $ZH \to \ell\ell b\bar{b}$, $WH \to \ell\nu b\bar{b}$, and $VH \to \nu\nu b\bar{b}$. Tree-level Feynman diagrams for these processes are given in Fig. 9.4. If we combine the results of this analysis with the results from similar analyses of the $ZH \to \ell\ell b\bar{b}$ and $VH \to \nu\nu b\bar{b}$ production channels we will increase the sensitivity of the final result beyond any of the individual analyses. The statistical method we've used is amenable to combining many analysis channels and gives us no obstacles. The only modification necessary when including these additional processes is the form of the final discriminating distribution. As described in Chapter 5 we use the transverse mass of the WH system because we cannot measure the z momentum of the neutrino in the final state. For the $VH \to \nu\nu b\bar{b}^1$ channel this requires a small modification to the transverse mass:

$$\begin{aligned} m_T^2 &= (E_T^V + E_T^X)^2 - (\vec{p}_T^V + \vec{p}_T^X)^2, \\ p_T^V &= \not{E}_T. \end{aligned} \tag{9.1}$$

On the other hand, for the $ZH \to \ell\ell b\bar{b}$ channel we detect both charged leptons and we can use the invariant mass of the ZH system:

$$m^2 = (E_Z + E_X)^2 - (\vec{p}_Z + \vec{p}_X)^2. \tag{9.2}$$

To avoid double-counting the event samples for the three VH production processes are orthogonal with respect to the number of detected leptons. Since the statistical method can combine any number of analysis channels we perform the combination of these processes both within the D0 experiment and within the Tevatron as a whole. Section 9.4 describes briefly the analysis methods of the $ZH \to \ell\ell b\bar{b}$ and $VH \to \nu\nu b\bar{b}$ channels at the D0 experiment and discusses the results from the combination. The combination with the CDF experiment is discussed in Section 9.5.

---

[1] Although the physical process associated with this production channel is strictly a Z boson decaying to a pair of neutrinos, we must also consider the possibility that the production is actually $WH \to \ell\nu b\bar{b}$ and we do not detect the charged lepton. This accounts for $\sim 50\%$ of the total events.

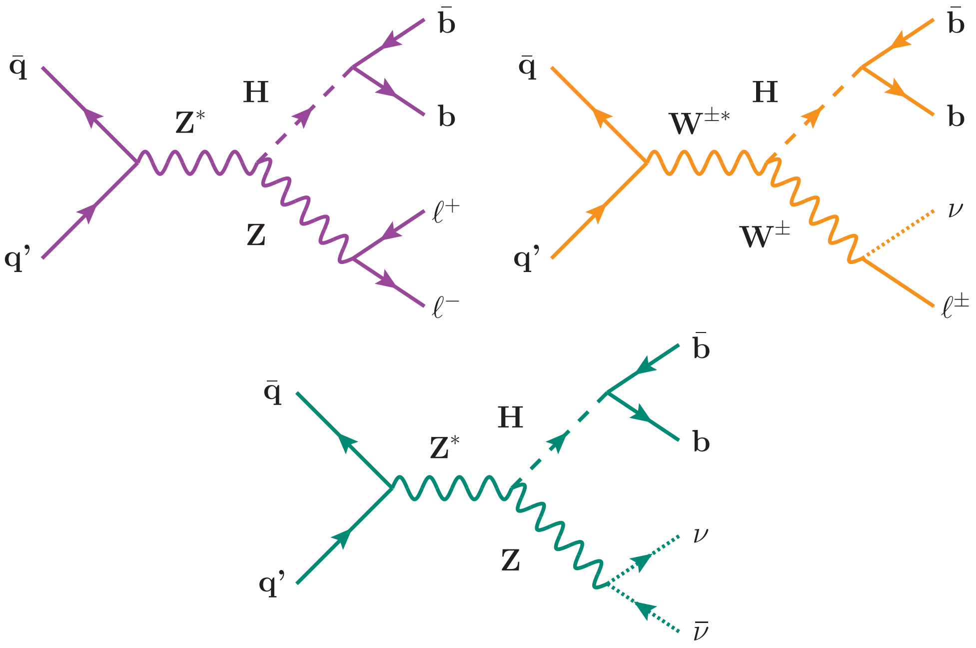

Figure 9.4: *VH Associated Higgs Boson Production*
Tree-level Feynman diagrams of vector boson associated Higgs boson production.

9.4 D0 Combination

The D0 combination includes the $ZH \to \ell\ell b\bar{b}$, $WH \to \ell\nu b\bar{b}$, and $VH \to \nu\nu b\bar{b}$ production channels. These channels are included in the D0 SM Higgs boson search[62]. The best fit to the data in the $H \to b\bar{b}$ combined analysis for the signal cross section multiplied by the branching ratio is $\mu = 1.23$. The individual analyses are described in detail in Ref. [39] ($ZH \to \ell\ell b\bar{b}$), Ref. [63] ($WH \to \ell\nu b\bar{b}$), and Ref. [64] ($VH \to \nu\nu b\bar{b}$).

The $ZH \to \ell\ell b\bar{b}$ analysis selects events with at least two isolated charged leptons and at least two jets. This channel uses a kinematic fit to correct the measured jet energies to their best fit values. We perform the fit by constraining the invariant mass of the lepton pair to be consistent with the mass of the Z boson and the total transverse momentum of the leptons and jets to be consistent with zero. We divide the events into two b-tagging categories depending on the number of b quark jets tagged in the event: a “single-tag” category (ST) and a "double-tag" category (DT). The SM Higgs boson search[39] uses Random Forest discriminants to produce the final distributions for the statistical analysis.

One of these Random Forests provides discrimination against top quark pair production and divides the events into $t\bar{t}$-enriched and $t\bar{t}$-depleted regions. For the spin and parity analysis only the events in the $t\bar{t}$-depleted region are considered[2]. The invariant mass is constructed from the two leptons and either the two b-tagged jets (DT) or one tagged jet and the untagged jet with the highest p_T. To improve the discrimination between the non-SM signals and the backgrounds we use the invariant mass of the dijet system M_{jj} to select two regions with different purity regions. The invariant mass of the dijet system is shown in Fig. 9.5. Events with $100 \leq M_{jj} \leq 150\,\mathrm{GeV}$ comprise the "high-purity" region while the remaining events are in the "low-purity" region. Figure 9.6 shows the invariant mass distribution of the ZH system for the DT b-tagging category in the high-purity region. Additional distributions are given in Appendix C.

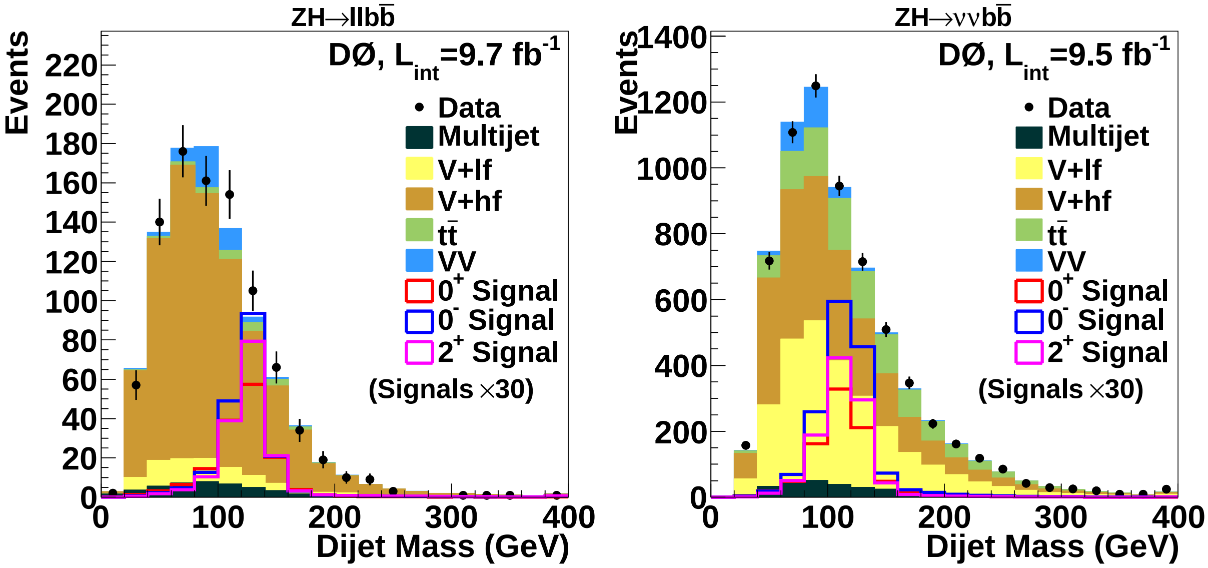

Figure 9.5: *$ZH \rightarrow \ell\ell b\bar{b}$ and $VH \rightarrow \nu\nu b\bar{b}$ Dijet Invariant Mass*
Dijet invariant mass for the $ZH \rightarrow \ell\ell b\bar{b}$ and $VH \rightarrow \nu\nu b\bar{b}$ channels.

---

[2] This region contains roughly 94% of the signal.

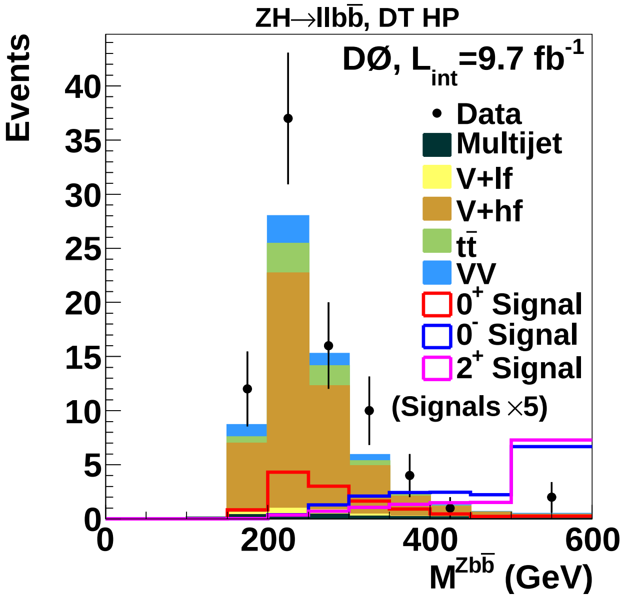

Figure 9.6: *Invariant Mass of the ZH System*
Invariant mass of the $ZH \to \ell\ell b\bar{b}$ system for the DT b-tagging category in the high-purity region.

The SM Higgs boson search in the $VH \to \nu\nu b\bar{b}$ channel selects events with a large $\not\!\!E_T$ and exactly two jets. This channel is sensitive to WH associated production when the charged lepton is not detected. The jets are classified into two b-tagging categories depending on the sum of the scores provided by the tagging algorithm. These categories are referred to as "medium" (MT) and "tight" (TT). We use a dedicated boosted decision tree to provide some rejection of the multijet background. The SM Higgs boson search uses a boosted decision tree discriminant as the final distribution in the statistical analysis.

The transverse mass of the VH system is constructed from the $\not\!\!E_T$ and the two selected jets. We use the invariant mass of the dijet system to again divide the events into high- and low-purity regions. Figure 9.5 illustrates the dijet invariant mass for the $VH \to \nu\nu b\bar{b}$ channel. This channel defines the high-purity region to include those events with $70 \leq M_{jj} < 150\,\text{GeV}$ while the low-purity region contains the remaining events. The transverse mass distribution for the TT b-tagging channel in the high-purity region is shown in Fig. 9.7.

Other distributions can be found in Appendix C.

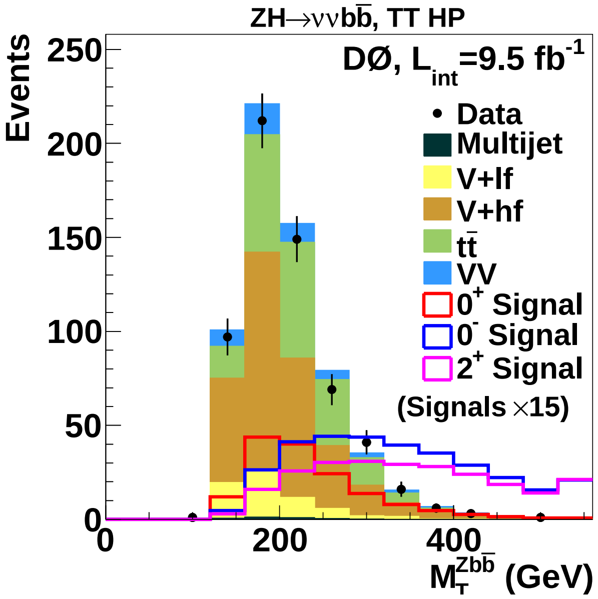

Figure 9.7: *Transverse Mass of the VH System*
Transverse mass of the $VH \rightarrow \nu\nu b\bar{b}$ system for the TT b-tagging category in the high-purity region.

9.4.1 D0 Combination Results: Pure Non-SM J^P States

Assuming the data is described by a pure non-SM J^P state for the test hypothesis we calculate the LLR test statistic for two values of μ: $\mu = 1.0$ corresponding to the SM prediction and $\mu = 1.23$ corresponding to the best fit value measured in the combined D0 $H \rightarrow b\bar{b}$ channel. The LLR distributions for $\mu = 1.0$ are given in Fig. 9.8. Log-likelihood ratio plots for the $ZH \rightarrow \ell\ell b\bar{b}$ and $VH \rightarrow \nu\nu b\bar{b}$ channels individually are given in Appendix C.

From the LLR distributions we calculate the p-values as before. Table 9.4 lists the p-values as well as CL_s for each channel individually as well as the combination for $\mu = 1.0$. The corresponding table assuming $\mu = 1.23$ can be found in Appendix C. We are able to exclude models with $J^P = 0^-$ at the 97.6% confidence level (CL) assuming $\mu = 1.0$. The expected exclusion is at the 99.86% CL. We exclude models with $J^P = 2^+$ at the 99.0%

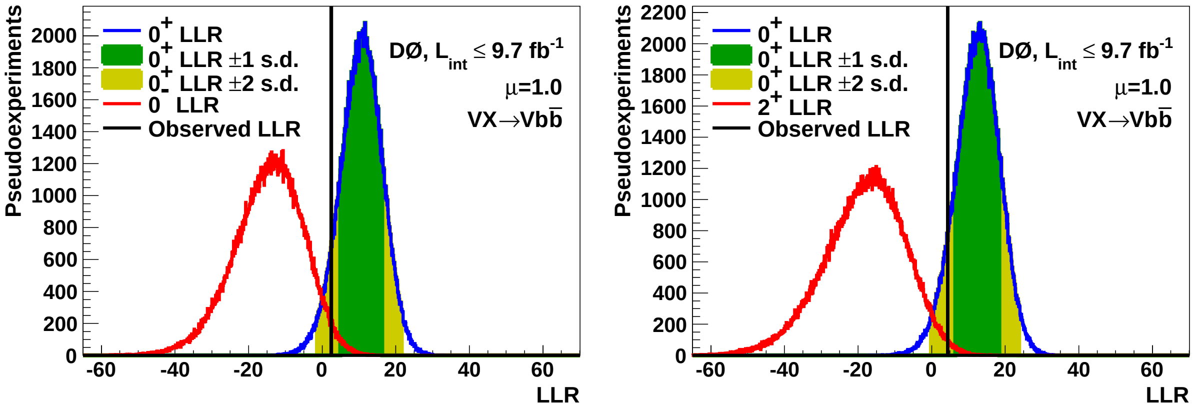

Figure 9.8: *D0 Combination LLR Distributions for* $\mu = 1.0$
LLR distributions for the D0 combination of the $ZH \rightarrow \ell\ell b\bar{b}$, $WH \rightarrow \ell\nu b\bar{b}$, and $VH \rightarrow \nu\nu b\bar{b}$ channels for $J^P = 0^-$ and $J^P = 2^+$ assuming $\mu = 1.0$. The LLR distribution assuming the test (null) hypothesis is shown in red (blue) while the observed LLR value is represented by the black vertical line. The green and yellow shaded bands represent 1 and 2 s.d. on the expectation from the null hypothesis, respectively.

CL with an expected exclusion of 99.94% CL. Assuming a signal strength of $\mu = 1.23$ the exclusion is stronger. We exclude the $J^P = 0^-$ ($J^P = 2^+$) case at the 99.5% (99.8%) CL with an expected exclusion of 99.98% (99.99%) CL.

By relaxing the constraint that $\mu = \mu_{J^P}$ we can explore the exclusion region as a function of both signal strengths. To do this we vary the $J^P = 0^+$ and non-SM J^P signal strengths independently and calculate the value of CL_s. If $CL_s \geq 0.95$ then the selected signal strengths are excluded. Figure 9.9 illustrates the expected exclusion region and the observed exclusion at 95% CL as functions of the SM μ_{0+} and non-SM μ_{J^P} signal strengths. Points in μ_{0+}-μ_{J^P} space are expected to be excluded at $\geq$ 95% CL if they fall in the shaded or hatched region. We exclude points which are above the observed 95% CL lines at $>$ 95% CL. The quoted exclusion for $\mu = 1.0$ corresponds to the point (1.0, 1.0) in this figure.

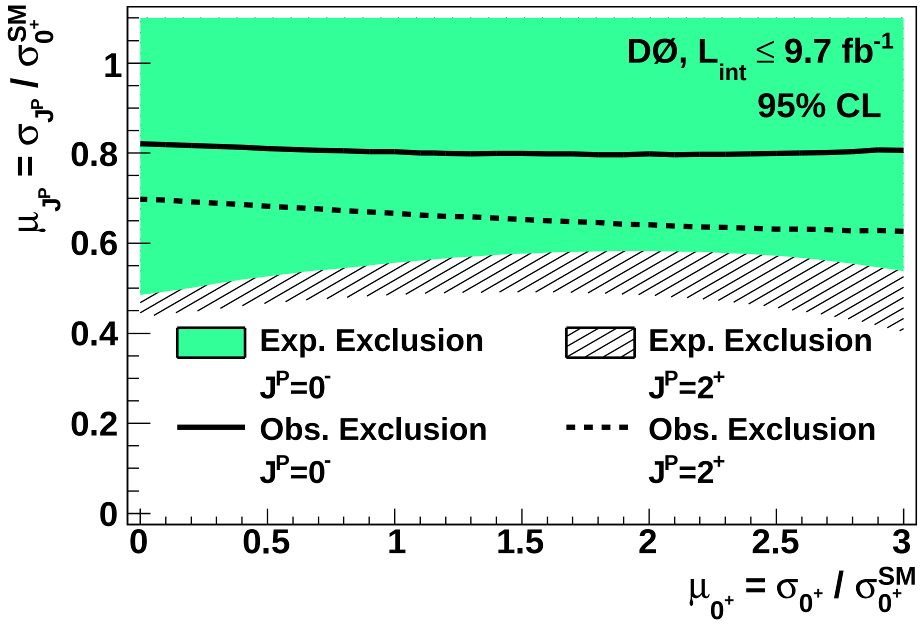

Figure 9.9: *D0 Observed and Expected Exclusion Regions, Pure J^P States*
The expected exclusion region (green shaded area) and observed exclusion (solid line) as functions of the $J^P = 0^-$ and $J^P = 0^+$ signal strengths. The hatched area corresponds to the expected exclusion region as a function of the $J^P = 2^+$ and $J^P = 0^+$ signal strengths. The dashed line is the corresponding observed exclusion.

Analysis	$ZH \to \ell\ell b\bar{b}$	$WH \to \ell\nu b\bar{b}$	$ZH \to \nu\nu b\bar{b}$	Combined
$J^P = 0^-$ vs. $J^P = 0^+$				
$p^{0^-}_{\text{test}}$ Expected	0.075	0.030	0.016	0.0007
$p^{0^-}_{\text{test}}$ Observed	0.126	0.351	0.007	0.022
$1 - p_{\text{null}}$ Expected	0.500	0.500	0.500	0.500
$1 - p_{\text{null}}$ Observed	0.646	0.965	0.367	0.918
CL_s Expected	0.850 (1.04 s.d.)	0.941 (1.56 s.d.)	0.969 (1.87 s.d.)	0.9986 (3.00 s.d.)
CL_s Observed	0.805 (0.86 s.d.)	0.637 (0.35 s.d.)	0.981 (2.07 s.d.)	0.976 (1.98 s.d.)
$J^P = 2^+$ vs. $J^P = 0^+$				
$p^{2^+}_{\text{test}}$ Expected	0.064	0.009	0.023	0.0003
$p^{2^+}_{\text{test}}$ Observed	0.134	0.114	0.002	0.009
$1 - p_{\text{null}}$ Expected	0.500	0.500	0.500	0.500
$1 - p_{\text{null}}$ Observed	0.702	0.932	0.173	0.906
CL_s Expected	0.872 (1.14 s.d.)	0.982 (2.09 s.d.)	0.953 (1.68 s.d.)	0.9994 (3.22 s.d.)
CL_s Observed	0.810 (0.88 s.d.)	0.878 (1.16 s.d.)	0.987 (2.23 s.d.)	0.990 (2.34 s.d.)

Table 9.4: *D0 Combination p-Values*
Expected and observed p-values and CL_s values for $J^P = 0^-$ and $J^P = 2^+$ VX associated production, assuming signal cross sections equal to the 125 GeV SM Higgs production cross section multiplied by $\mu = 1.0$.

9.4.2 D0 Combination Results: Admixtures of J^P States

For the D0 combination we can also consider the possibility that the data is described by an admixture of SM and non-SM J^P states. For this possibility we normalize the signals for each hypothesis as in Table 9.1. We fix the sum of the SM and non-SM J^P cross sections to a specific value of $\mu_{\text{tot}} \times \sigma^{\text{SM}}_{0^+}$ and vary the non-SM J^P signal fraction f_{J^P}. As previously, we choose values of $\mu_{\text{tot}} = 1.0$ and $\mu_{\text{tot}} = 1.23$ and proceed to calculate the value of CL_s. The observed and expected values of CL_s are plotted in Fig. 9.10 as a function of the non-SM J^P signal fraction for $\mu_{\text{tot}} = 1.0$. Fractions are excluded if the observed value is above the 95% CL. Assuming a total signal strength of $\mu_{\text{tot}} = 1.0$ we exclude non-SM J^P signal fractions greater than 0.80 for $J^P = 0^-$ and 0.67 for $J^P = 2^+$ at the 95% CL. The expected exclusions are 0.54 and 0.47, respectively. For an assumed value of $\mu_{\text{tot}} = 1.23$ the exclusions are stronger and are summarized in Table 9.5. The exclusion regions as functions of the non-SM J^P signal fraction f_{J^P} and the total signal strength μ_{tot} are illustrated in Fig. 9.11.

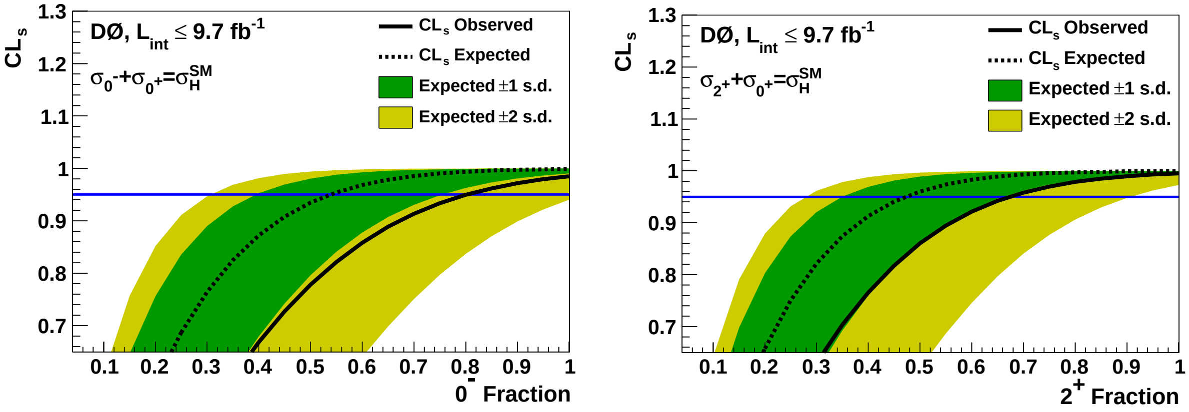

Figure 9.10: *CL_s as a Function of the Non-SM Signal Fraction*
Values of CL_s plotted as a function of the non-SM J^P signal fraction f_{J^P} assuming $\mu_{\text{tot}} = 1.0$. The observed (expected) value is represented by a solid (dotted) line. The green and yellow shaded bands correspond to 1 and 2 s.d. on the expectation of the null hypothesis. The blue horizontal line corresponds to the 95% CL.

9.4.3 Summary of D0 Results

The D0 combination of all three VX production channels increased the sensitivity of the spin-parity study dramatically when compared to the WX channel alone. Assuming a signal cross section multiplied by branching ratio consistent with measurements at both the Tevatron and the LHC we were able to strongly reject non-SM J^P predictions in favor of the SM prediction. The combination also allowed us to investigate signal admixtures and exclude some non-SM J^P signal fractions. The results are summarized in Table 9.5 for both $\mu = 1.0$ and $\mu = 1.23$. This result has been published and more details can be found in Ref. [65].

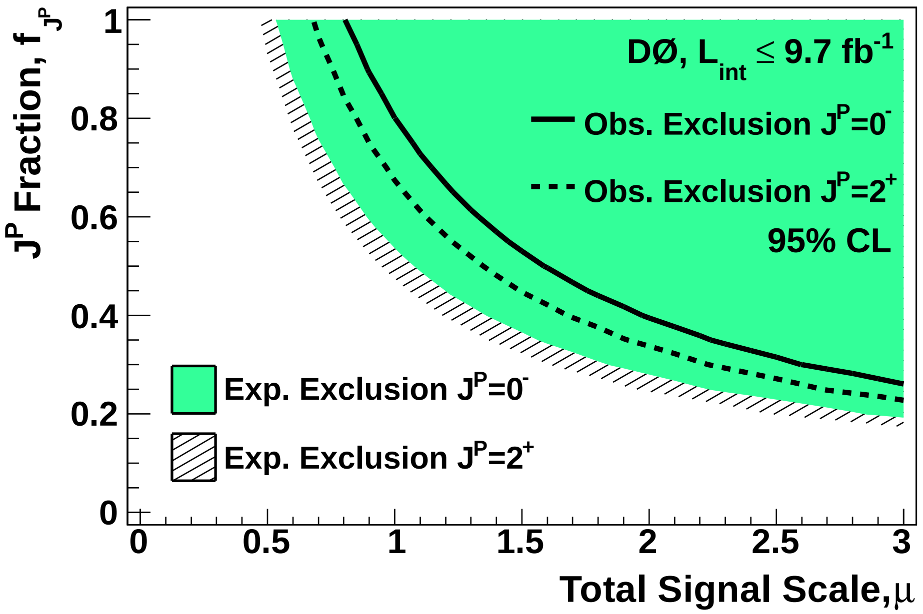

Figure 9.11: *D0 Observed and Expected Exclusion Regions, Admixtures*
The expected exclusion region (green shaded area) and observed exclusion (solid line) as functions of the $J^P = 0^-$ signal fraction and total signal strength. The hatched area corresponds to the expected exclusion region as a function of the $J^P = 2^+$ signal fraction and total signal strength. The dashed line is the corresponding observed exclusion.

J^P	CL_s (s.d.)		f_{J^P}	
$\mu = 1.0$	Exp.	Obs.	Exp.	Obs.
0^-	0.9986 (3.00)	0.976 (1.98)	>0.54	>0.80
2^+	0.9994 (3.22)	0.990 (2.34)	>0.47	>0.67
$\mu = 1.23$				
0^-	0.9998 (3.60)	0.995 (2.56)	>0.45	>0.67
2^+	0.9999 (3.86)	0.998 (2.91)	>0.40	>0.56

Table 9.5: *Expected and Observed CL_s Values*
Expected and observed CL_s values (converted to s.d. in parentheses) and signal fractions for $\mu = 1.0$ and $\mu = 1.23$ excluded at the 95% CL.

9.5 Tevatron Combination

The statistical combination of our results with those of a similar study[66] at the CDF experiment will increase the potential exclusion region. All three VX production channels were studied at the CDF experiment using the method suggested by [38]. The analysis method for the individual channels is similar to what was done at the D0 experiment and are briefly described in the following. All analyses use the same multivariate classifier to tag b quark jets. The classifier does not perform well on jets with $E_T > 200\,\mathrm{GeV}$ so b-tagging is not applied for these jets in all channels. For the spin-parity analysis a multivariate analysis (MVA) tool was trained to discriminate between the SM backgrounds and the non-SM J^P signal. Events that are classified as background are then classified using the MVA for the SM Higgs boson search in the $WH \to \ell\nu b\bar{b}$ and $VH \to \nu\nu b\bar{b}$ channels. Detailed descriptions of the SM Higgs boson searches on which the current analyses are based can be found in [67, 40, 68]. It is interesting to note that the CDF experiment reported 1 s.d. and 2 s.d. deficits in the signal regions for the $J^P = 0^-$ and $J^P = 2^+$ hypotheses, respectively. This is in contrast to the results of the D0 study which had a 2 s.d. excess. The combination of these results will have the effect of balancing the two extremes. The details of the Tevatron combination have been published and more information can be found in Ref. [69].

$ZH \to \ell\ell b\bar{b}$ Channel (CDF)

This channel requires two isolated leptons and at least two jets. The CDF analysis of this channel requires either two or three jets. Events are divided into b-tagging categories based on the output of a multivariate classifier. For the $ZH \to \ell\ell b\bar{b}$ channel they use three double-b-tag categories and one single-b-tag category.

$WH \to \ell\nu b\bar{b}$ Channel (CDF)

CDF requires one lepton (e or μ), exactly two jets, and significant $\not{E}_T$. Events are classified according to the quality of the selected lepton. These are high-quality leptons in the central detector, leptons based on isolated tracks, and electrons in the forward region. They define five b-tagging categories: three double-b-tag categories and two single-b-tag categories.

$VH \rightarrow \nu\nu b\bar{b}$ Channel (CDF)

The $VH \rightarrow \nu\nu b\bar{b}$ channel selects events with large $\not{E}_T$ and two or three jets. The jets are divided into two double-b-tag categories and one single-b-tag category. This analysis is also sensitive to $WH \rightarrow \ell\nu b\bar{b}$ production where the lepton is not identified.

9.5.1 Tevatron Combination Results: Pure Non-SM J^P States

For the Tevatron combination we first assume a pure non-SM J^Pstate and again calculate the value of CL_s assuming $\mu = 1.0$. The LLR distributions for $J^P = 0^-$ and $J^P = 2^+$ are shown in Fig. 9.12. The calculated $1 - CL_s$ values are presented in Table 9.6. We exclude models with non-SM J^P signals with significances of 5.0 s.d. and 4.9 s.d. for the $J^P = 0^-$ and $J^P = 2^+$ hypotheses, respectively. The expected significances for the $J^P = 0^-$ and $J^P = 2^+$ hypotheses are 4.8 s.d. and 4.6 s.d. In the Tevatron combination the observed significances are higher than expected. This effect is driven by a deficit in the observed number of events in a region with high non-SM J^P signal content for the CDF analyses. The largest contribution comes from the $WX \rightarrow \ell\nu b\bar{b}$ channel.

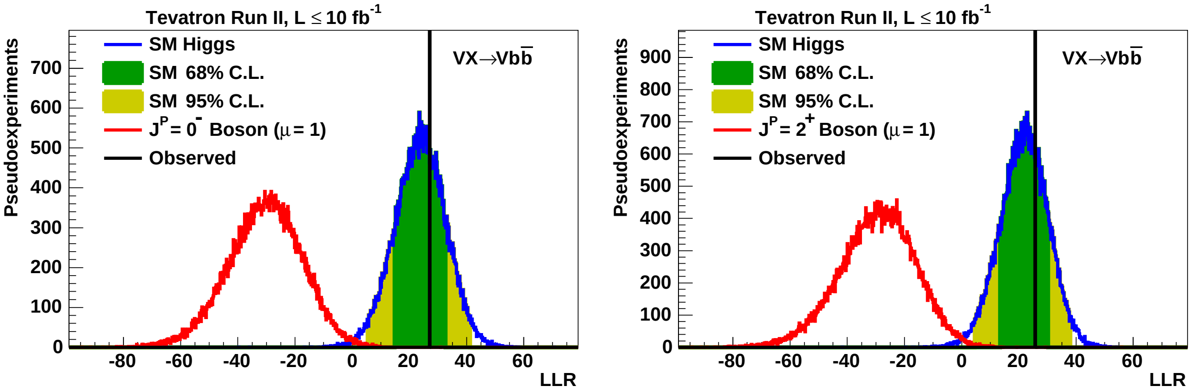

Figure 9.12: *LLR Distributions for the Tevatron Combination*
LLR distributions for the Tevatron combination of the VX production channels for $J^P = 0^-$ and $J^P = 2^+$ assuming $\mu = 1.0$. The LLR distribution assuming the test (null) hypothesis is shown in red (blue) while the observed LLR value is represented by the black vertical line. The green and yellow shaded bands represent 1 and 2 s.d. on the expectation from the null hypothesis, respectively.

Analysis	$J^P = 0^-$	$J^P = 2^+$
$1 - CL_s$ Expected	$9.4{\times}10^{-7}$ (4.8 s.d.)	$2.3{\times}10^{-6}$ (4.6 s.d.)
$1 - CL_s$ Observed	$2.6{\times}10^{-7}$ (5.0 s.d.)	$5.6{\times}10^{-7}$ (4.9 s.d.)

Table 9.6: *Tevatron* $1 - CL_s$ *Values*
$1 - CL_s$ values for $J^P = 0^-$ and $J^P = 2^+$ WX associated production, assuming signal cross sections equal to the 125 GeV SM Higgs production cross section multiplied by $\mu = 1.0$.

9.5.2 Tevatron Combination Results: Admixtures of J^P States

The Tevatron combination also considers the possibility of signal admixtures. We explore the exclusion regions as functions of the non-SM J^P signal fraction and the total signal strength. Figure 9.13 illustrates these regions. Note that meanings of the shaded and hatched regions are reversed when compared to the same plot in the D0 combination. The overall shape of the exclusion region is similar to the region defined by D0 but extends the range considerably.

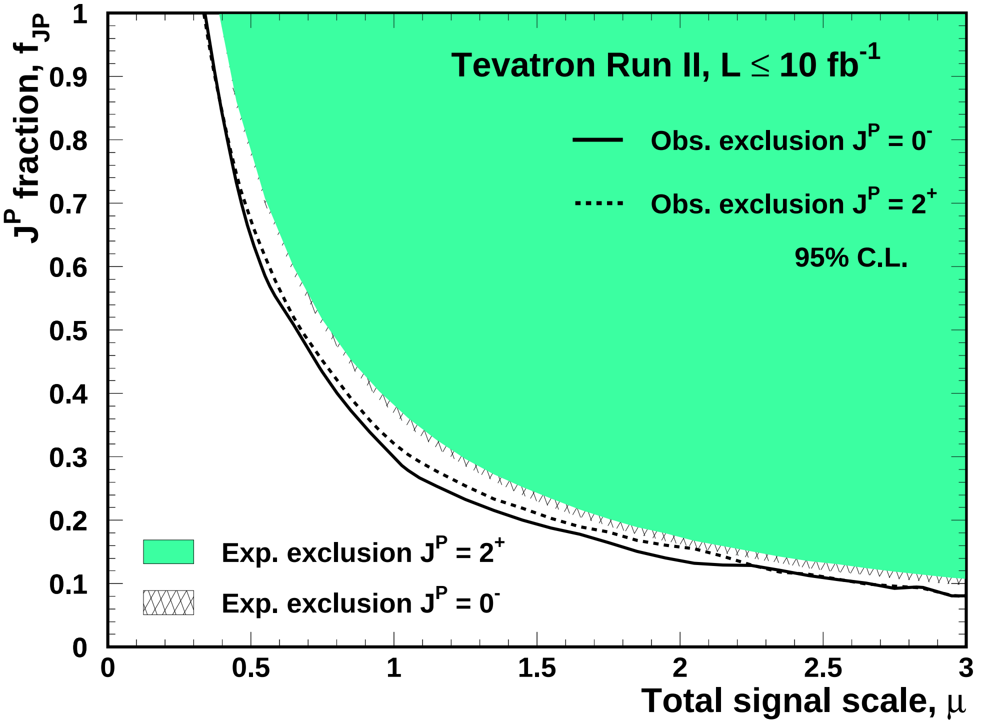

Figure 9.13: *Tevatron Observed and Expected Exclusion Regions, Admixtures*
The expected exclusion region (green shaded area) and observed exclusion (solid line) as functions of the $J^P = 2^+$ signal fraction and total signal strength. The hatched area corresponds to the expected exclusion region as a function of the $J^P = 0^-$ signal fraction and total signal strength. The dashed line is the corresponding observed exclusion.

Chapter 10

Conclusion

Beginning with the recommendation of Ref. [38] to study the J^P character of the excess observed at the Tevatron we were able to exclude models for the Higgs boson with exotic spin and parity with high significance. We studied WH production where the W boson decays leptonically and the Higgs boson decays to a pair of b quarks in detail. Using the transverse mass of the WH system as a discrimination tool we investigated two well-motivated J^P states: $J^P = 0^-$ and $J^P = 2^+$. Assuming that the signal cross sections were equal to the 125 GeV SM Higgs boson production cross section multiplied by $\mu = 1.0$ we found that we could not exclude these possibilities at the 95% CL. By combining the other vector boson associated production channels at D0 we were able to exclude the $J^P = 0^-$ and $J^P = 2^+$ hypotheses at the 97.6% CL and 99.0% CL, respectively. We considered the possibility that the data is described by an admixture of SM and non-SM J^P states. We were able to exclude $J^P = 0^-$ signal fractions $f_{0^-} > 0.80$ and $J^P = 2^+$ signal fractions $f_{2^+} > 0.67$ at the 95% CL. We also combined our results with the results of the CDF experiment. The $J^P = 0^-$ and $J^P = 2^+$ hypotheses are excluded with significances of 5.0 s.d. and 4.9 s.d., respectively. The corresponding confidence levels are $> 99.9999\%$. At the time of this writing, these production channels are not accessible to the experiments at the LHC because of the relatively low signal-to-background ratio. These results are the most stringent exclusions of models for the Higgs boson with exotic spin and parity in a fermionic Higgs boson decay channel and will remain so until the LHC acquires the necessary sensitivity.

APPENDICES

Appendix A

The Fermilab Accelerator Chain

This Appendix provides more detail on the equipment used to accelerate protons and antiprotons and produce collisions. The Fermilab accelerator chain is described in detail by following the different paths taken by a proton and an antiproton beginning with their production and ending with their collision at a center of mass energy of 1.96 TeV.

Although the Fermilab accelerator chain has gone through many upgrades throughout the years (and still continues to do so!), the following sections describe the accelerator chain at the time it ceased to operate as a colliding beam facility. Section A.1 describes the path of a proton from the source to the final stage of acceleration. The creation, collection, and acceleration of antiprotons is described in Section A.3.

A.1 Life of a Proton

A.1.1 The Preaccelerator

All protons at Fermilab begin in a bottle of hydrogen gas at one of two preaccelerators. There are two for redundancy and can be considered identical for the purpose of this Thesis. Each preaccelerator consists of a negative hydrogen ion source, a Cockcroft-Walton voltage generator, an electrostatic accelerating column, and a transport line for injection into the Linac.

To begin, hydrogen gas is pumped into a surface plasma magnetron source. The magnetron source, Fig. A.1, consists of a oval shaped cathode surrounded by an anode and placed in a magnetic field parallel to the cathode surface. The anode and cathode are energized with a few hundred volts and hydrogen gas is pumped into the space between the anode and cathode. The electric and magnetic fields cause the confined electrons to spiral in the gap between the anode and the cathode, producing a dense plasma. Negative ions are produced when positive ions are attracted to, and strike, the surface of the cathode and either sputter off negative ions or gain electrons themselves. To decrease the energy required to pull electrons from the cathode surface, cesium vapor is leaked into the system and coats the cathode with a very thin layer. Once produced, these negative ions accelerate from the cathode through the narrow plasma to the anode. When negative ions are near a slit in the anode – the anode aperture – they are accelerated by an extractor electrode to approximately 18 keV. To separate the negative hydrogen ions from other negative species a 90° bending magnet is used and guides the hydrogen ions to the first stage of acceleration, the accelerating column.

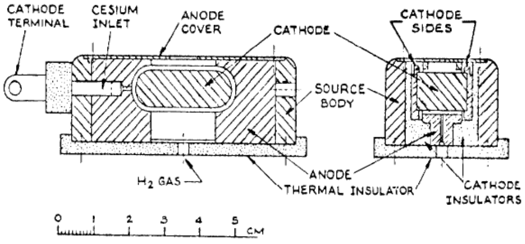

Figure A.1: *Surface Plasma Magnetron Source*
Diagram of a surface plasma magnetron source like those used at Fermilab.

The Fermilab accelerating column is an electrostatic accelerator. The high voltage difference required for the acceleration is provided by a dual-leg, five stage Cockcroft-Walton generator. The Cockcroft-Walton generator is described in Section 2.1.1. A second leg reduces ripple in the output voltage. The Cockcroft-Walton provides a high voltage of -750 kV from a source voltage of 75 kV. The accelerating column and source installment is shown in Fig. A.2. The accelerating column consists of seven disk-shaped titanium electrodes designed to guide the ions during their acceleration. They are separated with ceramic insulating disks and the inside is kept at vacuum. The entire column is placed inside a pressurized glass vessel containing the insulating gas sulfur hexafluoride to minimize sparks between the electrode leads. The high voltage is distributed among the electrodes via a water resistor so the voltage drop between electrodes is roughly equal. The end of the electrostatic column is grounded at the wall of the enclosure. Referring to Eq. 2.2 and considering the charge of the negative hydrogen ion is equal to that of an electron, the ions are accelerated to 750 keV. The source operates in pulsed mode with a rate of 15 Hz both to preserve the integrity of the source and to match the fixed cycle time of the Booster. A pulse lasts approximately 80 μs. Between the accelerating column and the Linac is a transfer line, the 750 keV line, that serves several functions: focusing, selecting, and bunching. Each transfer line has several horizontal and vertical focusing quadrupoles to keep the beam from being dispersed.

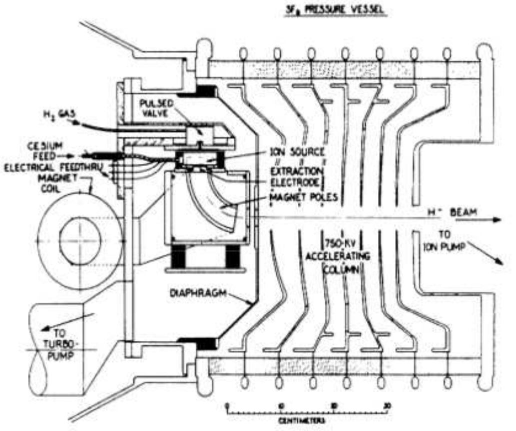

Figure A.2: *Proton Source and Accelerating Column*
Fermilab source and accelerating column assembly.

A device called the *chopper* selects a portion of the beam, usually approximately 40 μs, to send to the Linac. Bunching the beam increases the capture efficiency of the Linac. If a continuous particle beam were injected into the Linac only the particles in the stable phase region would be captured and accelerated which would amount to 35% of the pulse. The buncher is a single-gap radio frequency cavity similar to the cavities in the Linac. It operates at the same frequency as the Linac but with a different phase. Particles that arrive early are decelerated and particles that arrive late are accelerated. This effectively decreases the particles' width in time but increases the particles' momentum spread. With the buncher, the Linac capture rate is approximately 70%.

A.1.2 The Linac

The Fermilab Linac is composed of two different machines that work in tandem to accelerate the beam to 400 MeV. The first machine is an Alvarez drift tube linac (DTL). It consists of five cylindrical oxygen-free high conductivity (OFHC) copper clad steel tanks. Each tank is powered by its own 5 MW power source and resonates at 201.24 MHz. Each cavity has several resonant cells extending from the center of one drift tube to the next with the cell length ranging in length from 6.04 cm to 67.9 cm. The phase shift between adjacent accelerating cells is zero and each radio frequency (RF) bucket contains a particle bunch. The average axial electric field ranges from 1.6 MV/m to 2.6 MV/m. This portion of the Linac accelerates the negative hydrogen ions to 116 MeV.

After acceleration in the DTL the H^- ions move into the second portion of the Linac, the side-coupled linac (SCL). Instead of one cavity containing multiple accelerating cells as in the DTL, each cavity is one cell in the SCL. The SCL consists of seven modules which are divided into four sections with sixteen accelerating cells and fifteen coupling cells. Each cell has a $\pi/2$ phase shift from each adjacent cell, giving a phase shift of π between accelerating cells. Individual modules are powered with a single 12 MW power source and resonate at 804.96 MHz. Because the driving frequency is four times that of the DTL and the phase shift between accelerating cells is different by π, the bunches travel eight accelerating cells apart in the SCL. The power is distributed from one independent accelerating cell to the next through the coupling cells. An analogous system would be a set of masses connected in series with springs. If one mass is set to oscillate the others will come to oscillate at the same frequency through the coupling of the springs. An example section of a side-coupled linac is shown in Fig. A.3. In addition to coupling cavities, each section is connected via a bridge coupler that is the length of three coupling cells. This allows for the placement of focusing quadrupoles and beam diagnostics. The RF power is imported at the middle bridge coupler to equalize the power droop at either end.

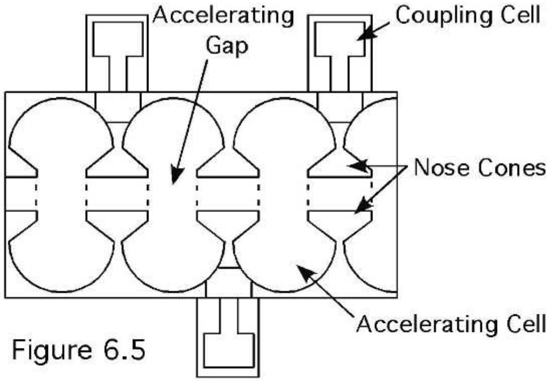

Figure A.3: *Side-Coupled Linac Section*
An example section of a side-coupled linac.

One of the main benefits of the SCL is the nose-cone shape of the accelerating cavities. Figure A.4 shows the electric field in the accelerating cavity due to the nose-cones. The electric field is highly concentrated in the center of the accelerating gap which produces a more efficient acceleration. The average axial field in each module is approximately 7.5 MV/m, about three times that of the DTL. After the 66 ms Linac cycle the beam has an energy of 400 MeV.

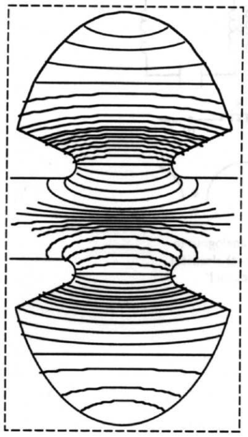

Figure A.4: *Nose-Cone Field*
The electric field of a nose-cone. Notice the concentrated field in the center of the accelerating region.

Between the Linac and the Booster is a transfer line, the 400 MeV line, that that has a similar function to the line between the Preaccelerator and the Linac. A portion of the pulse, the *chop*, from the Linac is selected to be sent to the Booster. The length determines the resulting intensity of the beam in the Booster. A cartoon of the chopping process is shown in Fig. A.5. First, the plates of the chopper are charged up to approximately 60 kV and beam goes through undeflected. It travels through the center of a focusing (in the horizontal direction) quadrupole and straight through the Lambertson septum magnet towards the beam dump. At the start of the chop the lower plate is grounded and the beam is deflected upwards. It enters the quadrupole off-center and gets further deflected into the field region of the Lambertson. The Lambertson gives the beam a horizontal bend of approximately 11°. At the end of the chop the top chopper plate is grounded and the remaining beam is again undeflected and is sent to the beam dump. After the chop is selected it is sent down fifteen feet to the Booster at an angle of approximately 13°. After being kicked out of the SCL,

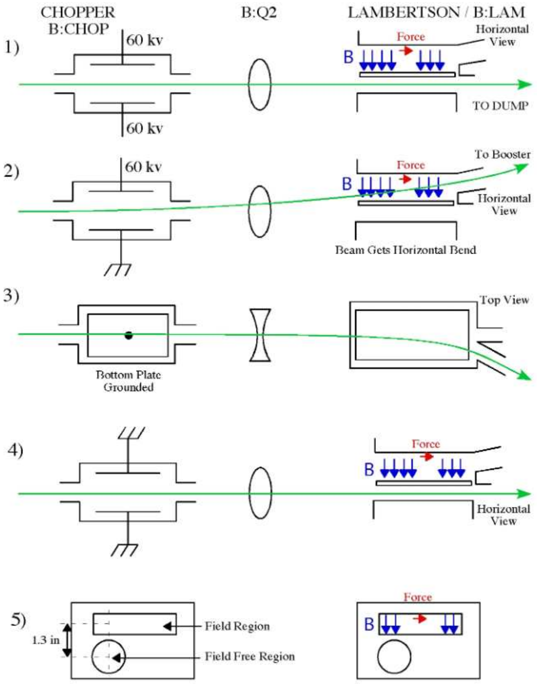

Figure A.5: *400 MeV Chopper*
Cartoon of the chopper section in the 400 MeV line from the Linac to the Booster.

the beam passes through a debuncher which helps remove the 804.96 MHz RF structure from the SCL and reduce the momentum spread in the beam. In addition to focusing and steering magnets, the 400 MeV line must also match the lattice of the SCL to the lattice of the Booster for efficient transfer.

A.1.3 The Booster

The Booster is the first in a series of three synchrotrons in the Fermilab accelerator chain. It is a fast-cycling machine that completes a cycle from injection to extraction in roughly 66 ms. It has a circumference of 468 m and consists of 96 combined function magnets arranged in a *FOFDOOD* lattice: focusing quadrupole, short drift length, focusing quadrupole, defocusing quadrupole, long drift length, and another defocusing quadrupole. It has seventeen accelerating cavities located in the long drift sections.

At the injection energy of 400 MeV one turn in the Booster takes 2.22 μs. With a chop length of approximately 40 μs, the beam from the Linac could wrap around the Booster eighteen times! It is here that the benefit of starting with negative hydrogen ions is apparent. If the source produced protons it would only be possible to fill up one turn of the Booster. In this way the intensity of the beam is limited and a large amount of beam is wasted. A clever route was taken to solve this problem and is shown in Fig. A.6. Upon injection, the circulating protons are bumped from their nominal orbit and sent with the negative hydrogen ions through a stripping foil which removes electrons from the negative ions. After going through the stripping foil the beam is sent back to its nominal orbit with newly acquired protons. The negative and neutral products are absorbed. In normal operation the Booster is able to accept five turns of beam from the Linac.

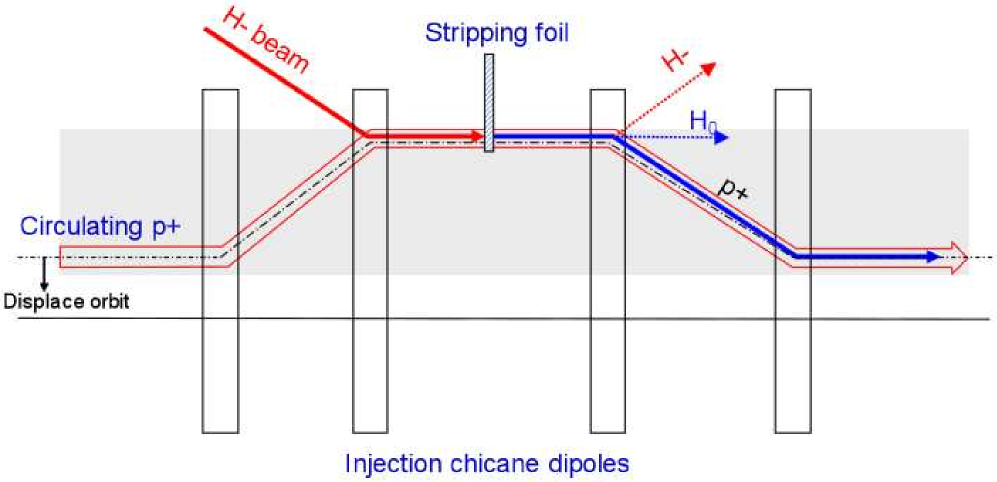

Figure A.6: *Charge Exchange Injection*
Two sets of dipole magnets produce a bump in the orbit of the circulating protons and injected negative hydrogen ions which puts them in the path of a stripping foil which removes electrons.

After the beam has been injected and the RF structure of the Linac has decayed away, the beam is captured by the Booster's 38 MHZ RF system into 84 RF buckets. Early in the cycle, the last three bunches in the bunch train are ejected and the corresponding buckets cleared to allow time for the ejection kicker magnets to turn on. During acceleration, the RF frequency increases from 37.8 MHz to 52.8 MHz to match the increasing kinetic energy of the beam. At the end of the acceleration cycle the protons have a kinetic energy of 8 GeV and are ready to be delivered to the Main Injector.

The 8 GeV transfer line between the Booster and the Main Injector must steer the beam down 11 feet to the level of the Main Injector and around obstacles (such as the Antiproton Source) all while maintaining horizontal and vertical focus. Because the transfer line has its own lattice structure, there are two lattice matches that need to be done before injection into the Main Injector: matching the Booster lattice to the transfer line lattice and matching the transfer line lattice to the Main Injector lattice. Because the extraction frequency of the Booster and the injection frequency of the Main Injector are equal, the Booster phase-locks with the Main Injector and performs a bucket-to-bucket transfer of beam.

A.2 The Main Injector

The Main Injector is the second synchrotron and is the real workhorse of the Fermilab accelerator chain. It serves many functions in the accelerator chain; delivering protons and antiprotons to the Tevatron for acceleration, delivering protons to the Antiproton Source, transferring antiprotons to and from the Accumulator and Recycler, and delivering beam to fixed target and neutrino experiments. The Main Injector has a circumference of 3319 m and is composed of 344 dipole and 208 quadrupole magnets arranged in a *FODO* lattice with most of the dipoles placed in the drift (O) spaces. It is capable of accelerating protons and antiprotons up to 150 GeV. It has eighteen RF cavities operating from 52.8 MHz to 53.1 MHz divided into two independent systems. This is required for *slip-stacking*, a method of increasing the intensity of the beam that involves letting two Booster batches with slightly different RF (and hence momentum) slip past each other in the ring until they are aligned and then recapturing the bunches in a single RF bucket. The Main Injector can also coalesce proton and antiproton bunches by rotating several bunches via synchrotron oscillations in a 2.5 MHz RF bucket and then recapturing them in a 53 MHz bucket. A partial batch from Booster of approximately seven bunches are passed to Main Injector and accelerated to 150 GeV when they are coalesced into a single bunch and injected into the Tevatron. A total of 36 of these super bunches are injected into the Tevatron for collisions.

A.2.1 The Tevatron

The Tevatron is the third synchrotron and final accelerator in the chain. It is a superconducting synchrotron that is 6.3 km in circumference. Over a thousand superconducting magnets cooled to liquid helium temperatures make up the *FODO* lattice of the Tevatron. Unlike the other machines which serve a variety of purposes throughout the complex, the Tevatron has one mode of operation: collider mode. Its job is to accelerate counter-rotating protons and antiprotons to their final energy of 980 GeV and then collide them at two fixed points around the ring. Once the acceleration is complete, it functions as a storage ring where stable beams collide for hours on end. There are eight accelerating cavities which resonate from 53.103 MHz to 53.104 MHz during acceleration. The acceleration of both protons and antiprotons in this machine requires two independent RF systems to allow for fine control over the relative positions of the beams. The eight accelerating cavities are divided into two groups: one that accelerates the protons and one that accelerates the antiprotons. The Tevatron now has 36 coalesced bunches of protons circulating at the injection energy of 150 GeV. We will return to the Tevatron later when discussing antiprotons.

A.3 Life of an Antiproton

Antiprotons are more difficult to make and many aspects of the accelerator chain reflect this. To get an idea of how difficult it is to produce antiprotons consider that for every 10^5 protons that bombard the target only about *two* antiprotons are produced. The Fermilab Antiproton Source consists of the Target Vault, two triangular synchrotrons: the Debuncher and the Accumulator, and a permanent-magnet storage ring called the Recycler. The Main Injector and the Tevatron are also directly involved in the acceleration and transport of the antiprotons. To begin, Booster sends two batches of protons to Main Injector where they are slip-stacked and accelerated to 120 GeV. Main Injector then rotates the bunches in longitudinal phase space, creating bunches which have a large momentum spread but a small spread in time. The bunches are then extracted from the Main Injector and sent to the Target Vault.

A.3.1 Target Vault

Upstream of the target is a *sweeper magnet*, a rotating dipole which deflects the proton beam in a circle to reduce heating of the target. The protons impinge on an Inconel (a nickel-iron alloy) target which produces a spray of secondary particles some of which are antiprotons. The target is cylindrical in shape and rotates on an axis perpendicular to the incoming beam to reduce target heating and degradation. Immediately after the target is a lithium lens which focuses the secondaries in both transverse planes. Lithium is used because it is the least dense solid conductor; scattering and absorption of the rare antiprotons is minimized. A copper collimator with a hole bored in the center for the beam to travel through protects the next element, a pulsed dipole magnet. This magnet selects negatively-charged 8 GeV secondaries and sends them to the Debuncher.

A.3.2 The Debuncher

The Debuncher is a rounded triangle synchrotron with a traditional *FODO* lattice. It operates at a fixed energy of 8 GeV, the peak energy of the Booster and close to the antiproton production peak. As the name implies, its function is to debunch the incoming antiprotons. During the transit from the Target Vault most of the secondaries that were not antiprotons decayed away and the rest will be lost during the first few trips around the Debuncher. The antiprotons that are left have retained the bunch structure of the protons that left the Main Injector. The main RF system in the Debuncher is a 53.1 MHz system that is responsible for rotating the beam of antiprotons in longitudinal phase space to recreate bunches that have a large spread in time and a small momentum spread. It is also responsible for debunching the beam. A secondary RF system maintains a gap between the head and tail of the bunch train so the train fits around the smaller Accumulator ring. The Debuncher uses *stochastic cooling* of the beam to decrease the transverse and longitudinal emittance resulting in a denser particle beam. Stochastic cooling uses sets of pick-ups and kickers to detect and correct errors in the beam energy and transverse displacement.

A.3.3 The Accumulator

The Accumulator is an 8 GeV fixed-energy synchrotron in the shape of a triangle with flattened corners. It lies on the inside radius in the same tunnel as the Debuncher and has a similar *FODO* lattice. The Accumulator collects successive antiproton batches from the Debuncher over several hours. It performs *momentum stacking* where newly injected beam is cooled and decelerated towards a core momentum value. Figure A.7 shows the radial distribution of antiprotons, collectively called the *stack*, in the Accumulator. Antiprotons of lower energy occupy a smaller radius in the machine. There is a difference in energy of 150 MeV from the stack core to the injection orbit. This is accomplished in the Accumulator first through RF manipulations and then through stochastic cooling. Beam from the Debuncher is a continuous ribbon and is captured into 53 MHz buckets and decelerated 60 MeV and deposited at the edge of the stack tail. The RF voltage is lowered slowly to allow the beam to debunch. Stack tail cooling systems are momentum cooling systems with pick-ups

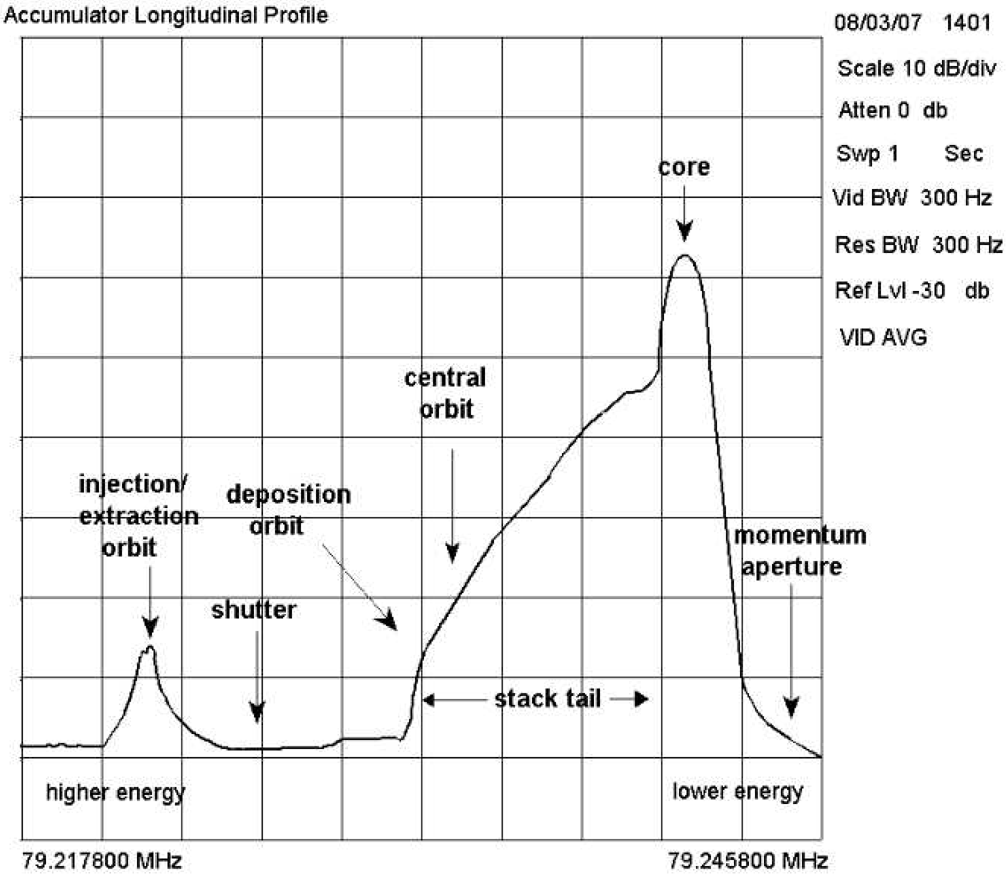

Figure A.7: *Accumulator Stack Profile*
Radial antiproton distribution in the Accumulator. Particles on the right in the diagram are lower in momentum and have a smaller orbital radius.

in high dispersion sections. These cooling systems decelerate the beam to the core region in approximately twenty minutes. Once in the core region, momentum cooling systems keep the beam contained in the core by decelerating higher momentum particles and accelerating lower momentum particles to keep them inside the machine. Transverse cooling pickups for the core are located in low dispersion sections and are used to control the transverse emittance.

Once a stack of suitable intensity is reached, part of the core is extracted from the Accumulator and transferred to the Recycler by the Main Injector. A 2.52 MHz RF system creates four bunches from the core and slowly accelerates them through the rest of the stack and all the way to the extraction orbit. They are then kicked out of the Accumulator without disturbing the rest of the stack and transferred by the Main Injector to the Recycler.

A.3.4 The Recycler

The Recycler is an 8 GeV storage ring. It consists of permanent combined function magnets arranged in a *FODO* lattice. It resides above the Main Injector in the same tunnel. Like the Accumulator its job is to accumulate and store antiprotons. It accepts several batches of antiprotons from the Accumulator and is capable of storing them for hours. In the Recycler the accumulated antiprotons are referred to as the *stash* to differentiate from the Accumulator's *stack*.

Like the Accumulator and Debuncher, the Recycler uses stochastic cooling to control both the transverse and longitudinal emittance. Unlike these machines, the Recycler also uses electron cooling to decrease the momentum spread. In this scheme an electron gun produces a highly collimated and nearly monochromatic electron beam which is accelerated to match the average velocity of the circulating antiprotons. This electron beam is then allowed to travel alongside the antiproton beam for a short distance. Along the way, energy from the 'hot' antiprotons is transferred to the 'cold' electrons. The electrons are then returned to the source taking the energy gained with them.

So far we've seen beam stored in two different ways: in bunches or in a continuous ribbon. The Recycler stores its beam in a different manner. Instead of using a resonant RF cavity it uses a wide-band RF cavity that is capable of producing a multitude of (non-resonant) waveforms. The most used waveform in the Recycler is a rectangular pulse. Beam is stored longitudinally between a negative and a positive voltage pulse called a *barrier bucket*. All other manipulations of the beam are done using additional rectangular pulses. During injection, the four bunches of antiprotons from the Main Injector are captured by a 2.5 MHz sinusoidal waveform which is contained inside a barrier bucket. The gain on the waveform is reduced and the beam is allowed to debunch inside the barrier bucket. This barrier bucket is then moved towards the stash and the barriers between them are removed. When the Recycler intensity is great enough and the Tevatron is ready to start a new store the antiprotons are longitudinally 'momentum-mined'. Another set of RF manipulations creates nine parcels of low momentum spread. These parcels are moved one by one to the extraction region where they are made into four bunches and sent to the Main Injector for acceleration.

A.3.5 The Main Injector: An Antiproton's Point of View

After injecting 36 coalesced proton bunches into the Tevatron one at a time, Main Injector can begin accepting antiprotons from the Recycler. Because antiprotons have the same mass but opposite charge as the protons, the lattice of the Main Injector also works to accelerate antiprotons as long as their direction of travel is opposite that of the protons.[1] The Main Injector accepts four bunches from the Recycler equal to one parcel or 1/9 of the stash. It accelerates these four bunches to 150 GeV and deposits them in the Tevatron. To accept another four bunches from the Recycler it returns back to 8 GeV. Nine of these transfers are made for a total of 36 antiproton bunches.

A.3.6 The Tevatron: An Antiproton's Point of View

Once all 36 proton bunches are loaded satisfactorily, the Tevatron prepares to receive antiprotons from the Main Injector. To minimize the effects of having two separate beams in the same beam pipe electrostatic separators are turned on giving a kick to the protons in both transverse planes. This causes the protons to perform betatron oscillations around the ideal path resulting in a spiral path. When antiprotons are injected, they feel an equal and opposite force and also follow a spiral trajectory. The result looks like a double helix. Once 36 bunches of antiprotons are in the machine they are accelerated to 980 GeV. Next, the helical displacement is removed near the collision points and beam is squeezed into a small cross-sectional area for collisions. After unbound particles which can damage sensitive material in the detectors are removed, a *store* is declared and physics data-taking begins. The store lasts for hours and ends when the luminosity has fallen below a predetermined value and/or the Recycler has accumulated a large enough stash to begin another store.

---

[1] In Main Injector's case, protons travel counterclockwise and antiprotons travel clockwise. This is *opposite* to the rotational sense in the Tevatron.

Appendix B

The D0 Detector in Detail

This Appendix describes the D0 detector in greater detail than what was presented in the main text. For reference, the cross-sectional view of the D0 detector from Chapter 4 is reproduced here.

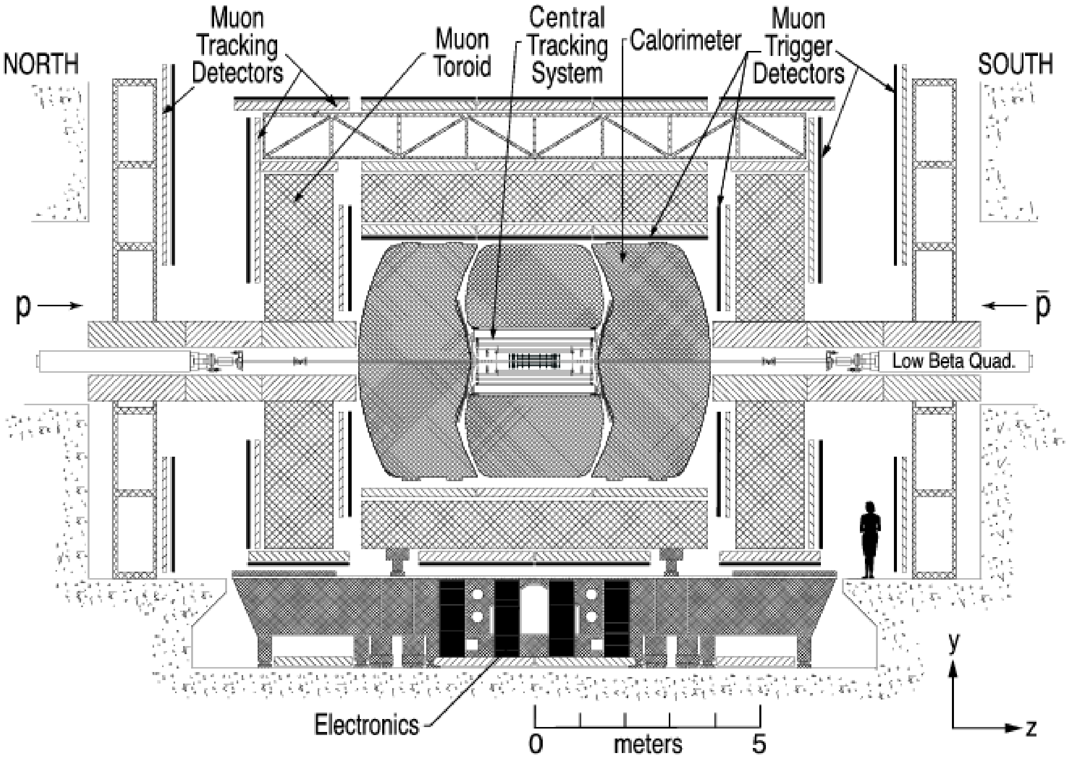

Figure B.1: *D0 Detector*
Cutaway view of the D0 detector showing the onion skin layering of the detector subcomponents.

B.1 Tracking System

The primary purpose of the tracking system is to record the tracks left by charged particles originating from the collisions of the proton and antiproton beams. Much information can be gained about the collision event from these recorded tracks. Placing the tracking volume inside the magnetic field of a solenoid makes additional measurements possible. Three important functions of the tracking system are based on the information provided by the recorded tracks. One such important function of the tracking system is *vertexing*. By extrapolating tracks back towards the beam, the primary interaction vertex for the event can be found with good precision. Secondary vertices caused by long-lived particles traveling a short distance before decaying can also be detected. This plays a major role in detecting long-lived b quark hadrons. Another important function is *particle identification*. Tracks can be matched to particle showers seen in the calorimeters to help determine the particle type. Determining the direction of curvature of the particle's trajectory in the magnetic field gives a measurement of the sign of its charge. The final function of the tracking system is obtaining a *momentum measurement* of the particles traversing the detector. This is done by measuring the curvature of the track in the magnetic field.

Many of these functions, particularly momentum measurements and vertexing, require the tracking system to be the closest detector subsystem to the interaction point. Directly outside the beam pipe, it occupies the radial space between 1.6 cm and 52 cm from the center of the beam pipe and is 2.5 m in extent. Since the direction and position of these tracks is important in reconstructing the collision event, care must be taken to minimize scattering of the particles off active detector material and support structures. Particles passing through the tracking system should not lose any appreciable amount of energy or be diverted from their original path. The tracking system consists of low atomic number Z materials to minimize the number of radiation lengths.

The tracking system consists of two detectors: the Silicon Microstrip Tracker and the Central Fiber Tracker described in Section B.1.2 and Section B.1.3, respectively. Because the magnet system is an essential part of the tracking system it will be described in Section B.1.1.

B.1.1 Magnets

The magnetic field which aids in tracking particles is provided by the combination of two magnets: a solenoid and a toroid. The entire tracking system is inside the bore of the solenoid magnet oriented parallel to the beam axis. The solenoid magnet along with the rest of the detector (with the exception of some of the muon system) is inside the toroid magnet. The central field of the solenoid is 2 T while the field in the toroid is 1.9 T. A projection of the resulting magnetic field in the y-z plane is shown in Fig. B.2. The magnetic field is symmetric about the x-z diagonal. The magnets' polarity is periodically reversed and data is taken in each of the four configurations.

B.1.1.1 Solenoid

The solenoid is a superconducting magnet that is 2.54 m long and 1.22 m in diameter. The superconducting cables are made from eighteen Cu:NbTi strands stabilized in aluminum. The cables are wound in two layers inside a supporting cylinder. The cables are cooled with liquid helium and operate in the superconducting regime. A current of 4749 A through the coils gives a central field of 2 T.

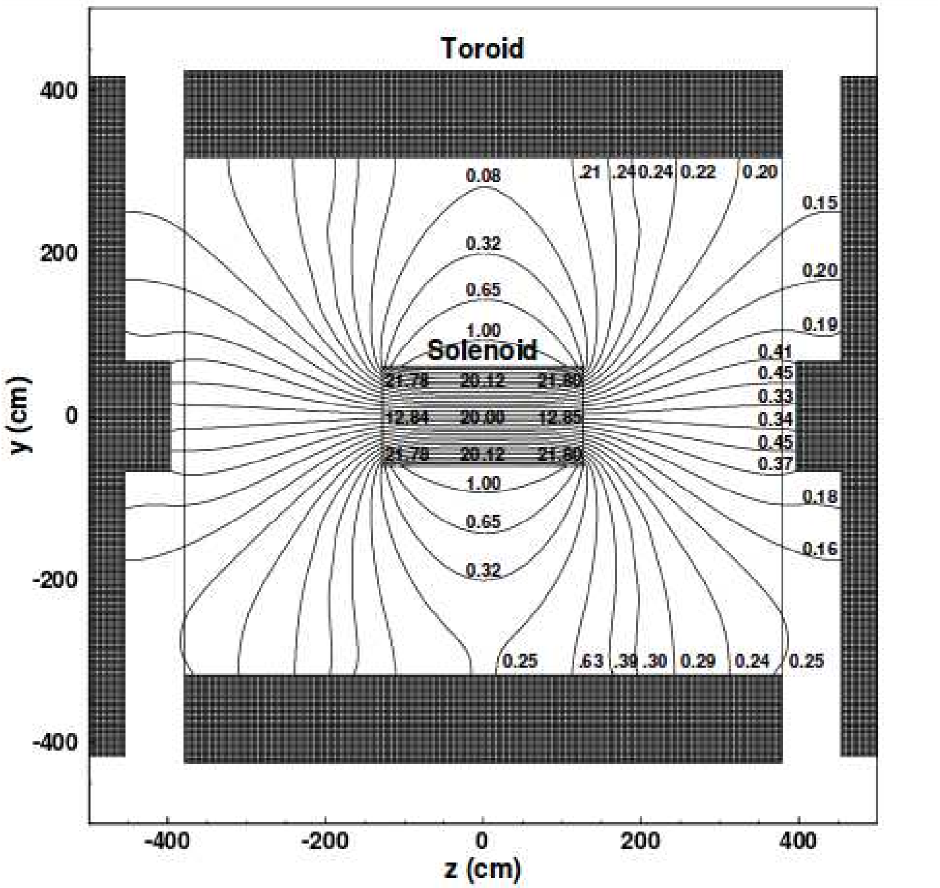

Figure B.2: *D0 Magnetic Field*
Plotted is the projection of the magnetic field in the y-z plane with the solenoid and toroid at full current. Note that the magnetic field possesses x-z symmetry; field lines at the points (y, $\pm z$) differ by as much as 2.5 m in x. Values are given in units of kilogauss (kG).

B.1.1.2 Toroid

The toroid is considered part of the muon system discussed in Section B.4 and also serves as the return for some of the field lines of the solenoid. Unlike the solenoid, the toroid operates in the classical regime. The magnet is made from iron windings around a steel yoke and has three sections: two end toroids and one central toroid. The central toroid is a square annulus about 1 m thick and 7.6 m long. It is wound with twenty coils of ten turns each. The two end toroids are square with a 1.8 m square hole to accommodate the beam line. Each end toroid is wound with eight coils of eight turns each and is wired in series with the central toroid. The current through the toroid is 1500 A giving a field inside the yoke of 1.8 T in the central toroid and 1.9 T in the end toroids.

B.1.2 Silicon Microstrip Tracker

The Silicon Microstrip Tracker (SMT) is a solid state semiconductor detector. Sensors are made from bulk n-type[1] silicon and are either single- or double-sided. Single-sided sensors are made by implanting p-type[2] silicon in strips on one side of the n-type bulk silicon. Double-sided sensors are made by implanting strips of n-type silicon with a larger fraction of donor impurities than the bulk material on the other side of single-sided sensors. Voltage is applied across the strips such that the p-type implants sit at a negative voltage compared to the n-type bulk or n-type strips. This creates a large region where there are no free charge carriers as the holes (electrons) in the p-type (n-type) material are attracted to the cathode (anode). This region is referred to as the depletion region and is the active area of

---

[1] N-type semiconductors have majority charge carriers (electrons) that are *negative* and are produced by adding impurities that donate electrons to the material lattice.

[2] P-type semiconductors have majority charge carriers (holes) that are *positive* and are produced by adding impurities that accept electrons to the material lattice.

the detector. When a charged particle passes through the sensor it ionizes the material in the depletion region creating electron-hole pairs. These migrate to the strips and the charge is read out.

The detector is composed of many of these sensors arranged in barrels and disks. An isometric view of the SMT is shown in Fig. B.3. The barrels provide a measurement of the r-ϕ for the tracks in the central (small $|\eta|$) region of the detector. Disks measure the r-z coordinate as well as the r-ϕ coordinate in the forward (high $|\eta|$) regions. There are six barrels in total capped at the high $|z|$ end by a disk composed of wedge detectors called an F-disk. Each end of the barrel region is capped by three additional F-disks. One large diameter disk, called an H-disk, is located in the far-forward regions. A separate system called Layer 0 is installed inside the inner diameter of the barrels and disks.

B.1.2.1 Barrels

Each of the six barrels has four layers with each layer composed of two sublayers. The barrel silicon module, called a *ladder*, consists of a 12 cm long sensor region and front-end electronics necessary to read out the sensor on a beryllium substrate. Ladders in the sublayers are arranged such that they provide an overlap in ϕ as in Fig. B.3. Each barrel contains 72 ladders with sensors of varying widths. The second and fourth layer of all barrels have ladders with double-sided silicon sensors. The p-side has strips oriented parallel to the beam pipe with a strip-to-strip distance (*pitch*) of 50 μm. Strips on the n-side are oriented at an angle of 2° with respect to the axial strips and have a pitch of 62.5 μm. The first and third layers of the two outer barrels have single-sided ladders with a strip pitch of 50 μm oriented parallel to the beam pipe. For the inner four barrels, the first and third layers have double-sided ladders with a 90° stereo angle. The p-side strips are aligned parallel to the

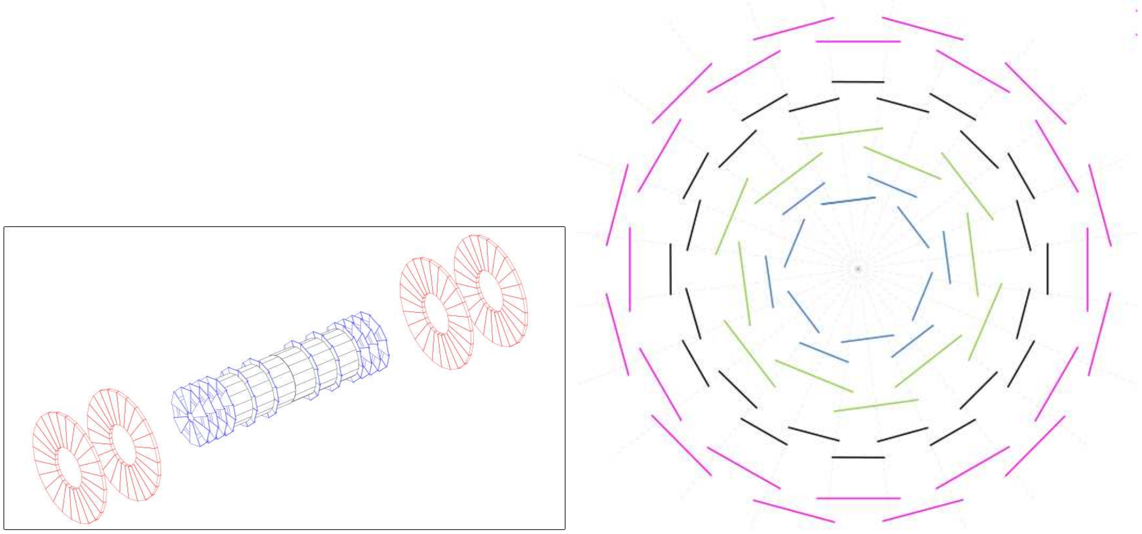

Figure B.3: *D0 Silicon Microstrip Tracker*
An isometric view of the D0 SMT. Note that the two far-forward H-disks were removed to install Layer 0 (not shown).

beam pipe as in the single-sided devices while the n-side strips are perpendicular.

B.1.2.2 F-disks

There are 12 F-disks in all: one at the high $|z|$ end of each of the six barrels and three at each end of the barrel assembly. Each F-disk is made in 12 sections with one double-sided sensor per section. The sensors are isosceles trapezoids with strips on either side aligned with a long edge of the trapezoid, giving a 30° stereo angle. The sections are joined with alternating p- and n-sides facing the center of the detector. The strip pitch for the p- and n-sides are equal to those of the double-sided 2° barrel sensors. The active length of the barrel/disk structure and the end F-disks is approximately 1066 mm.

B.1.2.3 H-disks

There are currently two H-disks in the D0 detector, though there were four at the beginning of Run II. They are located at $z \approx \pm 100$ cm. Twenty-four trapezoidal sensors comprise each H-disk. Each sensor is formed by gluing two single-sided sensors back-to-back. Like the F-disks, strips are aligned with a long edge of the trapezoid, giving an effective stereo angle of 15°. The strip pitch for these detectors is 40 μm.

B.1.2.4 Layer 0

Layer 0 was installed along with a new beryllium beam pipe in 2006. It resides in the space between the beam pipe and the first layers of the barrels. The whole device is approximately 1660 mm long with the sensors covering $z \leq |380|$ mm. There are 48 single-sided sensors in all with strip pitches of 71 μm and 81 μm. They are arranged on a hexagonal carbon fiber support tube with a row of eight sensors on each face. Rows alternate between 16.1 mm and 17.6 mm from the beam axis. The 71(81) μm strip pitch sensors are located 16.1(17.6) mm from the beam.

B.1.3 Central Fiber Tracker

The Central Fiber Tracker (CFT) is a scintillating fiber detector. The passage of charged particles through the fibers produces photons from ionization and excitation events. Because the number of photons produced in scintillating fiber for an ionization/excitation event is small, it is important that the device detecting these photons is extremely sensitive. We use *visual light photon counters* (VLPCs) which produce an electrical signal in response to photons and are capable of detecting single photons. Fibers were made by extruding polystyrene doped with two fluorescent dyes. The primary fluorescent dye (about 1% by weight) is rapidly excited by the neighboring excited polystyrene through a non-radiative near-field interaction. The primary fluorescent rapidly relaxes and emits a short wavelength ($\approx$ 340 nm) photon. Because this photon does not travel far in polystyrene, the second dye, a wavelength-shifter, is necessary. The second dye (present at about 1500 ppm) absorbs this photon and re-emits it at $\approx$ 530 nm, which is transmitted well by polystyrene. With two claddings of decreasing index of refraction the attenuation length in these scintillating fibers is approximately 5 m. Once out of the active volume of the CFT, the light travels in light-shielded clear fibers which are chemically similar to the scintillating fibers all the way to the VLPCs at the bottom of the detector.

B.1.3.1 Fiber Arrangement

The scintillating fibers in the CFT are 835 μm in diameter and are 1.66 m or 2.52 m in length. They are grouped into ribbons of 256 fibers each in two rows of 128. The fiber spacing ranges from 928 μm to 990 μm and depends on the radius at which the fibers are located. The second row of fibers is offset from the first by half this distance. These ribbons are bonded to the outside of carbon fiber support cylinders in two layers: an axial layer and a stereo layer. In the axial layer the fibers are oriented parallel to the beam axis. The stereo layer has fibers oriented at a $\pm 3^\circ$ angle with respect to the axial layer. The sign of the angle alternates between cylinders. There are eight cylinders total occupying the radial space from 20 cm to 52 cm.

B.2 Preshower Detectors

Directly outside the solenoid before the calorimeter are the preshower detectors. They can be considered part of both the tracking system and the calorimetry; they mark the beginning of electromagnetic showering and are used to match tracks to showers seen in the calorimeter. Like the CFT, the preshower detectors use scintillation light to detect the passage of charged particles. Instead of single fibers the preshower detectors use polystyrene strips with a triangular cross section. The strips are doped with fluorescent dye and a wavelength-shifting fiber is placed in the center. The light is collected by the center fiber and transferred to VLPCs for read-out via clear fiber. There are three preshower detectors: the Central Preshower detector (CPS) and two Forward Preshower detectors (FPS). All three use the same type of scintillating strips but the strips are arranged differently for the CPS and FPS.

B.2.1 CPS

The CPS sits between the solenoid and the calorimeter. Directly outside the solenoid is a lead radiator covered with steel. This radiator and the solenoid provide about two radiation lengths to particles with normal incidence. At larger angles this increases to about four radiation lengths. Scintillator strips in the CPS are nested together to form single layers that are approximately 7 mm tall, slightly taller than the strips themselves. The CPS consists of three such layers of scintillator: one axial layer and two stereo layers with angles of $\approx \pm 24^\circ$.

B.2.2 FPS

There are two FPS detectors, one on either end of the D0 detector. They are mounted on the end calorimeter cryostats (see Section B.3). Scintillator strips in the FPS are nested together such that a layer of scintillator is about as tall as a strip: about 5 mm. There are four super-layers separated in z in each FPS detector. Each super-layer consists of eight active $\phi = 22.5^\circ$ modules separated by eight inactive regions. The second and fourth super-layers are rotated by 22.5° with respect to the first and third super-layers, creating two active effective layers in each 22.5° wedge. Each layer consists of two sublayers of scintillator strips with a 22.5° stereo angle between them. The inner layer is shorter than the outer layer and mainly detects minimally ionizing particles. Between the inner and outer layer is a short piece of lead/steel absorber which adds two radiation lengths in the path of the particles producing electromagnetic showers in the outer layer. The solenoid provides up to three radiation lengths for particles traveling in the outer area of the outer layer where there is no absorber.

B.3 Calorimeters

The primary purpose of the calorimeter is to make a measurement of the energy of particles produced in the D0 detector. Unlike the tracking system which is designed to measure the passage of particles with minimal disturbance, the calorimeter is designed to stop particles completely. In this way particles make a complete deposit of their energy. The D0 detector uses a *sampling* calorimeter that has alternating layers of absorber and active material. Particles traveling through the absorber create showers of secondary particles that are either electromagnetic or hadronic in nature as described in Section 2.3.1. These secondary particles ionize the active material and the charge is collected and measured. The D0 calorimeter is a *compensating* combined electromagnetic (EM) and hadronic calorimeter; it has an equal response to electromagnetic and hadronic particles with the same energy. Because EM and hadronic shower generation is governed by two different length scales – the radiation length (X_0) and the nuclear interaction length (λ_A) – the calorimeter has varying absorber thicknesses and materials to capture both types of showers. In high Z materials X_0 is much smaller than λ_A so EM showers occur closer to the interaction region than hadronic showers.

The D0 calorimeter has three showering layers: the EM layer, the fine hadronic layer, and the coarse hadronic layer. The active material in the D0 calorimeter is liquid argon. For accessibility, the calorimeter is divided into three separate cryostats, a central cryostat and two end cryostats. Depending on the layer and cryostat the absorber is either depleted uranium, a uranium-niobium alloy, copper, or steel. A typical calorimeter cell is shown in Fig. B.4. Sensor pads interleaved between sheets of absorber are patterned for segmented readout. Cells whose centers lie at the same η and ϕ are ganged together in depth to create readout towers as shown in Fig. B.5.

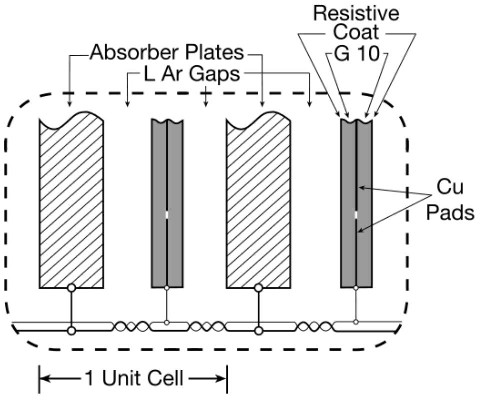

Figure B.4: *Calorimeter Cell*
Schematic of a typical calorimeter cell.

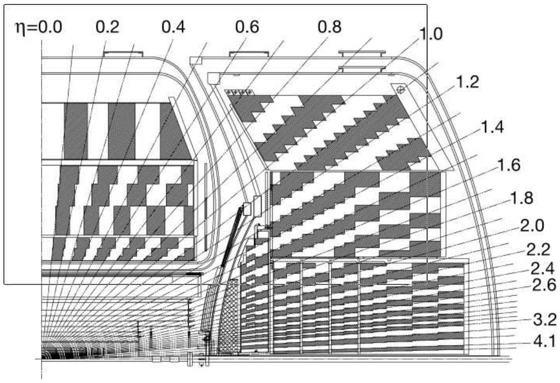

Figure B.5: *Calorimeter Readout Towers*
Shown are the D0 calorimeter readout towers. Calorimeter cells lying at the same η and ϕ are ganged together to form towers for readout.

B.3.1 Central Calorimeter

The central calorimeter (CC) covers the region $|\eta| \lesssim 1$. The EM section is made from 3 mm-thick absorber plates of nearly pure depleted uranium. It has four separate depth layers, or gangings, that are 1.4, 2.0, 6.8, and 9.8 X_0 thick. The total number of radiation lengths from material between the calorimeter and the interaction region is about four at $\eta = 0$. The fine hadronic section is made from 6 mm-thick plates of a uranium-niobium alloy. It has three gangings that are 1.3, 1.0, and 0.76 λ_A thick. There is only one coarse hadronic layer made from 46.5 mm-thick plates of copper that is 3.2 λ_A thick.

B.3.2 End Calorimeters

The end calorimeters (EC) extend the coverage of the calorimeter to $|\eta| \lesssim 4$. The material between the interaction region and the first active gap in the EC provides approximately 4.4 X_0 of material at $\eta = 2$. Like the CC, the EC has four depth layers in the EM section that are approximately 1.6, 2.6, 7.9, and 9.3 X_0 thick. The EM section is a disk made from plates of nearly pure depleted uranium 4 mm thick. The hadronic sections of the EC are divided into three regions from the beam line: the inner hadronic, middle hadronic, and outer hadronic regions. The inner and middle hadronic regions have both fine and coarse hadronic sections. Fine hadronic sections are made from 6 mm-thick uranium-niobium plates and have four gangings 1.1(0.9) $\lambda_A$thick in the inner (middle) hadronic sections. There is only one depth layer for the inner (middle) coarse hadronic section that is made from 46.5 mm-thick steel plates with a total thickness of 4.1(4.4) λ_A. The outer hadronic region has only one coarse hadronic ganging made from the same steel plates with a total maximum thickness of 6.0 λ_A. These plates are inclined at an angle of approximately 60° with respect to the beam axis to avoid cracks.

B.4 Muon System

Because of their higher mass, muons do not radiate as much energy via bremmstrahlung as electrons. They don't produce particle showers and leave the detector with most of their energy intact. They do however leave ionization tracks in the detector. The muon system sits on the very outer faces of the detector and exists to make measurements of muons as they exit the detector. The toroid magnet discussed in Section B.1.1 is an essential part of the muon system. A measurement of the muon momentum can be made by measuring the position of tracks before and after traversing the toroid. Tracks in the muon system can also be matched to tracks in the tracking portion of the detector for muon identification. Using quick response scintillation material the muon system can associate a muon track with the correct bunch crossing. This scintillator is also important in *event triggering*, a process which selects events for recording based on desirable event features, such as an event with an associated muons. More information on event triggering can be found in Section B.7. It is also possible to reject cosmic ray backgrounds which originate outside the detector and traverse the detector at large angles. In addition to the fast response scintillator, the muon system uses wire drift tubes to track muons. The drift tubes collect the charge left when passing particles ionize the surrounding gas.

B.4.1 Wide Angle Muon System

The Wide Angle Muon System (WAMUS) covers the $|\eta| \lesssim 1$ region. It consists of the central toroid magnet (Section B.1.1), three layers of proportional drift tubes (PDTs), the cosmic cap and bottom scintillation counters, and the $A\phi$ scintillation counters.

B.4.1.1 Proportional Drift Tubes

There are three layers of PDTs in WAMUS denoted A, B, and C. The A-layer resides between the calorimeter and the central toroid magnet while the B- and C-layers lie outside the central toroid. Each layer consists of either three or four stacks of PDTs. Each 10.1 cm PDT cell is made from a long rectangular aluminum tube with an anode wire in the center and a cathode pad above and below the anode wire. The tube is filled with 84% argon and 8% CH_4/CF_4 that gives a maximum electron drift time of 500 ns. Two anode wires are ganged together and are read out at one end of each cell. Position information along the PDT is gathered from the timing difference between the signal at the end of the struck wire and the signal at the end of its partner's wire. The position resolution using this method can be anywhere from 10 cm-50 cm depending on where the hit occurred. Information about the amount of charge deposited on the cathode pads can bring the resolution down to about 5 mm. As can be seen in the exploded view of the D0 muon wire chambers in Fig. B.6, the PDT coverage on the bottom is sparse due to the calorimeter supports. Still, approximately 55% of the central region is covered by three layers of PDTs and close to 90% of the region is covered by at least two layers of PDTs.

B.4.1.2 Cosmic Cap and Bottom

The cosmic cap and bottom scintillation counters cover the outer layer of the central muon PDTs. The cosmic cap refers to the counters covering the top and sides of the central muon C-layer PDTs while the cosmic bottom refers to counters covering the bottom B- and C-layer central muon PDTs. Both provide fast timing information that is used to associate a hit in a PDT with the appropriate bunch crossing and to reject the cosmic ray background.

There are 240 cosmic cap scintillation counters. Each counter is made from 0.5 in-thick plastic scintillator 25 in wide and 81.5 in-113 in long. They are oriented with their length along ϕ and their width along z. Light from charged particle interactions is gathered by wavelength shifting fibers that are glued into grooves along the length of the scintillator from each end to just past the center. Fibers are collected in the center into two bundles and the light is detected by two photomultiplier tubes (PMTs) mounted directly on the counter.

There are 132 counters in the cosmic bottom on the outside of the B and C PDT layers. Refer to Fig. B.7 for the placement of the counters. In contrast to the cosmic cap counters, the cosmic bottom counters are placed with their width along ϕ and their length along z. There are two types of counters employed in the cosmic bottom; both are similar in design to the cosmic cap counters. Forty-eight counters in the center bottom B-layer are identical to the cosmic cap counters with minor improvements in edge fiber placement. There are sixteen total counters located on the bottom sides of the B-layer PDTs. The remaining 68 counters on the bottom B- and C-layer PDTs have fewer total fibers that are placed in vertical rather than horizontal grooves like those in the cosmic cap. The light yield in this arrangement is similar to that in the cosmic cap. Like the cosmic cap, light is detected by PMTs mounted directly on the counter.

B.4.1.3 $A\phi$ Scintillation Counters

In addition to the scintillator on the outer layers of central muon PDTs there is another layer of scintillator on the outside of the A-layer PDTs generally referred to as the $A\phi$ scintillation counters. These counters are used for identifying and triggering on muons, rejecting backscattering from the forward direction, and providing a time stamp on low p_T

muons that may not reach the cosmic cap and bottom counters. The counters are made from scintillator plastic with wavelength shifting fibers embedded in vertical grooves in a manner similar to the second type of cosmic bottom counter. Like the cosmic cap and bottom, the light is detected by a PMT mounted directly to the counter case. The $A\phi$ counters are 33.25 in long and are used in three widths: 14.46 in, 10.84 in, and 9.09 in. The use of three different widths allows for a relatively constant 4.5° segmentation in ϕ that matches the segmentation of the CFT. Counters are aligned with their lengths along z and their widths along ϕ with the widest counters located at the corners of the detector and the thinnest near the center line. A gap of approximately 2.5 m on the center bottom accommodates the calorimeter support. Nine counters butted end-to-end make up the length of the detector for a total of 630 counters.

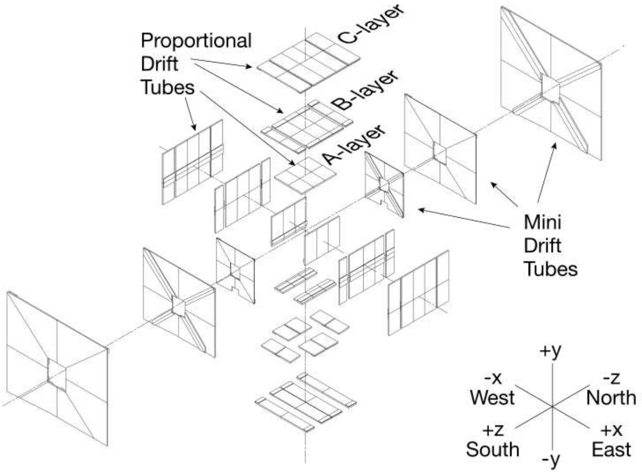

Figure B.6: *D0 Muon Wire Chambers*
Exploded view of the D0 muon wire chambers.

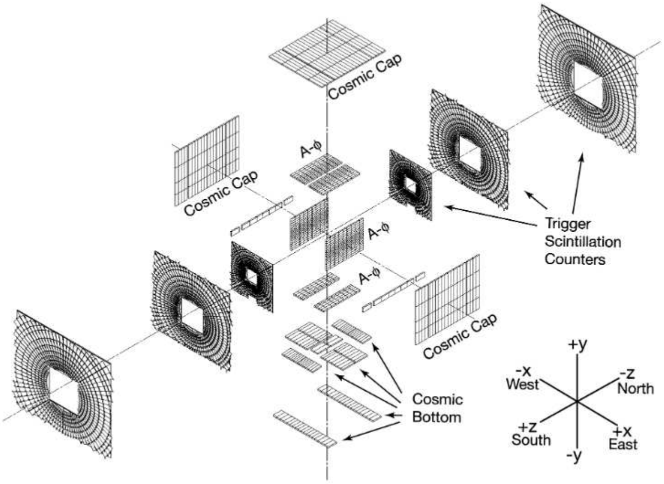

Figure B.7: *D0 Muon Scintillator*
Exploded view of the D0 muon scintillator.

B.4.2 Forward Angle Muon System

The Forward Angle Muon System (FAMUS) covers the region $1 \lesssim |\eta| \lesssim 2$. It consists of the end faces of the toroid magnet (Section B.1.1), three layers of mini drift tubes (MDTs), three layers of scintillation counters, and a significant amount of shielding. The shielding nearly eliminates the two main sources of non-muon background from proton and antiproton remnants: *i*) their interactions with the end of the calorimeter and beam pipe inside the detector and *ii*) their interactions with the Tevatron quadrupoles just outside the detector. The shielding surrounds the beam pipe from the end calorimeter cryostat, through the end toroid magnet, to the wall of the collision hall where it partially surrounds the Tevatron quadrupole magnets. It is made from layers of lead, polyethylene, and iron to absorb gamma rays, neutrons, and electromagnetic and hadronic particles respectively.

B.4.2.1 Mini Drift Tubes

Muon momentum measurements in the forward region use arrays of mini drift tubes (MDTs). Identical in operating principle to the PDTs, these are smaller and hence have a much smaller maximum drift time of about 60 ns. There are three layers arranged inside the toroid (layer A) and outside the toroid (layers B and C). Each layer has either three or four stacks of MDTs mounted along the magnetic field lines of the end face toroids. Each MDT is composed of eight rectangular aluminum cells with an internal cross section of 9.4×9.4 mm^2 and a W-Au anode wire down the center. The wire is grounded at the electronics and the cathode is held at a constant negative high voltage. Cells are filled with a CF_4-CH_4 (90%-10%) gas mixture. The coordinate resolution for the MDTs when taking into account the timing electronics is approximately 0.7 mm per hit.

B.4.2.2 Forward Scintillator Counters

The forward scintillator counters are primarily used for triggering on events that contain muons. They are arranged in three layers inside (layer A) and outside the toroid (layers B and C). Each layer is composed of 0.5 in plastic scintillator tiles cut into trapezoids and arranged in a fish scale pattern around the beam pipe as shown in Fig. B.8. The segmentation in ϕ is approximately 4.5° to match the segmentation in the CFT for triggering purposes. Segmentation in η is 0.12 for the inner nine layers and 0.07 for the outer three layers. The outer C-layer counters are the largest at 60×110 cm^2. Each tile has wavelength-shifting bars on two adjacent edges to collect and transmit light to the PMT attached to the tile.

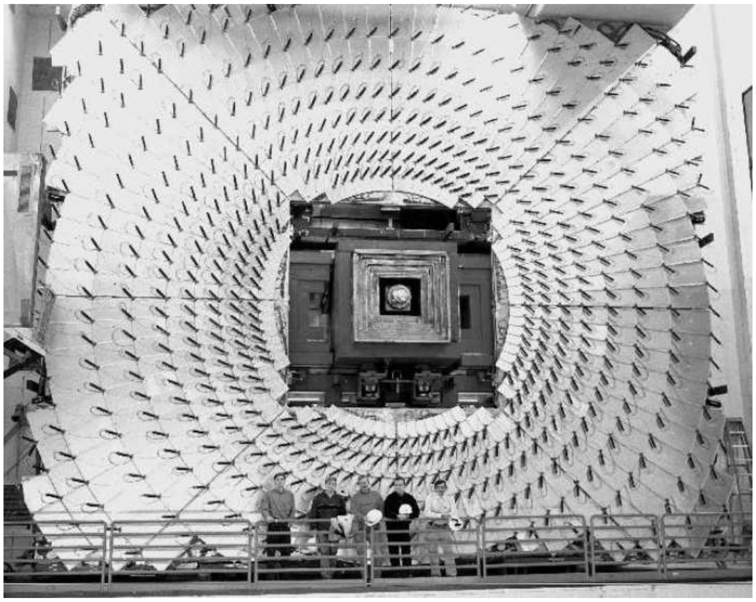

Figure B.8: *Forward Muon Scintillator*

B.5 Forward Proton Detector

A subdetector, called the Forward Proton Detector (FPD), designed to measure scattered protons and antiprotons that do not impinge on the main detector is located on either side of the detector inside the Tevatron tunnel. It is primarily used to tag *diffractive* events where one or both incident protons survive the interaction intact[3] and are scattered at very small angles with respect to the beam.

The FPD is a momentum spectrometer that uses magnets in the accelerator lattice and position detectors which can be moved very close to the beam. There are nine independent spectrometers: one on the outgoing antiproton side of the D0 detector downstream from the bending dipole magnet and four on each side of the D0 detector downstream from the low β quadrupoles. There are two horizontal (in and out) and two vertical (up and down) spectrometers to either side of the D0 detector. The spectrometer downstream from the

---

[3] Contrary to elastic scattering, additional particles are produced in the scattering event even in the case where both protons are intact.

bending dipole is to the inside of the bend. Each spectrometer has an upstream and a downstream position detector. The position detectors are housed in movable stainless steel containers called Roman pots which allow them to operate outside the ultra-high vacuum of the beam pipe and be retracted during suboptimal beam conditions. Roman pots are grouped into castles: four castles with four Roman pots each serving the upstream and downstream position detectors of the eight spectrometers nearest the D0 detector and two castles with one Roman pot each serving the spectrometer downstream from the bending dipole.

The position detectors are made from six stacks of scintillating fiber ribbons arranged with the edges of the ribbons in the plane perpendicular to the beam. Stacks are oriented at angles of ± 45 ° and 90° with respect to the bottom of the detector. There are two stacks in each orientation that are offset by 2/3 of the fiber width. Scattered protons and antiprotons travel through a thin steel window and impinge on the scintillator. Fibers are read out by multi-anode photomultiplier tubes and integrated into the CFT electronics. Between the 90° and -45 ° layers is a solid piece of scintillating plastic read out by a fast photomultiplier tube that is used for triggering purposes (See Section B.7).

B.6 Luminosity Monitor

Measuring the instantaneous luminosity being provided to D0 by the Tevatron is an important process both for online operation and off-line data analysis. The instantaneous luminosity dictates the trigger set used at a given time during operation and therefore determines the physics processes being recorded for later analysis. Off-line analyses require an accurate luminosity measurement for proper event yield predictions of specific processes.

The D0 subdetector responsible for measuring the instantaneous luminosity is the Luminosity Monitor (LM). Additionally, the LM provides a fast measurement of the z coordinate of the interaction vertex and a measurement of the beam halo.

These measurements are done by detecting inelastic proton-antiproton collisions through scintillation light. Two arrays of plastic scintillation counters located at $z = \pm 140$ cm comprise the LM. Each array contains 24 counters divided into two enclosures attached to the spherical head of the end calorimeters. At 15 cm long, they occupy the radial space between the beam pipe and the FPS detector over the pseudorapidity range $2.7 < |\eta| < 4.4$. Their location in the forward region close to the interaction point necessitates the use of radiation-hard PMTs for readout.

Signals from each array are collected and a timing pulse is created for each array. The difference in the timing pulses determines the z coordinate of the interaction vertex z_{vtx} to within 6 cm. To select only those interactions which originate from beam-beam collisions, a cut is placed on the z coordinate of the interaction vertex such that $|z_{vtx}| < 100$ cm. This encompasses nearly all of the proton-antiproton collisions produced by the Tevatron. Any beam halo particles traveling parallel to the beam and not participating in the beam-beam collisions will have a z_{vtx} of approximately ± 140 cm and be excluded by the cut. The instantaneous luminosity L is determined by the bunch crossing frequency f of the Tevatron, the average number of inelastic proton-antiproton collisions per crossing $\bar{N}_{LM}$ as measured by the LM, and the effective[4] inelastic $p\bar{p}$ cross section into the LM σ_{LM} given by Eq. B.1.

$$L = \frac{f\bar{N}_{LM}}{\sigma_{LM}} \tag{B.1}$$

---

[4] The cross section is an effective one; it has factors which account for the *acceptance* and *efficiency* of the LM. The acceptance is related to the probability that an interaction will have particles in the geometric coverage of the LM. Given that particles are in the acceptance of the LM, the efficiency is related to the probability that the event will be recorded by the detector.

The effective inelastic $p\bar{p}$ cross section σ_{LM} is calculated to be 46 ± 3 mb. In general $\bar{N}_{LM}$ is greater than one and must be determined by counting the fraction of beam crossings without events and applying Poisson statistics.

B.7 Triggering System

With 36 bunches of protons and antiprotons traveling around the Tevatron 48 thousand times per second, there are approximately 1.7 million possible interactions per second. Recording all of these interactions is not feasible. Fortunately, a large fraction of these events are uninteresting for the purposes of the D0 experiment. By having an idea of what interesting events look like to the detector, we can use a process called *triggering* to look for and record only the events we find interesting. D0 uses a three-tiered triggering system based in both hardware and software to accomplish this. The levels are designed to act as a filtering system with each step increasing in complexity. The Level 1 (L1) trigger consists of hardware elements with an accept rate of approximately 2 kHz. Events that pass are sent to the Level 2 (L2) system which consists of hardware and microprocessors associated with each subdetector and a global processor that makes trigger decisions not only based on individual physics objects but object correlations as well. The accept rate of L2 is approximately 1 kHz. If an event is passed by L2 it is sent to the farm of about 250 computer nodes that make up Level 3 (L3). Level 3 passes events at a rate of about 50 Hz. Those events are recorded for later offline reconstruction.

B.7.1 Level 1

Level 1 is implemented in hardware devices which originate in four detector subsystems: the scintillating fiber tracking system, the calorimeter, the muon system, and the forward proton detector. Every event is examined and each subsystem submits event information to the trigger framework (TFW). The TFW constructs physics triggers from the triggers constructed by the L1 systems using AND/OR logical operators. In addition to the construction of physics triggers the TFW manages communication with the front-end electronics and the trigger control computer, applies prescaling to triggers, and coordinates readout upon a L2 accept. The logical OR of the physics triggers is what determines whether the event is selected for additional processing in Level 2.

B.7.1.1 L1 Tracking

The scintillating fiber systems which participate in the Level 1 trigger decision are the FPS and CFT/CPS axial systems, collectively referred to as the Central Track Trigger (L1CTT). By design these systems provide triggers for charged particles with a transverse momentum p_T greater than 1.5 GeV. Finding tracks, finding energy clusters originating in the preshower detectors, and matching tracks to clusters are the main functions of the scintillating fiber systems in L1. Significant processing resources are reserved for finding and triggering on isolated charged particle tracks. In addition, lists of tracks are sent to the L1 muon system to be used as seeds.

B.7.1.2 L1 Calorimeter

The calorimeter groups readout towers two by two in η and ϕ into trigger towers. Transverse energy E_T thresholds are set for the sum total of all trigger towers and for each trigger tower individually. In addition, thresholds can be defined for the total unbalanced or "missing" transverse energy $\not\!\!E_T$. The partial sums necessary for the calculation can be used to trigger on jets which are much larger than the trigger towers.

B.7.1.3 L1 Muon

The Level 1 muon system looks for hit patterns consistent with the passage of a muon using the muon scintillator and wire chambers and the seed tracks from the L1CTT system. Triggers are formed in the scintillator by 1) matching L1CTT tracks to hits in either the A-layer or the A- and B-layer and 2) requiring hits in either the A-layer or the A- and B-layer without a matched track. Additionally, hits in the muon wire chambers are used to confirm scintillator hits in each layer. These confirmed hits are used to form triggers 3) in either the A-layer or the A- and B-layer scintillator.

B.7.1.4 L1 FPD

The Forward Proton Detector also takes part in the Level 1 trigger. It selects events in which beam particles leave the interaction region intact and hit one or more FPD spectrometers. We create a pixel grid from the stacks of scintillating ribbon in the position detectors and compare pixel hits to detector pixel hit patterns stored in hardware. Timing information is obtained from the trigger scintillator using fast photomultiplier tubes. The FPD trigger system uses this timing information to look for coincidences between hit signals of both position detectors for any of the nine spectrometers signaling the passage of an intact beam particle. Coincidences between spectrometers on either side of the interaction region are indicative of an event where both beam particles leave the interaction region intact.

B.7.2 Level 2

Following a Level 1 accept from the TFW, the event begins processing at L2. Level 2 consists of a detector-specific preprocessing stage and a global processing stage. The preprocessing stage collects information from the L1 trigger system and the detector front-ends to form physics objects. At the global level, data from different parts of the detector can be combined to form higher-quality physics objects than those available at the preprocessing stage. In addition, correlations between objects across the whole detector can be examined. All detector subsystems participating in Level 1 also participate in Level 2 with the exception of the Forward Proton Detector. Also participating in L2 is the Silicon Microstrip Tracker. The finer spatial resolution of the SMT with respect to the CFT allows for a more precise track reconstruction and an improved momentum measurement. The L2 global processing stage runs algorithms on the data received from the preprocessors based on what triggers fired at Level 1. The L2 global decision is returned to the TFW.

B.7.3 Level 3

Events which pass Level 2 are sent to the Level 3 trigger. Level 3 is a fully programmable software trigger which has access to the full detector information. It performs a limited reconstruction of the full event and makes its decision based on complete physics objects and their relationships. The software resides on about 250 commercial computers running the Linux operating system. Event fragments from different parts of the detector are routed to a single L3 node where the event is built and made available to L3 processes. Events selected by L3 are destined for storage on tape and full offline reconstruction.

Appendix C

Additional Distributions

This appendix contains additional plots and tables not included in the main text.

C.1 Additional VX Distributions

Plots of the invariant (transverse) mass are included for all VH analyses for each b-tagging channel and purity region. The high-purity plots for the WH analysis are reproduced here for comparison.

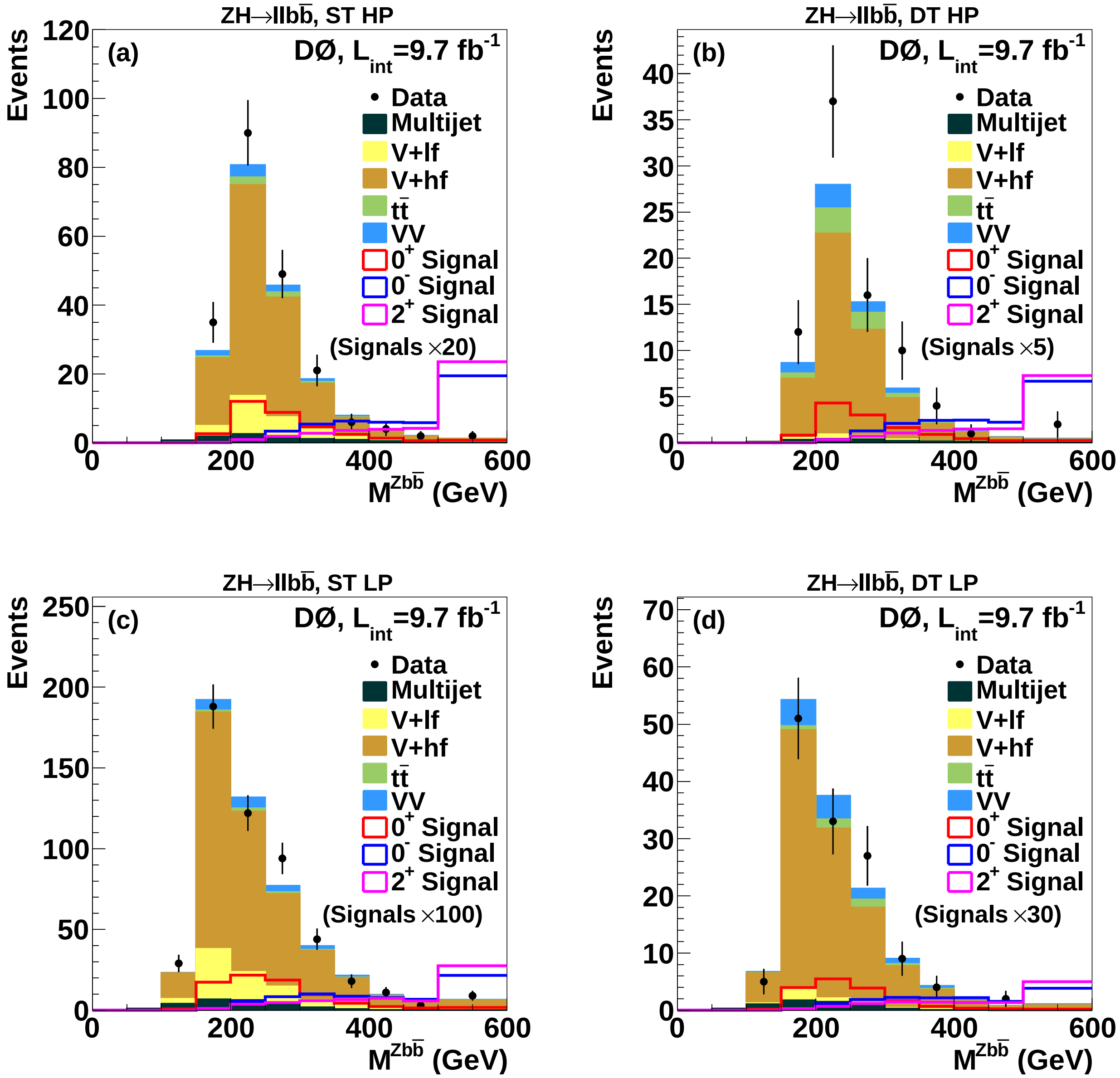

Figure C.1: *Invariant Mass of the $\ell\ell b\bar{b}$ System*

Invariant mass of the $\ell\ell b\bar{b}$ system in the $ZH \to \ell\ell b\bar{b}$ analysis for events in the (a) single-tag high-purity (ST HP), (b) double-tag high-purity (DT HP), (c) single-tag low-purity (ST LP), and (d) double-tag low-purity (DT LP) channels. The $J^P = 2^+$ and $J^P = 0^-$ samples are normalized to the product of the SM cross section and branching fraction multiplied by an additional factor. Heavy- and light-flavor quark jets are denoted by lf and hf, respectively. Overflow events are included in the last bin. For all signals, a mass of 125 GeV for the H or X boson is assumed.

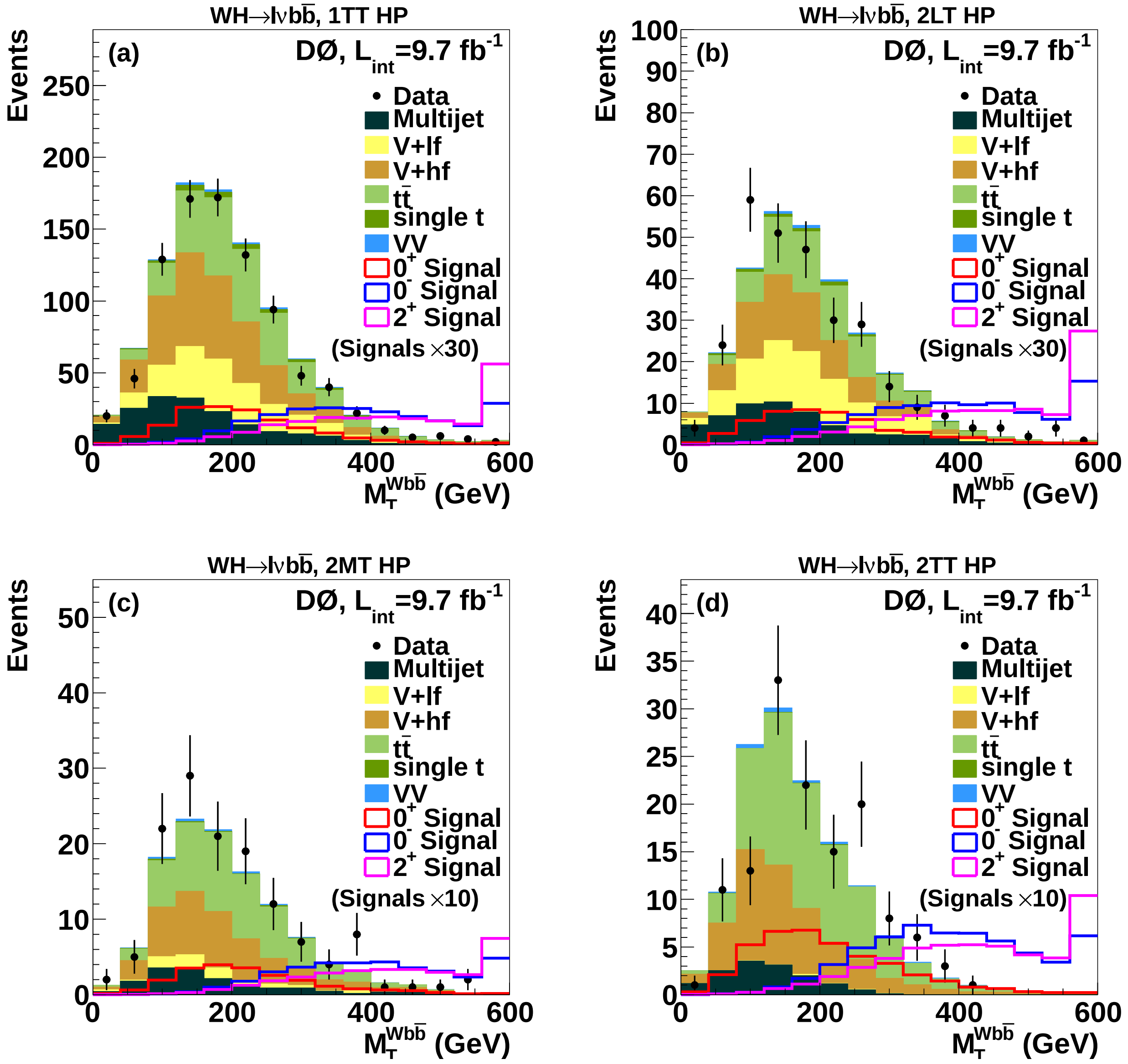

Figure C.2: *Transverse Mass of the $\ell\nu b\bar{b}$ System, High-Purity Region*
Transverse mass of the $\ell\nu b\bar{b}$ system in the $WH \rightarrow \ell\nu b\bar{b}$ analysis in the high-purity (HP) region for (a) 1 tight-tag (1TT), (b) 2 loose-tags (2LT), (c) 2 medium-tags (2MT), and (d) 2 tight-tags (2TT) channels. The $J^P = 2^+$ and $J^P = 0^-$ samples are normalized to the product of the SM cross section and branching fraction multiplied by an additional factor. Heavy- and light-flavor quark jets are denoted by lf and hf, respectively. Overflow events are included in the last bin. For all signals, a mass of 125 GeV for the H or X boson is assumed.

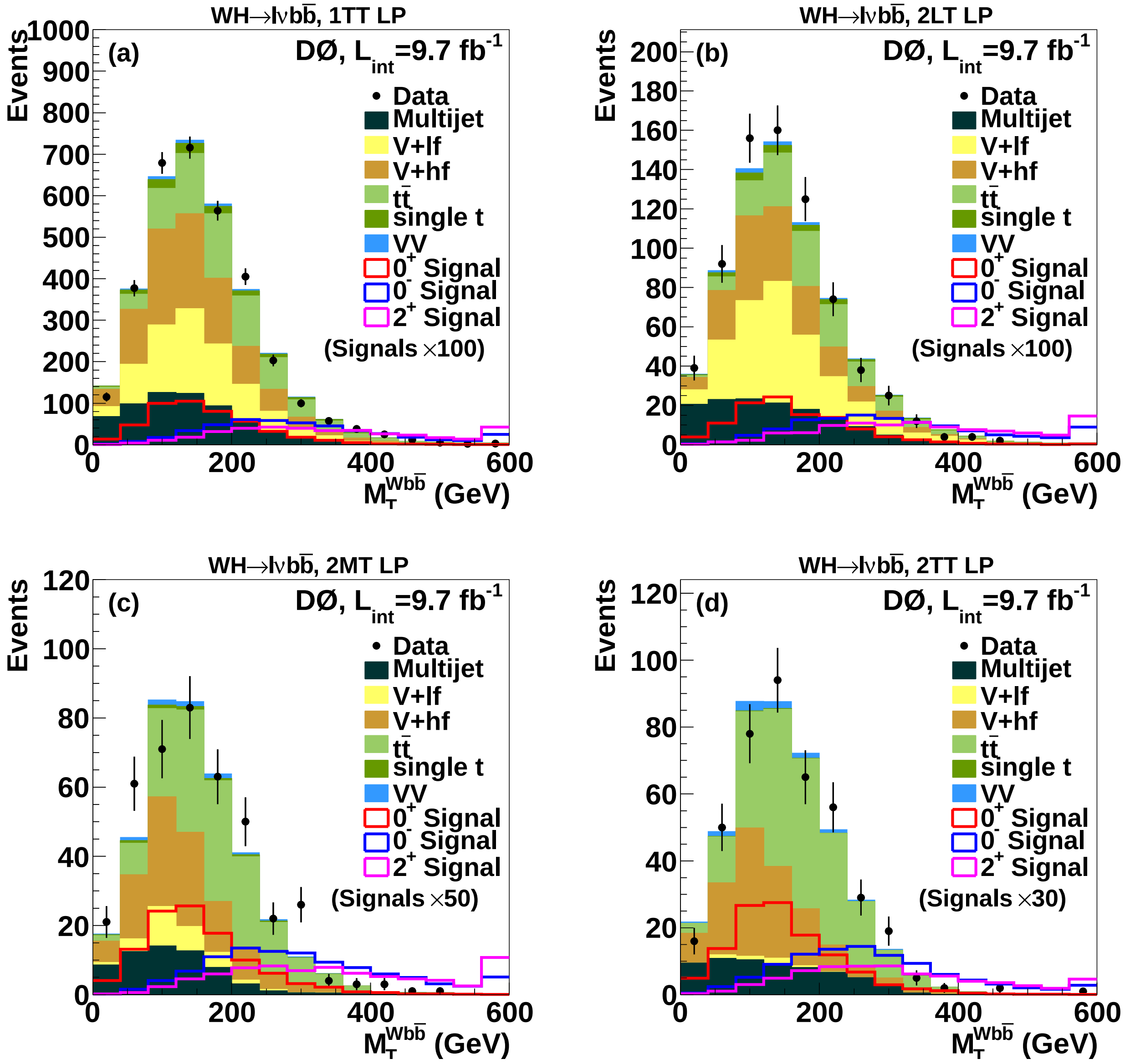

Figure C.3: *Transverse Mass of the $\ell\nu b\bar{b}$ System, Low-Purity Region*
Transverse mass of the $\ell\nu b\bar{b}$ system in the $WH \to \ell\nu b\bar{b}$ analysis in the low purity (LP) region for (a) 1-tight-tag (1TT), (b) 2-loose-tags (2LT), (c) 2-medium-tags (2MT), and (d) 2-tight-tags (2TT) channels. The $J^P = 2^+$ and $J^P = 0^-$ samples are normalized to the product of the SM cross section and branching fraction multiplied by an additional factor. Heavy- and light-flavor quark jets are denoted by lf and hf, respectively. Overflow events are included in the last bin. For all signals, a mass of 125 GeV for the H or X boson is assumed.

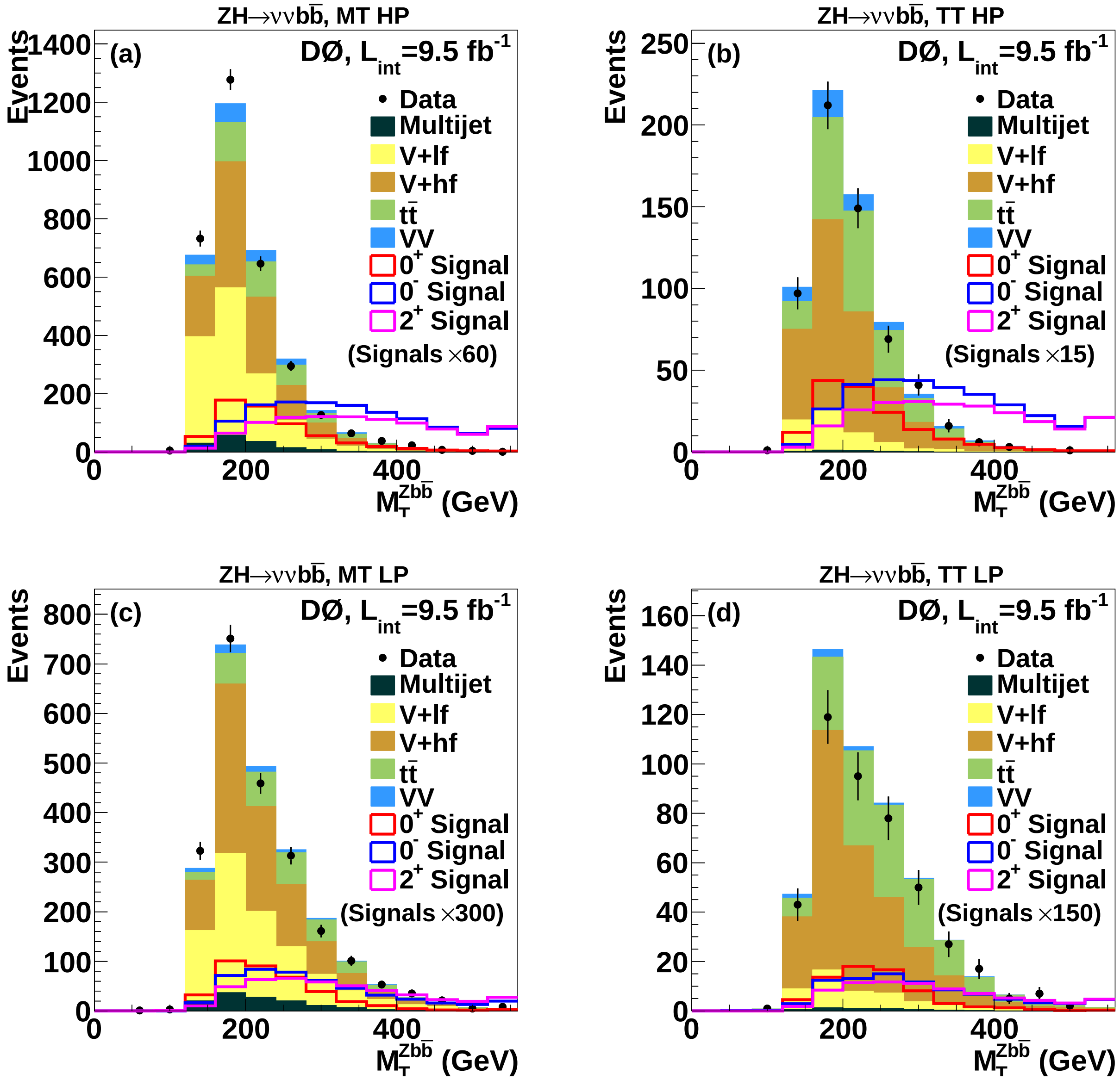

Figure C.4: *Transverse Mass of the $\nu\nu b\bar{b}$ System*
Transverse mass of the $\nu\nu b\bar{b}$ system in the $VH \rightarrow \nu\nu b\bar{b}$ analysis for events in the (a) medium-tag high-purity (MT HP), (b) tight-tag high-purity (TT HP), (c) medium-tag low-purity (MT LP), and (d) tight-tag low-purity (TT LP) channels. The $J^P = 2^+$ and $J^P = 0^-$ samples are normalized to the product of the SM cross section and branching fraction multiplied by an additional factor. Heavy- and light-flavor quark jets are denoted by lf and hf, respectively. Overflow events are included in the last bin. For all signals, a mass of 125 GeV for the H or X boson is assumed.

C.2 Additional LLR Distributions

This section contains LLR distributions for each VH analysis and all analyses combined for $\mu = 1.0$.

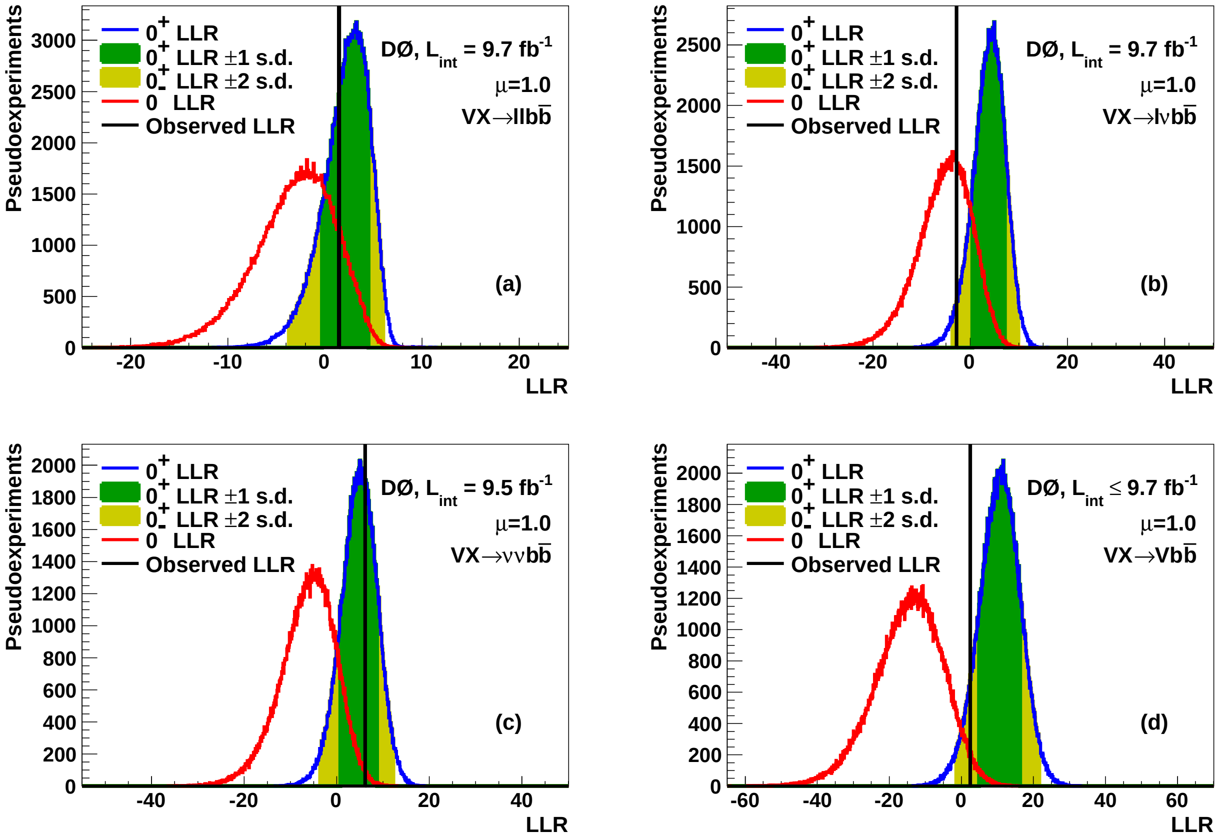

Figure C.5: *D0 LLR Distributions for the $J^P = 0^-$ Hypothesis*
LLR distributions comparing the $J^P = 0^+$ and the $J^P = 0^-$ hypotheses for the (a) $ZH \to \ell\ell b\bar{b}$ analysis, (b) $WH \to \ell\nu b\bar{b}$ analysis, (c) $VH \to \nu\nu b\bar{b}$ analysis, and (d) their combination. The $J^P = 0^+$ and $J^P = 0^-$ samples are normalized to the product of the SM cross section and branching fraction multiplied by $\mu = 1.0$. The vertical solid line represents the observed LLR value, while the dark and light shaded areas represent 1 s.d. and 2 s.d. on the expectation from the null hypothesis H_0, respectively. Here H_0 is the SM $J^P = 0^+$ signal plus backgrounds. For all signals, a mass of 125 GeV for the H or X boson is assumed.

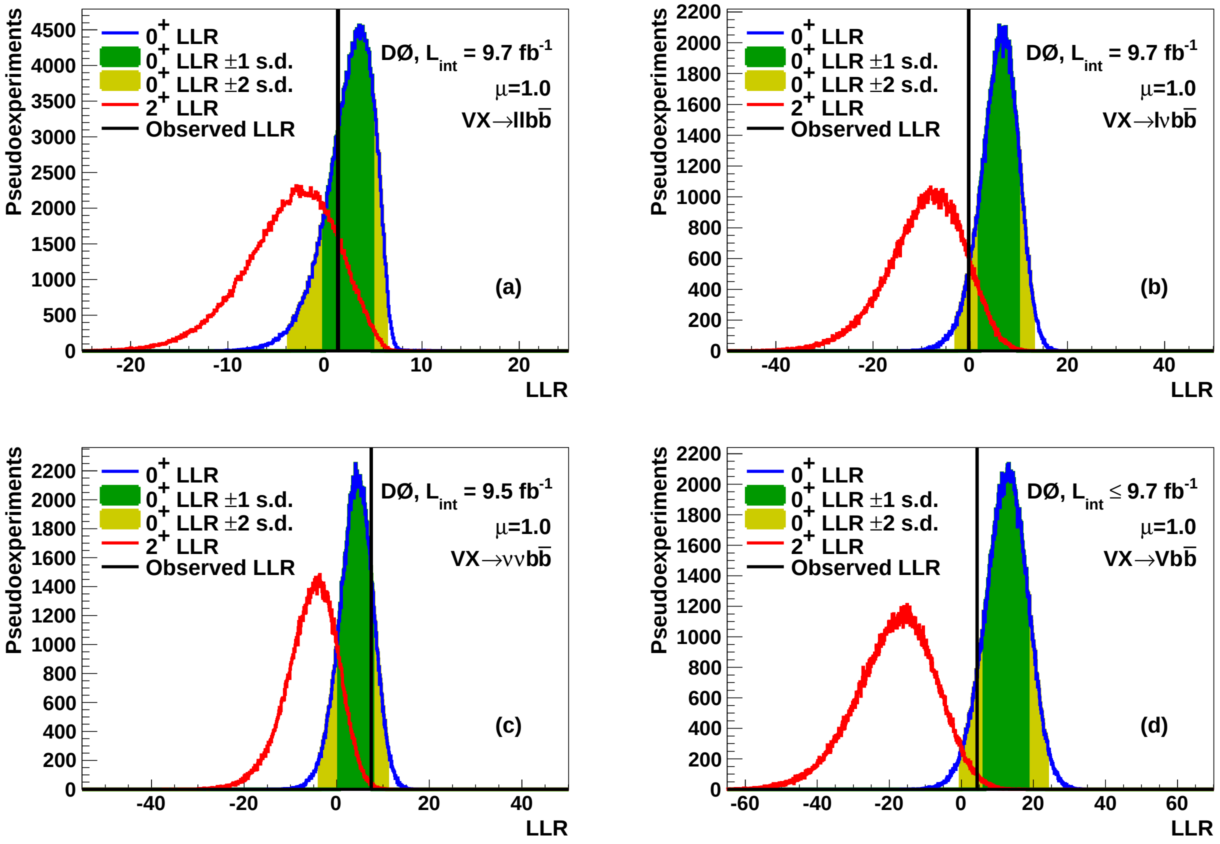

Figure C.6: *LLR Distributions for the* $J^P = 2^+$ *Hypothesis*
LLR distributions comparing the $J^P = 0^+$ and the $J^P = 2^+$ hypotheses for the (a) $ZH \rightarrow \ell\ell b\bar{b}$ analysis, (b) $WH \rightarrow \ell\nu b\bar{b}$ analysis, (c) $VH \rightarrow \nu\nu b\bar{b}$ analysis, and (d) their combination. The $J^P = 0^+$ and $J^P = 2^+$ samples are normalized to the product of the SM cross section and branching fraction multiplied by $\mu = 1.0$. The vertical solid line represents the observed LLR value, while the dark and light shaded areas represent 1 s.d. and 2 s.d. on the expectation from the null hypothesis H_0, respectively. Here H_0 is the SM $J^P = 0^+$ signal plus backgrounds. For all signals, a mass of 125 GeV for the H or X boson is assumed.

C.3 Expected and Observed p-values for $\mu = 1.23$

Analysis	$ZH \to \ell\ell b\bar{b}$	$WH \to \ell\nu b\bar{b}$	$ZH \to \nu\nu b\bar{b}$	Combined
	$J^P = 0^-$ vs. $J^P = 0^+$			
$p_{\text{test}}^{0^-}$ Expected	0.046	0.012	0.005	<0.0001
$p_{\text{test}}^{0^-}$ Observed	0.072	0.245	0.0006	0.005
$1 - p_{\text{null}}$ Expected	0.500	0.500	0.500	0.500
$1 - p_{\text{null}}$ Observed	0.615	0.971	0.215	0.922
CL_s Expected	0.908 (1.33 s.d.)	0.975 (1.96 s.d.)	0.989 (2.31 s.d.)	0.9998 (3.60 s.d.)
CL_s Observed	0.883 (1.19 s.d.)	0.747 (0.67 s.d.)	0.997 (2.78 s.d.)	0.995 (2.56 s.d.)
	$J^P = 2^+$ vs. $J^P = 0^+$			
$p_{\text{test}}^{2^+}$ Expected	0.037	0.003	0.009	<0.0001
$p_{\text{test}}^{2^+}$ Observed	0.078	0.056	0.003	0.002
$1 - p_{\text{null}}$ Expected	0.500	0.500	0.500	0.500
$1 - p_{\text{null}}$ Observed	0.679	0.937	0.363	0.911
CL_s Expected	0.925 (1.44 s.d.)	0.995 (2.56 s.d.)	0.983 (2.11 s.d.)	0.9999 (3.86 s.d.)
CL_s Observed	0.885 (1.20 s.d.)	0.941 (1.56 s.d.)	0.991 (2.35 s.d.)	0.998 (2.91 s.d.)

Table C.1: *Expected and Observed p-Values for $\mu = 1.23$*
Expected and observed p-values and CL_s values for $J^P = 0^-$ and $J^P = 2^+$ VX associated production, assuming signal cross sections equal to the 125 GeV SM Higgs production cross section multiplied by $\mu = 1.23$. The null hypothesis is taken to be the sum of the SM Higgs boson signal and background production.

REFERENCES

REFERENCES

[1] E. W. Weisstein, Cylindrical coordinates, From MathWorld – A Wolfram Web Resource.

[2] E. W. Weisstein, Spherical coordinates, From MathWorld – A Wolfram Web Resource.

[3] O. Chamberlain, E. Segrè, C. Wiegand, and T. Ypsilantis, Phys. Rev. **100**, 947 (1955).

[4] K. A. Olive *et al.*, [Particle Data Group], Chinese Physics C **38**, 090001 (2014).

[5] H. D. Politzer, Phys. Rev. Lett. **30**, 146 (1973).

[6] D. J. Gross and F. Wilczek, Phys. Rev. Lett. **30**, 1343 (1973).

[7] S. L. Glashow, Nucl. Phys. **22**, 579 (1961).

[8] S. Weinberg, Phys. Rev. Lett. **19**, 1264 (1967).

[9] A. Salam, Originally printed in Svartholm: Elementary Particle Theory, Proceedings Of The Nobel Symposium Held 1968 At Lerum, Sweden, Stockholm 1968, 367-377.

[10] P. W. Higgs, Phys. Rev. Lett. **13**, 508 (1964).

[11] F. Englert and R. Brout, Phys. Rev. Lett. **13**, 321 (1964).

[12] G. S. Guralnik, C. R. Hagen, and T. W. B. Kibble, Phys. Rev. Lett. **13**, 585 (1964).

[13] L. Álvarez-Gaumé and J. Ellis, Nat. Phys. **7**, 2 (2011).

[14] M. Baak *et al.*, The European Physical Journal C **74** (2014).

[15] G. Abbiendi *et al.*, [ALEPH, DELPHI, L3, and OPAL Collaborations, the LEP Working Group for Higgs Boson Searches], Phys. Lett. B **565**, 61 (2003).

[16] S. Heinemeyer, C. Mariotti, G. Passarino, and R. Tanaka (Eds.), [LHC Higgs Cross Section Working Group], CERN-2013-004 (2013).

[17] T. Aaltonen *et al.*, [CDF and D0 Collaborations], Phys. Rev. D **88**, 052014 (2013).

[18] T. Aaltonen *et al.*, [CDF and D0 Collaborations], Phys. Rev. Lett. **109**, 071804 (2012).

[19] G. Aad *et al.*, [ATLAS Collaboration], Phys. Lett. B **716**, 1 (2012).

[20] S. Chatrchyan *et al.*, [CMS Collaboration], Phys. Lett. B **716**, 30 (2012).

[21] S. Dimopoulos and H. Georgi, Nucl. Phys. B **193**.

[22] H. Murayama, UCB-PTH-00/05 (2000), Pedagogical review SUSY review given at 1999 ICTP Summer School.

[23] G. Branco *et al.*, Phys. Rep. **516**, 1 (2012).

[24] A. Djouadi, Phys. Rep. **459**, 1 (2008).

[25] L. Randall and R. Sundrum, Phys. Rev. Lett. **83**, 3370 (1999).

[26] L. Randall and R. Sundrum, Phys. Rev. Lett. **83**, 4690 (1999).

[27] F. Abe *et al.*, [CDF Collaboration], Phys. Rev. Lett. **74**, 2626 (1995).

[28] S. Abachi *et al.*, [D0 Collaboration], Phys. Rev. Lett. **74**, 2422 (1995).

[29] S. Abachi *et al.*, Nucl. Instrum. Methods Phys. Res. A **338**, 185 (1994).

[30] V. Abazov *et al.*, Nucl. Instrum. Methods Phys. Res. A **565**, 463 (2006).

[31] R. Angstadt *et al.*, Nucl. Instrum. Methods Phys. Res. A **622**, 298 (2010).

[32] S. Chatrchyan *et al.*, [CMS Collaboration], Phys. Rev. D **89**, 092007 (2014).

[33] G. Aad *et al.*, [ATLAS Collaboration], Phys. Lett. B **726**, 120 (2013).

[34] A. Martin, W. Stirling, R. Thorne, and G. Watt, The European Physical Journal C **63**, 189 (2009).

[35] W. J. Stirling, private communication.

[36] D. Miller, S. Choi, B. Eberle, M. Mhlleitner, and P. Zerwas, Phys. Lett. B **505**, 149 (2001).

[37] J. D. Richman, CALT-68-1148 (1984).

[38] J. Ellis, D. S. Hwang, V. Sanz, and T. You, J. High Energy Phys. **2012**, 134 (2012).

[39] V. M. Abazov *et al.*, [D0 Collaboration], Phys. Rev. Lett. **109**, 121803 (2012).

[40] T. Aaltonen *et al.*, [CDF Collaboration], Phys. Rev. Lett. **109**, 111804 (2012).

[41] J. Pumplin *et al.*, J. High Energy Phys. **07**, 012 (2002).

[42] T. Sjöstrand, S. Mrenna, and P. Skands, J. High Energy Phys. **2006**, 026 (2006).

[43] R. Brun and F. Carminati, Cern program library long writeup w5013.

[44] J. Alwall *et al.*, J. High Energy Phys. **2014** (2014).

[45] P. Aquino, K. Hagiwara, Q. Li, and F. Maltoni, J. High Energy Phys. **2011**, 1 (2011).

[46] K. Hagiwara, J. Kanzaki, Q. Li, and K. Mawatari, Eur. Phys. J. C **56**, 435 (2008).

[47] A. Djouadi, J. Kalinowski, and M. Spira, Computer Phys. Comm. **108**, 56 (1998).

[48] M. L. Mangano, F. Piccinini, A. D. Polosa, M. Moretti, and R. Pittau, J. High Energy Phys. **2003**, 001 (2003).

[49] V. Abazov *et al.*, Phys. Lett. B **669**, 278 (2008).

[50] E. E. Boos, V. E. Bunichev, L. V. Dudko, V. I. Savrin, and V. V. Sherstnev, Phys. Atom. Nucl. **69**, 1317.

[51] A. Hoecker *et al.*, PoS **ACAT**, 040 (2007).

[52] T. Junk, Nucl. Instrum. Methods Phys. Res. A **434**, 435 (1999).

[53] A. L. Read, J. Phys. G **28**, 2693 (2002).

[54] W. C. Fisher, FERMILAB-TM-2386-E (2006).

[55] W. C. Fisher, private communication.

[56] T. Andeen *et al.*, FERMILAB-TM-2365 (2007).

[57] N. Kidonakis, Phys. Rev. D **74**, 114012 (2006).

[58] U. Langenfeld, S. Moch, and P. Uwer, Phys. Rev. D **80**, 054009 (2009).

[59] J. M. Campbell and R. K. Ellis, Phys. Rev. D **60**, 113006 (1999).

[60] J. M. Campbell, R. K. Ellis, and C. Williams, Mcfm - monte carlo for femtobarn processes.

[61] J. M. Campbell, FERMILAB-Conf-01/072-T .

[62] V. M. Abazov *et al.*, [D0 Collaboration], Phys. Rev. D **88**, 052011 (2013).

[63] V. M. Abazov *et al.*, [D0 Collaboration], Phys. Rev. Lett. **109**, 121804 (2012).

[64] V. M. Abazov *et al.*, [D0 Collaboration], Phys. Lett. B **716**, 285 (2012).

[65] V. M. Abazov *et al.*, [D0 Collaboration], Phys. Rev. Lett. **113**, 161802 (2014).

[66] T. Aaltonen *et al.*, [CDF Collaboration], Phys. Rev. Lett. **114**, 141802 (2015).

[67] T. Aaltonen *et al.*, [CDF Collaboration], Phys. Rev. Lett. **109**, 111803 (2012).

[68] T. Aaltonen *et al.*, [CDF Collaboration], Phys. Rev. Lett. **109**, 111805 (2012).

[69] T. Aaltonen *et al.*, [CDF and D0 Collaborations], Phys. Rev. Lett. **114**, 151802 (2015).